Investigation of Efficiency in Applied Field MagnetoPlasmaDynamic Thrusters

Dan Lev

A Dissertation
Presented to the Faculty
of Princeton University
in Candidacy for the Degree
of Doctor of Philosophy

Recommended for Acceptance
by the Department of
Mechanical and Aerospace Engineering
Adviser: Professor Edgar Y. Choueiri

January 2012

Abstract

An experimental and theoretical investigation of the scaling of thrust efficiency with the operational parameters (J,B,$\dot{m}$) of applied-field magnetoplasmadynamic thrusters (AF-MPDTs) is carried out to provide guidelines for scaling and controlling AF-MDPT performance. This investigation is based on characterization of the various power dissipation mechanisms in AF-MPDTs with a focus on the acceleration and anode sheath power components.

A semi-empirical model is derived for the anode sheath voltage fall in AF-MPDTs and verified by comparison to experimental data on a 30 kW lithium-fed steady-state AF-MPDT obtained using a hot langmuir probe. It is found that the anode sheath voltage fall increases approximately linearly with current and applied magnetic field and is inversely proportional to mass flow rate. It is shown that, although the electrons in the anode sheath are unmagnetized the voltage fall is attributed to plasma density reduction at the sheath edge, which is a result of increased plasma pinching at higher applied magnetic field values. It is also concluded that increased thermionic emission from the anode surface leads to an increase in the anode sheath voltage fall; therefore anode material with a high work function is preferred.

A thrust efficiency model is formulated by employing a thrust formula previously derived and verified for the same thruster, and composing expressions for the different voltage components in AF-MPDTs. It is demonstrated that the efficiency increases with applied magnetic field for all current and mass flow rate values, and the enhancement of the efficiency by the applied magnetic field is greater when the mass flow rate is reduced. It is shown that the efficiency-current curves have a decreasing-increasing behavior due to an interchange between the different thrust components, each of which dominates in a different current regime and thus affects the scalability of the acceleration power component with current.

It is demonstrated that electrodes power losses, primarily anode sheath power

losses, are the dominant power dissipation mechanism in AF-MPDTs. It is also demonstrated that resistive power deposition, which is responsible for plasma heating and ionization, has little effect on the overall efficiency, except in the low current regime in which resistive power losses can account for more than a third of the total thruster power.

The physical insights obtained from this study can aid in forming design criteria and general guidelines for AF-MPDT design and control.

Acknowledgements

This PhD thesis could not have been completed without the help of many individuals to whom I owe my deepest gratitude.

My wife Sivan, who supported me from over the ocean ever since my first day at Princeton and eventually joined me so we would become a true family. I will never be able to thank you enough for enduring the long distance relationship for so long and, most importantly, bearing our children, Yuval and Amit.

Eddie, who gave me the great opportunity to come and work in the EP lab. Every conversation we had taught me something new and made me stop and think. You always insisted on nothing less than the best, from me and for me, and for this I thank you.

The former fellow students in the lab. Jimmy, Luke, Peter and Ashley who were there when I first arrived and introduced me to the lab, Princeton and American culture. Jimmy and Luke, the support and advice you gave me while being in the lab, and later on after leaving the lab, was priceless. Ashley, who was a great friend, I miss the late night BBQs.

The current fellow students. Ben, Justin and Matthew, who were such good and supportive friends. I will never forget the help and support that all of you gave me, especially near the end of my time at Princeton. Ben, who spent the mornings with me talking about nonsense, and Jenna who became friends with my wife. Justin, the party king, who always had good laughs with me while embracing a new foreign girlfriend. Matthew, who is funny and open, and reminded me how it is to be at the beginning of research.

Bob, who taught me so many things about everything. Machining, the economy, electronics, gold, hardware design, politics and so much more. I owe you a great debt for bearing with me through the intimidating lithium system, while enriching me with yet another piece of American culture. You taught me how to “thimk”. Thank you.

Prof. Jahn, who gave me advice and was always willing to listen to new ideas and research plans. I valued everything you told me.

I would also like to thank Yevgeny Raitses and Sam Cohen for their support at PPPL and at the university. You were always willing to help.

Finally, I would like to thank Greg Emsellem, who saved my research project by teaching me about the experiment and how to conduct research well and quickly. Thank you.

This dissertation carries the number T-3234 in the records of the Department of Mechanical and Aerospace Engineering

Contents

List of Tables

List of Figures

List of Symbols

A_a	Anode inner surface area
$A_{a,eff}$	Effective anode current attachment surface area
A_R	Richardson-Dushman coefficient
a_0	Sonic speed
$\bar{B}$	Magnetic field
B_a	Magnetic field at the cathode tip and solenoid center
B_c	Magnetic field at the anode face
$\bar{E}$	Electric field
E_m	Energy of the mth energy level
e	Electron charge
$\bar{f}$	Lorentz force density
f_{nm}	Oscillator strength
g_m	Degeneracy of the mth energy level
I_m	Current to solenoid
I_{mn}	Spectral line intensity
Isp	Specific impulse
J	Total thruster current
J_{ci}	Critical ionization current
J_{onset}	Onset current
$\bar{j}$	Current density

j_e	Electron current density
j_{em}	Thermionic emission current density
j_{net}, j_∞	Thruster net current density
K_{gd}	Gas dynamic thrust coefficient
K_{self}	Self-field thrust coefficient
K_H	Hall thrust coefficient
k_B	Boltzmann constant
$\dot{m}$	Mass flow rate
m_e	Electron mass
m_i	Ion mass
m_i	Initial propellant mass
m_p	Propellant mass
m_{tot}	Total mass
N_A	Avogadro's number
n_e	Electron density
P_{acc}	Acceleration power
P_E	Electrodes' power
P_{res}	Resistive power
P_{tot}	Total power
r_a	Anode radius
r_c	Cathode radius
r_L	Electron Larmour radius
$\mathcal{T}$	Thrust
$\mathcal{T}/P$	Thrust-to-power ratio
T_a	Anode temperature
T_e	Electron temperature
T_i	Ion temperature

$\bar{u}$	Velocity
u_e	Exhaust velocity
V_a	Anode sheath voltage fall
V_c	Cathode voltage fall
V_E	Electrodes' voltage
V_{emf}	Back electromotive voltage
V_{heat}	Plasma heating voltage
V_i	Ionization voltage
V_{tot}	Total thruster voltage
β_i	Ionization coefficient
γ_e	Electron specific gas ratio
γ_i	Ion specific gas ratio
Δ_{CL}	Charge-limited potential difference
Δt	Mission duration
ΔV	Velocity increment
ϵ	Material emissivity
ϵ_{eff}	Effective emissivity
ϵ_i	Ionization energy
η	Efficiency
κ	Thermal conductivity
λ_{De}	Debye length
μ_0	Permeability of free space
μ_{pl}	Molecular weight of plasma
ν_e	Electron collision frequency
σ	Stephan-Boltzmann constant
σ_0	Scalar conductivity
Φ	Plasma potential

ϕ	Electric potential
ϕ_a	Anode work function
ϕ_W	Material work function
ρ	Mass density
ξ	Normalized ionization current
Ω_e	Electron Hall parameter

Chapter 1

Introduction

1.1 Overview

For decades mankind has improved its capability to reach outer-space, travel to neighboring planets and even escape the solar system. As space travel encompasses great opportunities for the future of mankind the continuous development of new technologies is essential for mankind's further advancement. One major limitation to space exploration is purely financial as the cost of launching a spacecraft into orbit or conducting a mission to other planets is quite expensive and often disabilitating the mission. Launching a satellite into low earth orbit presently costs up to $20,000/kilogram[1], and this cost increases with the distance to target and mission duration. For example, the 'Mars Reconnaissance Orbiter' launched in 2005 cost over $40,000/kilogram[2] due to the large amounts of propellant, consisting of over 50% of initial mass, required to deliver the spacecraft from low Earth orbit to Mars orbit. Mission cost increases sharply with the required propellant mass, thus reducing the propellant mass is of great benefit to the realization of more frequent missions with larger payloads.

The rocket equation derived by Tsiolkovsky[3] relates the propellant mass fraction

to the nature of the space mission performed and the propulsion system's exhaust velocity.

$$\frac{m_p}{m_i} = 1 - \exp\left(-\frac{\Delta V}{u_e}\right) \tag{1.1}$$

where m_p is the propellant mass, m_i is the initial spacecraft mass, ΔV is the velocity increment needed to perform a space mission and u_e is the thruster's exhaust velocity. Each interplanetary mission has its own ΔV requirement based on trajectory changes from point of origin to the target and can be thought of as a "mission price tag" regardless of the propulsion system used. On the other hand the exhaust velocity u_e is a characteristic of the propulsion system and varies from one thruster type to another. Propellant mass ratio vs. exhaust velocity curves based on Eq. 1.1 are plotted in Fig 1.1 for the cases of Ohman transfer from Earth to Mars and Earth to Pluto missions. In both of these examples the ΔV taken was from the Earth's sphere of influence (low Earth orbit) to the target planet sphere of influence[4]. It can be seen from the figure that small changes in u_e can contribute to huge mass savings. It is also obvious that for missions to remote planets such as Pluto chemical propulsion is not a suitable solution. It is therefore financially and energetically beneficial to use propulsion systems with high exhaust velocities.

While conventional chemical rockets are capable of producing exhaust velocities no higher than $u_e \simeq 4,500$ m/s, electric thrusters hold the premise of delivering high exhaust velocities of over an order of magnitude higher ($O(10^4)$ m/s). This fact makes electric propulsion a very attractive option for interplanetary missions within and beyond the solar system.

Electric thrusters come in a variety of geometries and configurations, with each satisfying different goals depending upon the application. Presently, the two most widely used electric thrusters are the ion engines and Hall thrusters. These two types of electric thrusters convert electrical power to accelerate the propellant to exhaust velocities of up to 10^5 m/s in ion engines and over 10^4 m/s in Hall thrusters[5].

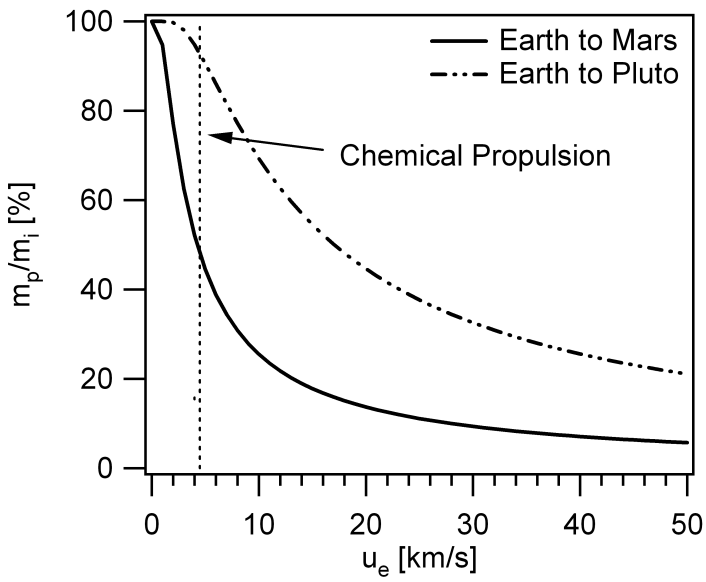

Figure 1.1: Propellant mass ratio vs. exhaust velocity for low Earth orbit to Mars orbit and low Earth orbit to Pluto orbit missions.

Unfortunately these types of thrusters hold the disadvantages of low thrust density, which is the thrust per unit area, and the ability to process no more than about 1 kW in a typical thruster. In order to increase thrust in a Hall thruster more mass needs to be added which requires a larger thruster so not to reduce the Hall parameter. In order to increase the thrust in an ion engine more mass needs to be added which will cause charge limitation that will have to be compensated by a larger grid, hence a larger thruster. In both of these types of thrusters an increase in thrust is followed by an increase in the physical size of the thruster while the thrust density does not change. These shortcomings extend mission duration for Hall thrusters and ion engines relative to chemical thrusters and require multiple or large thrusters to execute a particular mission, making the spacecraft heavier.

For this reason another type of electric thruster generating higher thrust densities could be useful for near-Earth interplanetary missions. One such thruster is the MagnetoPlasmaDynamic (MPD) thruster.

1.2 The MPD Thruster

Magnetoplasmadynamic thrusters (MPDTs) are a subclass of plasma thrusters with an overwhelmingly electromagnetic acceleration mechanism involving the interaction of a current between an anode and a cathode and a magnetic field, which could be externally applied or induced by the current itself (Fig. 1.2). This interaction gives rise to a Lorentz force density ($f = j \times B$) that accelerates propellant out of the thruster. This acceleration mechanism enables operation at high number densities, relative to other types of electric thrusters, thus high thrust densities. MPDTs promise a wide range of thrust levels (100 mN - 100 N)[6, 7, 8] depending on the power level, along with high exhaust velocities (from 10 km/s up to 100 km/s with hydrogen) a high thrust efficiency, (10-25% with argon and up to 60% with lithium propellant), and the ability to process hundreds of kW to multi MW of power in a single compact device.

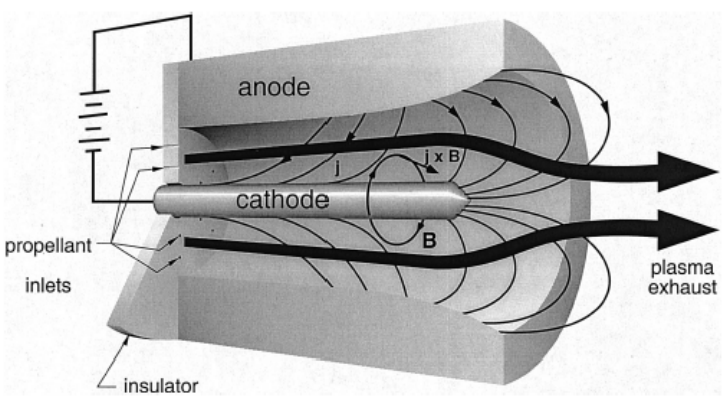

Figure 1.2: MagnetoPlasmaDynamic (MPD) thruster schematic.

When an external magnetic field is applied to an MPDT it is called the *applied-field* MPDT (AF-MPDT) whereas if the current interacts with the magnetic field induced by the current itself the thruster is named the *self-field* MPDT. The thrust generation mechanism of the self-field MPDT is well understood and was characterized by Maecker [9] and Jahn [10] and analyzed by Choueiri[11] who showed how

the various components of thrust scale with geometric and operational parameters. Jahn[10] showed that the expression for thrust in self-field MPDTs can be written as

$$\mathcal{T}_{self} = \frac{\mu_0 J^2}{4\pi} \left[\ln\left(r_a/r_c\right) + \phi\right] \tag{1.2}$$

where μ_0 is the permeability of free space, J is the total current to the thruster, r_a and r_c are the anode and cathode radii respectively and ϕ is a parameter of the order of 1 and depends on the current attachment to the cathode tip. ϕ is conventionally taken as 3/4.

Equation 1.2 was derived by neglecting the electrothermal component of thrust. This is a valid assumption in the high-current operational regime where the electromagnetic contribution is dominant. One consequence of this high-current assumption is that the resulting expression for thrust is independent of the mass flow rate, $\dot{m}$. For lower current levels, however, it is necessary to include the thermal contribution. In a more detailed analysis, Choueiri[11] derived an expression for thrust that explicitly depends on the mass flow rate and showed that in the high current regime, this expression converges toward Eq. 1.2.

It has been well established[6] that the addition of an applied magnetic field to the thruster increases its performance significantly. This is often necessary at low power levels (below 100 kW) where the current is too low for the self-induced magnetic field to be sufficient to produce substantial thrust. Thrust, efficiency and exhaust velocity tend to increase with the applied magnetic field intensity. It has been observed[6] that the thrust increases linearly with the product JB, where B is the value of the applied magnetic field measured at the solenoid's center. This linear increase regime with JB depends on the mass flow rate, thruster geometry and materials, and propellant used. This increase is not similar to the thrust increase in self field MPDTs where the thrust scales with the current squared (J^2). In addition, thrust efficiencies in AF-

MPDTs were reported to be significantly larger, for the same power levels,[7, 8, 12] than the thrust efficiencies observed in self-field MPDTs. The detailed physics behind the acceleration mechanism in AF-MPDTs is not yet fully understood and further experimental research is needed.

1.3 Description of the LiLFA

The focus of ongoing studies of AF-MPDTs is on the most promising variant called the **Li**thium **L**orentz **F**orce **A**ccelerator (LiLFA) shown in Fig. 1.3. The LiLFA is a steady state AF-MPDT that uses lithium as a propellant and employs a multi-channel hollow cathode through which the lithium vapor propellant is injected into the thruster's acceleration region. Lithium has great potential for two main reasons: 1) Lithium's first ionization potential (5.4 eV) is significantly lower than that of other, commonly-used propellants such as argon (15.7 eV), xenon (12.1 eV) or hydrogen (13.6 eV), while lithium's second ionization potential is significantly higher than these other propellants. Therefore the frozen flow losses associated with multiply-ionized species are expected to be lower in lithium-fed MPDTs. 2) Lithium (especially with the addition of small amounts of barium) lowers the work function of the thruster's cathode, thus enabling cathode operation at much lower temperatures[13], reducing cathode erosion. The above two advantages make lithium a very good candidate for high power AF-MPDTs. Lithium-fed MPDTs have high efficiencies, in the range of 20% to 60% depending on the power level, and due to their low electrode erosion rate (when trace amounts of barium are added to the propellant), have demonstrated hundreds of hours of high-power operation (at 0.5 MW) without showing significant damage[14].

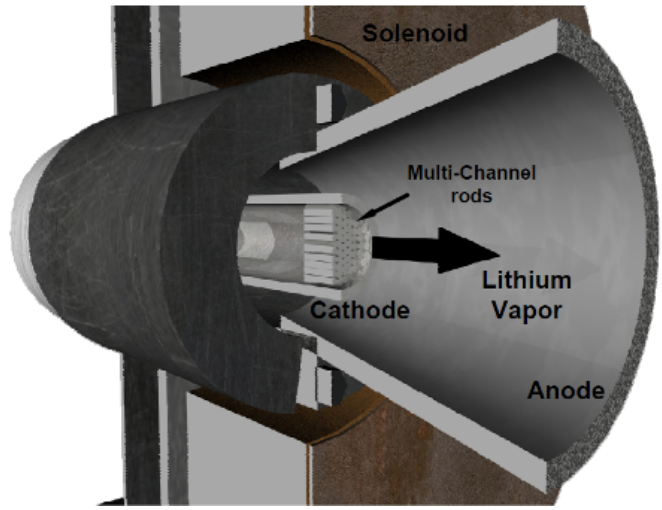

Figure 1.3: Cross-section illustration of the Lithium Lorentz Force Accelerator.

1.4 AF-MPDT Power Distribution

To estimate the efficiency of AF-MPDTs in general and the LILFA in particular one needs to examine the power distribution of a typical electric thruster as presented in Fig. 1.4[15]. The power to MPDTs can be divided into three main groups, the

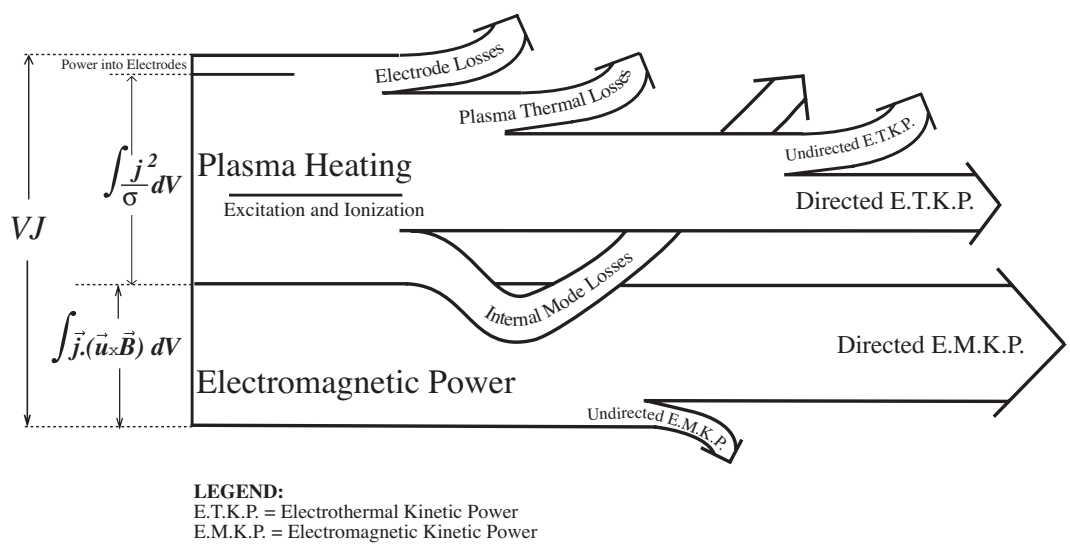

Figure 1.4: Power Distribution in MPD Thrusters. The relative sizes of the boxes are proportional to their common relative fraction found in literature.

electromagnetic power, the power to plasma heating which originates from resistive effects and the power dissipated in the electrodes and associated sheaths. The electro-

magnetic and plasma heating power components were shown to be $\int \bar{j} \cdot \left(\bar{u} \times \bar{B}\right) d\mathbf{V}$ and $\int j^2/\sigma d\mathbf{V}$ respectively[16].

Following Fig 1.4 the above three components can be further divided into the following components of power:

1. **Electromagnetic Kinetic Power.** This is the useful component of power which represents the power invested in the acceleration of the propellant. The electromagnetic kinetic power can be written as

$$P_{acc} = \frac{1}{2}\dot{m}u_e^2 = \frac{1}{2}\frac{\mathcal{T}^2}{\dot{m}} \tag{1.3}$$

   where the thrust is a function of the thruster's operational parameters and geometry ($\mathcal{T}(J, B, \dot{m}, r_a, r_c)$).

2. **Plasma Thermal Losses.** This component represents the power lost to raising the electrons, ions and neutral particles' temperatures. In MPDTs the ion and electron temperatures are of the same order of magnitude of $\sim O(1)\ eV$[17, 18]. To separate this component from the other resistive components it is conventional to regard the different species' temperatures after the propellant has been accelerated. This will enable the separation between power to plasma heating and power to propellant ionization.

3. **Internal Mode Losses.** This component represents the power invested in plasma ionization and excitation. It is also referred to as frozen flow losses and is not part of the acceleration process. In MPDTs ionization serves as an important energy sink as the acceleration time scale is shorter than the recombination time scale and the plasma is strongly to fully ionized throughout the thruster plume. At a microscopic time scale, like in many gas discharges, ionization is due to electron impact and is therefore affected by the energy

of the electrons in the discharge. However, it has been shown[19] that superthermal electrons attribute to plasma instabilities in the discharge which cause ionization. On a macroscopic level, the ionization losses can be tied to Joule heating effects where plasma instabilities are reflected in the enhancement of resistivity, also known as anomalous resistivity.

4. **Electrothermal Kinetic Power.** This component originates from thermal energy that is converted into kinetic energy, usually via a nozzle. Due to the low number densities associated with MPDTs of the order of less than $10^{20}\ m^{-3}$ this component is negligible in MPDTs[20]. The electrothermal component plays an important role only in the low current regime, which is of low interest since both the thrust and specific impulse are quite low at this regime.

5. **Electrode Losses.** This component represents the power invested in electrode heating, charge separation at the electrode sheaths and electron extraction from the electrodes.

   MPDTs rely on electron thermionic emission from the hot cathode for the supply of electron current density. Similarly, the anode absorbs energy from impinging electrons to emit secondary electrons from its surface. The "energetic price" of this emission is called the work function (ϕ_W). Due to the high temperatures associated with MPDTs the electrodes are usually made out of tungsten which has a work function value of $\phi_W = 4.54$ eV. It was mentioned earlier and will be discussed in this thesis that when lithium coats the surface of tungsten the work function value drops to about $\phi_W \simeq 2.5$ eV. This means that each electron impinging on the electrodes, per unit time, loses 2.5 eV to extract new electrons from the surface of the electrodes and maintain the discharge.

   Except for the power invested in thermionic emission from the electrodes' surface the power invested into maintaining the electrode sheaths charge separation

is a large power dissipation mechanism in MPDTs and is mostly dominated by the anode sheath voltage fall[21, 22, 23, 24]. The physics of this dissipation mechanism is still unclear and further investigation and modeling is required to elucidate how anode sheath voltage fall relates to the thruster's operational parameters (J,B,$\dot{m}$). In particular, in AF-MPDTs it was found that the anode sheath voltage fall is a function of the applied magnetic field (B) yet the electrons in the sheath can be shown to be unmagnetized[23, 24]. This contradiction is yet to be explained and requires additional experimental and analytical analysis. We will put a special effort in this thesis on characterizing this significant dissipation mechanism.

1.5 Voltage-Current Characteristics

The voltage-current, $V - J$, characteristics of the MPDT are important in evaluating the scaling of thrust efficiency in different operating regimes. The thrust efficiency is defined as the ratio of thrust power to total power,

$$\eta = \frac{P_{acc}}{P_{tot}} = \frac{\frac{1}{2}\dot{m}u_e^2}{P_{tot}}, \tag{1.4}$$

where P_{acc} is the power invested into plasma acceleration, $\dot{m}$ is the propellant mass flow rate and P_{tot} is the total power to the thruster. The total power is simply the product JV thus emphasizing the importance of the $V - J$ characteristics. Changing the applied current, mass flow rate, or applied magnetic field affects such plasma properties as the plasma resistivity and as a consequence, the exhaust velocity. This in turn changes the voltage required to sustain thruster operation, leading to variations in efficiency for different operational regimes.

It is useful to divide the different power dissipation components by the current

and regard the different power components as voltage components as follows:

$$\eta = \frac{P_{acc}}{P_{tot}} = \frac{P_{acc}}{P_{acc} + P_{res} + P_E} = \frac{V_{emf}}{V_{emf} + \frac{1}{j}P_{res} + V_E}. \tag{1.5}$$

Where V_{emf} is the electromotive voltage responsible for plasma acceleration, P_{res} is the resistive power that is invested in plasma heating, excitation and ionization and V_E is the voltage invested in the electrodes. In Eq. 1.5 the acceleration power is replaced by the electromotive voltage, V_{emf}, the resistive power, P_{res}, is simply divided by the total current and the electrode voltage falls and work function, V_E, are dealt with directly as voltages.

Analyzing the voltage-current characteristics of an MPDT is a conventional approach to efficiency analysis as the total voltage, which can be easily compared to other voltage components, represents the total power invested in the thruster and is plotted against current which is the main operational parameter of the thruster. We will adopt this approach in our thrust efficiency exploration.

1.6 Goal of Present Work

The ultimate goal of efficiency studies in AF-MPDTs is to learn how to maximize the efficiency. However the fundamental understanding of the different physical mechanisms affecting efficiency is not sufficient, at present, to accomplish this goal. What we have undertaken to achieve in this work is to gain a better grasp of the phenomenology of the different power dissipation mechanisms in the AF-MPDT. Using this understanding we strive to unravel the way efficiency depends on the thruster's operational parameters.

To do so we attempt to answer the following questions:

- *How does thrust efficiency change with the thruster's operational parameters?*

  We focus specifically on efficiency's dependence on applied magnetic field and

compare our results with the limited data taken in past studies on AF-MPDTs. From the obtained relations we attempt to deduce thruster design and operation criteria that will help in maximizing AF-MPDT efficiency.

- *What are the processes at work in the physics of anode sheath voltage fall?*
  Simply put, we are trying to understand and explain how different plasma parameters and material properties affect power dissipation in the anode sheath. Furthermore, we look for scaling relations for the anode sheath voltage fall as it varies with the thruster's operational parameters. In particular we attempt to explain the dependence of anode sheath voltage fall on the applied magnetic field. The insights from this examination are used to draw conclusions and establish design criteria for AF-MPDTs.

- *What are the dominant power dissipation components within different current regimes in AF-MPDTs?*
  Specifically we examine whether anode sheath power dissipation is dominant over a wide current range. For example, we expect resistive losses to dominate at low current values since frozen flow losses are embedded in resistive dissipation and ionization is expected to account for a large portion of the invested power. We focus our attention on the contribution that applied magnetic field has on the dominant power components interplay.

We approach the above questions using empirical and theoretical methods. Using the LiLFA we produce a large efficiency, anode sheath voltage fall and plasma parameters database as a function of the three operational parameters J, B and $\dot{m}$. The experimental results are used to formulate semi-empirical models for the thrust efficiency and the power dissipation components. We use both experimental data and physical models to draw conclusions for each of the above questions.

1.7 Structure of Thesis

We begin in chapter 2 by describing past research conducted on the LiLFA and other AF-MPDTs. We focus on different dissipation mechanisms found in these thrusters and their dependence on the thruster's operational parameters. In chapters 3 and 4 we describe the facility, apparatus, methods and diagnostics used to conduct our experimental investigation using the LiLFA. We move on to chapter 5 where we present the experimental results obtained for our efficiency exploration followed by an analysis of the observed results. In that analysis we identify different trends, scaling relations and postulate on the physics behind them. In chapter 6 we present a model for the main power dissipation mechanism in the thruster, the anode sheath voltage fall. The model is compared to the experimental data presented in chapter 5 and physical insights are drawn from the relations between anode sheath voltage and the operational parameters. In chapter 7 we formulate a thrust efficiency model by using voltage-current characteristics data obtained in chapter 5 and the semi-empirical anode sheath voltage fall model formulated in chapter 6. Efficiency curves are plotted against the operational parameters and the physical mechanisms at work are discussed. Finally, in chapter 8 we summarize the important findings of this work, draw conclusions on the physical insights obtained and discuss open questions raised in the process.

Chapter 2

Review of Past Research

This chapter reviews past theoretical and experimental work that is relevant both to understanding thruster efficiency and total thruster voltage in AF-MPDTs and self-field MPDTs. While past research focused mainly on individual power dissipation mechanisms it is still lacking a global view of the combined contribution of these mechanisms to the determination of efficiency. Except for one research group (Tikhonov et al.[8]), no particular effort was made to extensively repartition and characterize all the various power components taking part in AF-MPDT operation. As a consequence, the past research reviewed here focuses mainly on *particular* power dissipation mechanisms as opposed to full investigations of *all* power dissipation mechanisms. In addition, the work conducted in studying efficiency in AF-MPDTs is mostly experimental, where the efficiency is determined from thrust, mass flow rate and total thruster power measurements.

The main purpose of this chapter is to summarize the findings that exist in AF-MPDT efficiency literature, determine major trends of AF-MPDT power and efficiency with the thruster's operational parameters and identify research questions that still need to be answered.

Since the literature on power and efficiency studies in AF-MPDT is quite extensive

we choose to review past research that is most relevant to the work of this thesis. This review is arranged by research group with the major group findings summarized at the end of each section. At the last section of this chapter we describe the relevance of past research to the study presented in this thesis and pose open questions paramount to the investigation conducted in this thesis.

2.1 Review of Research at Moscow Aviation Institute (1993-1998)

The research performed at Moscow Aviation Institute (MAI)[8, 25, 26, 27, 28, 29, 30, 31, 32, 33], led by Tikhonov, is the most extensive and comprehensive experimental effort undertaken to study the general physics of steady state AF-MPDTs. The work at MAI was conducted on three different lithium-fed AF-MPDTs at three different power levels which are 30 kW, 130 kW and 200 kW (Fig. 2.1). All thrusters have multi-channel hollow cathodes through which the propellant is injected. The experiments' operational regime involves current levels of up to 3 kA, applied magnetic fields up to 0.112 T and mass flow rate values of up to 120 mg/s.

A replica of a 30 kW thruster used by MAI was made and transferred to Princeton university in 1998 and is the thruster used in the study presented in this thesis. The research at MAI focused on the measurement and investigation of thrust and total voltage that were used to estimate efficiency. In addition the research involved measurements of the electron temperature in different regions of the thruster, electrode temperature, and electrode erosion rates.

The main conclusions drawn from this research are:

- Efficiency was experimentally shown to be in the range of 20% to 45% and exhibited an increase with current and applied magnetic field while showing a decrease with increasing mass flow rate. The qualitative trends of thrust,

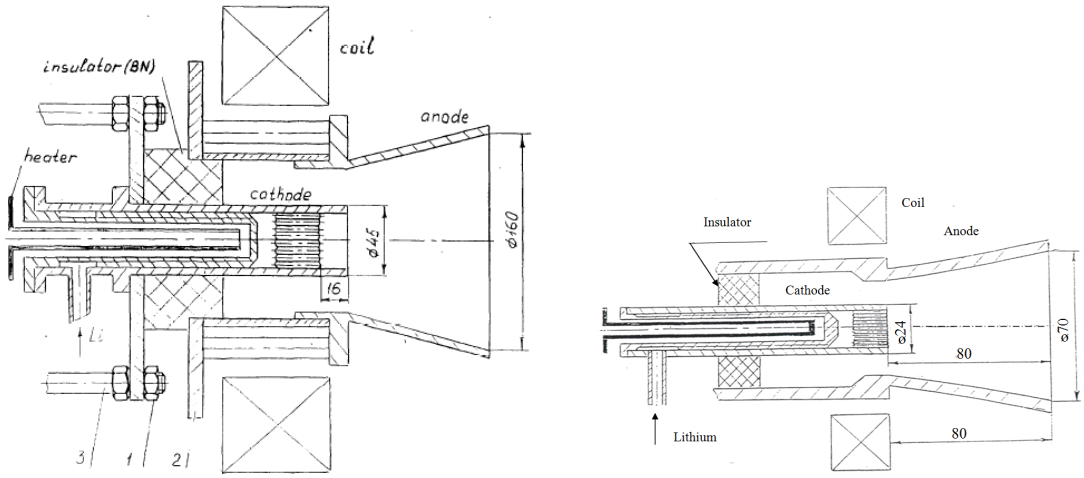

(a) The 130 kW LiLFA

(b) The 30 kW LiLFA

Figure 2.1: Schematics of the (a) 130 kW and (b) 30 kW LiLFA thrusters built and tested at Moscow Aviation Institute (A schematic of the 200 kW LiLFA is not available). All dimensions are in millimeters

total voltage and efficiency with the operational parameters were published in Ref.[26] and are presented in Fig. 2.1.

In general, efficiency was shown to increase with total thruster power.

- Thrust in AF-MPDTs can be characterized in the following semi-empirical formula:

$$\mathcal{T}(J) = K_{self}J^2 + K_H(2r_a)B_aJ + K_{gd}\dot{m}a_0. \tag{2.1}$$

Here $\mathcal{T}(J)$ is the thrust which is a function of total current, r_a is the anode radius, B_a is the applied magnetic field at the anode face, a_0 is the sonic speed at the cathode exit and the constants K_{self}, K_H and K_{gd} are to be determined by experimental measurements conducted on a particular thruster. The operational current regime of AF-MPDTs is in the range in which $K_H(2r_a)B_aJ$ is the most dominant term in the thrust formula since it represents the contribution and effect of the applied field to thrust. A detailed explanation of Tikhonov's thrust model will be given in chapter 7.

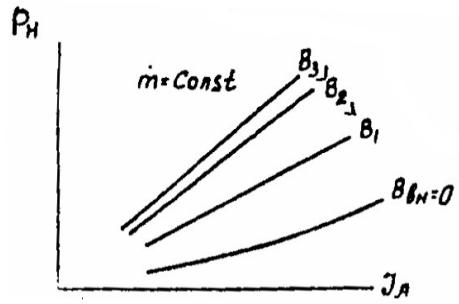

(a) Thrust vs. Current

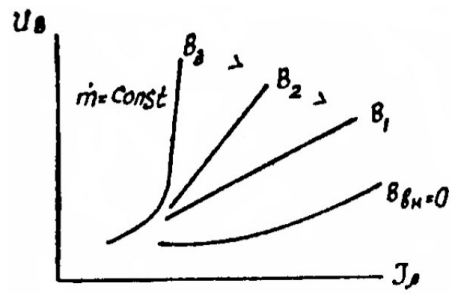

(b) Voltage vs. Current

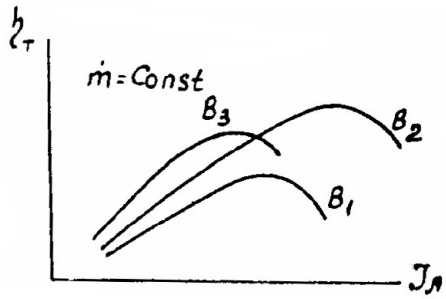

(c) Efficiency vs. Current

Figure 2.2: Qualitative trends in (a) thrust, (b) voltage and (c) efficiency as a function of discharge current as investigated by Tikhonov et al. at MAI

- Voltage in AF-MPDTs can be modeled by the following semi-empirical formula:

$$V_{tot} = \frac{\mathcal{T}^2}{2\dot{m}J} + \frac{\beta_i e \left(\epsilon_i + 2\frac{k_B T_e}{e}\right) N_A \dot{m}}{\mu_{pl} J} + \phi_W + V_c + 2\frac{k_B T_{e,A}}{e} + V_a \tag{2.2}$$

where β_i is the ionization coefficient which is a fit parameter, ϵ_i is the ionization energy, N_A is Avogadro number, μ_{pl} is the molecular weight of lithium plasma, V_c is the cathode sheath voltage fall, ϕ_W is the anode work function, $T_{e,A}$ is the electron temperature in the anode layer and V_a is the anode sheath voltage fall. One of the main disadvantages of this model is the fact that it relies on experimental knowledge of the plasma properties within a specific thruster. Specifically the anode sheath voltage fall, V_a, which can be a significant fraction of the total voltage, dependence on the thruster's operational parameters is unknown. In addition, most voltage data were obtained at a variety of current

values but only three values of applied magnetic field and several values of mass flow rate.

- The electron temperature was measured to be 1.5 eV at the cathode exit and about 2 eV in the anode layer region. This knowledge will be used in our study since the electron temperature measurements were taken on the same thruster used in the study presented in this thesis.

The work conducted by Tikhonov et al. sets the framework for the understanding of the fundamental physics of AF-MPDTs. It relates the plasma properties to thruster performance parameters and sets some basic operational limitations.

Comments: Tikhonov et al. demonstrated the basic scalability of thrust and voltage in AF-MPDT along with identification of the different current regimes that affect thrust production. He showed that AF-MPDT operation is possible at a variety of power levels and geometries and proved that it is more efficient than self-field MPDTs. Tikhonov et al. also demonstrated the high efficiency and low erosion rate that correspond to using lithium propellant and multi-channel hollow cathode. Lastly, Tikhonov et al. measured plasma and thruster properties that can aid future investigation and characterization of AF-MPDT operation.

2.2 Review of Research at Alta's Electric Propulsion Group in Pisa, Italy (2001-2003)

The research conducted at 'Alta', Pisa in Italy[12, 26, 34, 35], led by Andrenucci and Paganucci, is an ongoing experimental effort to characterize quasi-steady AF-MPDT performance as it varies with the thruster's operational parameters. Quasi-steady MPDT operation is an operational mode of several milliseconds which is sufficient to emulate steady-state operation as the plasma transport time scale is of the order of

several microseconds. The AF-MPDT used at 'Alta' is a quasi-steady argon thruster with about 90% propellant injection from a hollow cathode and 10% injection from the anode wall. The experiment's operational regime involves current levels of up to 15 kA, applied magnetic field up to 0.08 T and mass flow rate values of up to 660 mg/s. The operational regime corresponds to instantenious power of about 400 kW.

The research conducted at 'Alta' demonstrated the usefulness of adding an applied magnetic field to MPDTs in general and quasi-steady MPDTs in particular. It was shown that the addition of applied field increases the thrust and efficiency of MPDTs (Fig. 2.2). The general trends of thrust and efficiency with current were measured and Tikhonov's thrust model was verified with the experimental data. In addition, the measurements span over three values of applied magnetic field and two values of mass flow rate, so no conclusive remarks could be made regarding the scaling of the efficiency with applied magnetic field and mass flow rate.

The research at Alta also involved measurements of the electron temperature, T_e, and plasma density, n_e, at two different radial positions in the thruster using a triple Langmuir probe. The measurements showed an electron temperature range of around 6 eV, which is significantly higher than that measured in other labs. The electron temperature was found to slightly decrease with increasing radius. The measurements also showed a plasma density range of about 10^{20} m^{-3} with a density decrease with the radius. These measurements give a general sense of the range of electron temperatures and plasma densities in the thruster and their qualitative change with radial position.

Comments: The research group at Alta demonstrated the benefits of adding an applied magnetic field to MPDTs. This experimental work corroborates with the research conducted at MAI and was used to verify that Tikhonov's thrust model is valid for quasi-steady argon thrusters. Lastly, the research conducted at Alta add to the knowledge of plasma properties in AF-MPDTs which can be used in future modeling and research.

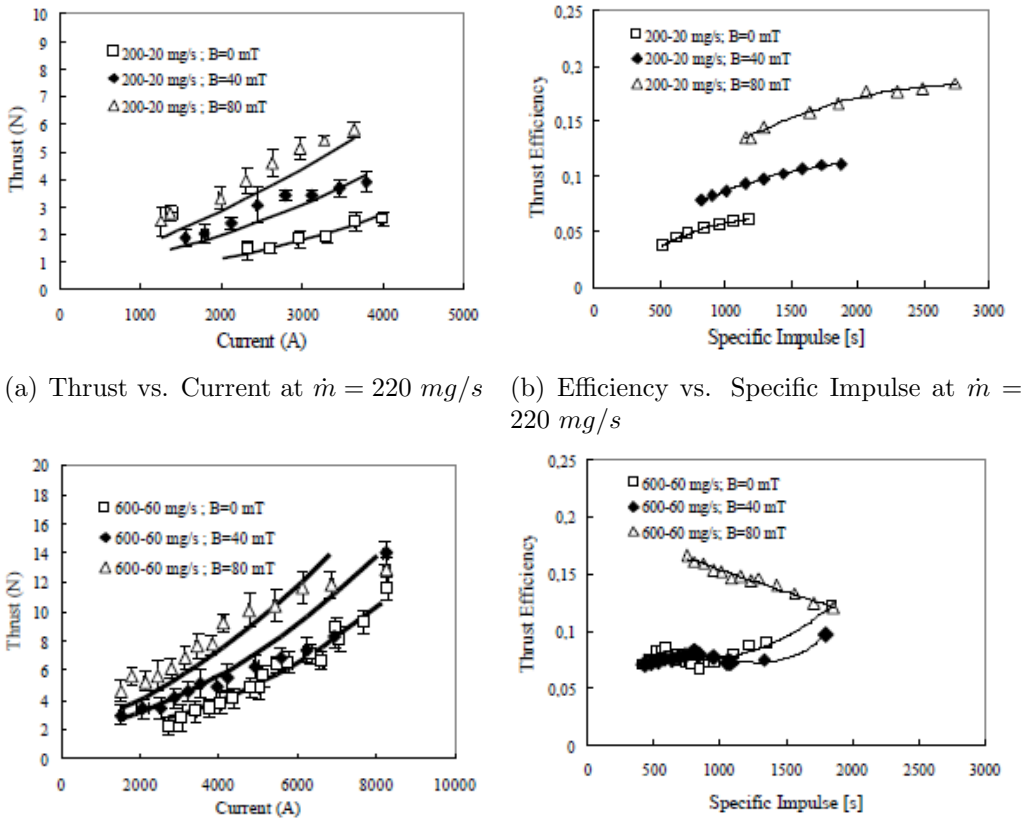

(a) Thrust vs. Current at $\dot{m} = 220\ mg/s$

(b) Efficiency vs. Specific Impulse at $\dot{m} = 220\ mg/s$

(c) Thrust vs. Current at $\dot{m} = 660\ mg/s$

(d) Efficiency vs. Specific Impulse at $\dot{m} = 660\ mg/s$

Figure 2.3: Experimental data of thrust and efficiency obtained at Alta in Pisa, Italy. The solid lines in the figures for thrust correspond to Tikhonov's thrust formula (Eq. 2.1) with $K_{self} = 1.33 \times 10^{-7}$, $K_H = 0.1$ and $K_{gd} = 1.6$

.

2.3 Review of Research at NASA Lewis Research Center (1989-1994)

The research conducted at 'NASA Lewis' research center in Ohio[23, 24, 36, 37, 38], led by Myers, was an extensive experimental effort to characterize both thrust and efficiency in AF-MPDTs. The experiments conducted at 'NASA Lewis' aimed at revealing the scaling of different performance parameters with the operational parameters and thruster geometry. In addition, a special experimental effort was made to characterize the main power dissipation mechanism in AF-MPDTs - the anode

sheath voltage fall. The AF-MPDTs used at 'NASA Lewis' were steady-state argon AF-MPDTs with a back wall propellant injection for all geometrical configurations (Fig. 2.3). The experiment's operational regime involved current levels of up to 2000 A, applied magnetic field levels up to 0.4 T and mass flow rate values of up to 160 mg/s. The operational regime corresponds to a maximum power of about 70 kW.

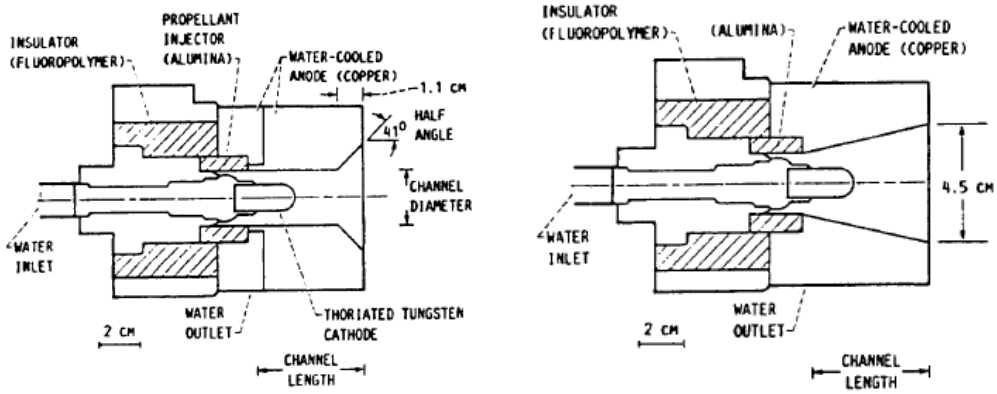

(a) Geometry A

(b) Geometry B

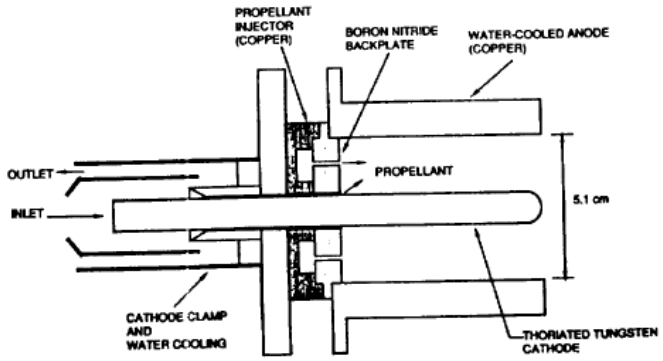

(c) Geometry C

Figure 2.4: The three different geometries investigated by Myers et al. at the 'NASA Lewis' research center

The research conducted by Myers et al. at 'NASA Lewis' demonstrated the scaling relation for thrust also observed at MAI and 'Alta', that is, $\mathcal{T} \propto JB$ except for high currents. In addition, the research showed the geometrical dependence of both thrust ($\mathcal{T} \propto r_a$) and total voltage ($V_{tot} \propto r_a^2$) which was similar to the dependence observed by Tikhonov et al. Myers et al. showed that the scaling of thrust and total voltage changes within different current regimes thus reflecting different acceleration

mechanisms. He postulated that the low current region in his study is dominated by the applied magnetic field while the high current region is dominated by self field. According to Myers et al. each regime is defined according to thruster current, geometry and mass flow rate.

The study conducted on the scaling of anode sheath voltage fall, V_a, with the operational parameters, using an array of floating Langmuir probes, was the first experimental effort of this important aspect of AF-MPDT operation, power dissipation and produced important conclusions:

- V_a increases linearly with thruster current, J.
- V_a increases linearly with applied magnetic field, B.
- V_a decreases with increasing mass flow rate, $\dot{m}$.
- V_a increases quadratically with anode radius, ($V_a \propto r_a^2$).

An example of the data demonstrating the first two conclusions is presented in Fig. 2.5

The above conclusions added to the understanding of the anode sheath power dissipation mechanism in AF-MPDTs. However, no theoretical endeavor was made to explain the physics behind this mechanism. As a consequence, the dependence of the anode sheath voltage fall, V_a, on the applied magnetic field remains unexplained. This dependence poses a problem since the electrons in the anode sheath are unmagnetized ($\lambda_{De} \sim 10^{-6}$ m, $r_L \sim 10^{-4}$ m) thus ostensibly, V_a should not be dependent on the applied magnetic field. Myers et al. suggests that this scaling with applied field is due to the influence of the applied field on the electron Hall parameter in the anode region. Nevertheless, the physical reason behind it remains unexplored.

In addition, Myers et al. measured the electron temperature and plasma density in the plume of AF-MPDTs using a triple probe. Plume temperatures of 1.5-2.5 eV were

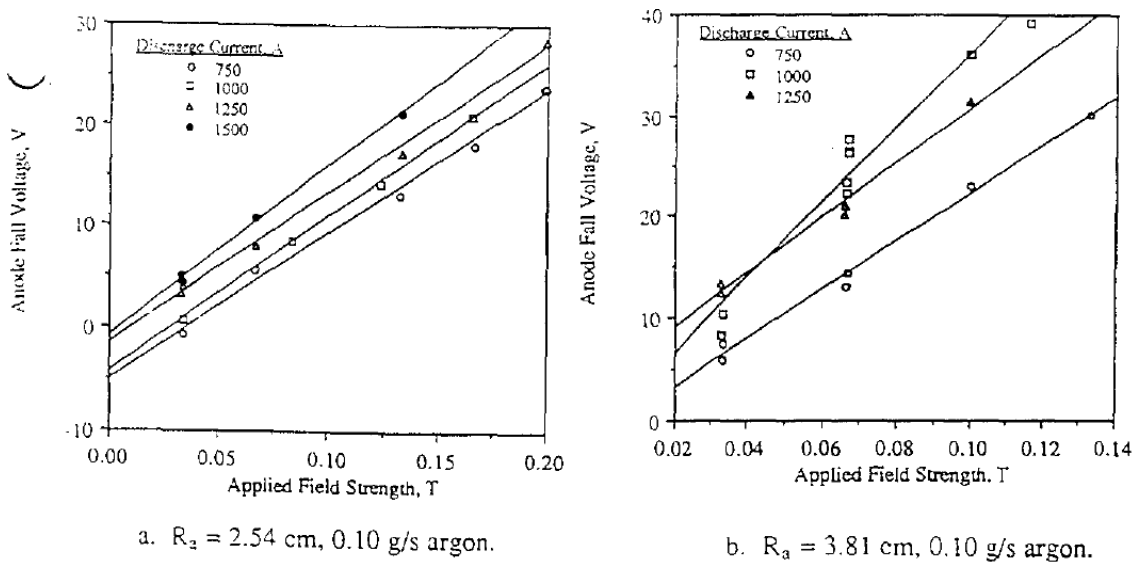

a. R_a = 2.54 cm, 0.10 g/s argon.

b. R_a = 3.81 cm, 0.10 g/s argon.

Figure 2.5: Anode sheath voltage fall plotted against (a) thruster current and (b) applied magnetic field as measured by Myers et al. for $\dot{m} = 100\ mg/s$ of argon in two different thruster geometries ($r_a = 2.54\ cm$ and $r_a = 3.81\ cm$)

found to weakly decrease with axial position and to be independent of the applied magnetic field. Electron density measurements indicated an average plasma density of about $10^{19}\ m^{-3}$ at the thruster's centerline with a sharp radial decrease of a few orders of magnitude in the near anode region.

Comments: The research conducted by Myers et al. at 'NASA Lewis' research center corroborates the findings at MAI and 'Alta' previously presented by alluding to the same thrust scaling relations. The measurements of anode sheath voltage fall are useful for the basic understanding of the main power dissipation mechanism in AF-MPDTs. These measurements can help in the validation of future anode sheath voltage fall measurements and in the formulation of scaling relations for thrust efficiency. Nevertheless, the study conducted by Myers et al. did not present a theoretical explanation and physical description of the processes at play in the determination of thrust efficiency.

2.4 Review of Research at Stuttgart University (1967-1998)

The research performed at Stuttgart university[39, 40, 41], led by Krülle, was an experimental and theoretical effort to characterize both thrust and efficiency of AF-MPDTs. Krülle et al. attempted to theoretically derive the scaling relations of thrust and efficiency in AF-MPDTs as well as experimentally verify these relations. The AF-MPDT used at Stuttgart university is a steady-state thruster with back wall propellant injection of either argon or helium. The experiment's operational regime involves current levels of up to 1.2 kA, applied magnetic field up to 0.25 T and mass flow rate values of up to 220 mg/s. The operational regime corresponds to a maximum thruster power of about 100 kW.

In his theoretical model Krülle et al. assumed that thrust is generated by conversion of azimuthal momentum of swirling plasma into axial momentum via a magnetic nozzle effect. By using the resistive MHD approach, treating the plasma as a rigid body (the swirling angular velocity is constant), and making a few simplifications of current distribution patterns, Krülle et al. were able to form theoretical scaling relations for thrust, $\mathcal{T}$, and its dependence on operational parameters. Also, Krülle et al. assumed that the plasma swirling is due to $\bar{E} \times \bar{B}$ drift, allowing for scaling relations for the radial electric field and total voltage, V_{tot}.

The final theoretical scaling relations are:

$$\mathcal{T} \propto JB_c^2 r_a^2, \tag{2.3}$$

$$V_{tot} \propto \frac{JB_c^2 r_a^2}{\dot{m}}, \tag{2.4}$$

$$\eta \propto JB_c^2 r_a^2. \tag{2.5}$$

The scaling relations for thrust and efficiency demonstrate how each increases with current and applied field. These scaling relations are not similar to the ones found experimentally by Tikhonov et al. In addition, the scaling relation for efficiency lacks the dependence on mass flow rate which was also observed experimentally by Tikhonov et al.

Experimentally Krülle et al. found a linear increase in both thrust and efficiency with current and applied field. In addition, Krülle et al. found no dependence of thrust on mass flow rate.

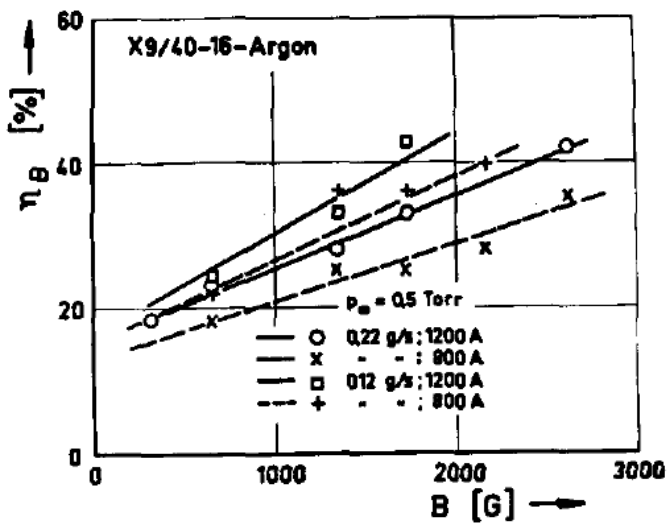

Figure 2.6: Efficiency vs. applied magnetic field for different current and mass flow rate values as measured by Krüle et al.

Using the experimental results and the theoretical analysis Krülle et al. drew the following conclusions:

- Azimuthal acceleration and conversion through the magnetic nozzle plays an important role in thrust generation in AF-MPDTs.
- The work done by the axial forces of $\left(\bar{j} \times \bar{B}\right)$ should be further investigated.
- Thrust and efficiency are independent of mass flow rate or the type of propellant used.

Comments: The research conducted by Krülle et al. at Stuttgart university adds to the understanding of the acceleration and energy conversion mechanisms in AF-MPDT. The basic theoretical scaling relations for thrust and total voltage with current are in agreement with the trends measured in other facilities yet the dependence on the applied magnetic field is different as the thrust and total voltage are quadratic with B_c and not linear.

2.5 Review of Research at Tohoku University (1991-2007)

The research performed at Tohoku university[18, 42, 43], led by Ando, is an extensive and elaborate experimental effort to characterize the spatial distribution of magnetic fields, $\bar{B}$, current densities, $\bar{j}$, and force densities, $\bar{f}$, in AF-MPDTs. In this research Ando et al. also measured the velocity vector, $\bar{u}$, perpendicular to the magnetic field ion temperature, $T_{i\perp}$, plasma density radial distribution, $n_e(r)$, and electric potential radial distribution in the interelectrode region, $\phi(r)$. Although the research did not aim to calculate or characterize the thrust efficiency, it contributes greatly to the understanding of the fundamental physical mechanisms in AF-MPDTs.

The AF-MPDT used at Tohoku university is a quasi-steady helium AF-MPDT with a back wall propellant injection. The experiment's operational regime involved current levels of up to 10 kA, applied magnetic field up to 0.1 T and mass flow rate values of up to 100 mg/s. The operational regime corresponds to a maximum power of almost 2 MW.

By performing and using the different measurements mentioned above several important conclusions, relevant to the study of this thesis, were drawn:

- Plasma pinching dominates thrust production in AF-MPDTs since the dominant force density is radial towards the cathode ($f_r \gg f_z$) and is converted to

thrust via pressure on the cathode or back wall.

- The plasma density radial distribution, $n_e(r)$, has a Gaussian shape with the maximum density at the thruster's centerline.
- The plasma potential radial distribution, $\phi(r)$, in the interelectrode region is parabolic, that is $\phi(r) \propto r^2$.
- The radial velocity, u_r, is negligible compared to the axial and azimuthal velocities.

Comments: The research conducted at Tohoku university can help in the development of future efficiency models by adding to the understanding of the physics in AF-MPDTs. The conclusions presented here will help in the formulation of several of the assumptions in the models presented in this study.

2.6 Review of Other Studies

AF-MPDTs have been the subject of research for many research groups attempting to theoretically, experimentally or numerically characterize the physics behind thrust generation, efficiency determination and plasma properties in these thrusters. In addition, elaborate studies on the different power dissipation mechanisms in self-field MPDTs were conducted and should be noted here.

Mikellides and Turchi[44] formulated theoretical thrust and total voltage models based on the assumption that the azimuthal force density is balanced by viscous forces. This assumption implies that the acceleration mechanism in AF-MPDTs is thermal. Mikellides and Turchi also derived the following scaling relations: $\mathcal{T} \propto \sqrt{JBr_a}$ and $\eta \propto Jr_a/\dot{m}$ which are not in agreement with the experimental data obtained at MAI, 'Alta', 'NASA Lewis' and Stuttgart university. Therefore, we can conclude from this

study that it is doubtful that the acceleration mechanism in AF-MPDTs is thermal due to viscous heating.

Fradkin formulated[17] theoretical thrust and total voltage models assuming that the plasma rotates as a rigid body at a constant angular velocity. Fradkin also assumed that the rotational energy is converted completely into axial energy. Using these two assumptions Fradkin showed that the thrust and total voltage can be written as follows:

$$\mathcal{T} \propto JB_c r_a, \tag{2.6}$$

$$V_{tot} = V_0 + 1.88\frac{B_c^2 J r_a^2}{\dot{m}} \tag{2.7}$$

where V_0 is voltage due to electrodes and resistive losses. Fradkin was able to analytically produce the same scaling relations observed in previous research, but he did not characterize V_0 and its scalability with the operational parameters. For this reason no expression was derived for AF-MPDT efficiency.

Since the number of studies of anode sheath voltage fall physics in AF-MPDTs is limited we review some of the self-field MPDT literature relevant to the study presented in this thesis. These studies come to investigate the anode sheath voltage fall phenomena and can aid in the understanding of this phenomenon in AF-MPDTs.

Saber[45], Gallimore[22] and Diamant[21] investigated the anode phenomena in self-field MPDTs. Saber showed experimentally that the anode power deposition is the largest power dissipation mechanism in AF-MPDTs in the power range 0.2-20 MW. He demonstrated reduction of anode power fraction with increased thruster power. Saber speculated this behavior to be influenced by collisional processes in the near anode region, yet outside of the anode sheath region. In addition, Saber measured the electron temperature in the near anode region to be around 1 eV.

Similarly, Gallimore found experimentally that anode sheath voltage fall is the most significant contributor to anode power deposition in the power range of 1.9-7 MW. He observed that an increase in thruster current leads to an increase in anode sheath voltage fall and a decrease in the anode power deposition fraction. Gallimore experimentally showed that this phenomenon is correlated with the electron Hall parameter, Ω_e, in the near anode region.

Diamant demonstrated, in the power range of 0.32-4 MW, an increase of the anode voltage fall with the normalized ionization current ($\xi \propto J/\sqrt{\dot{m}}$) which is the discharge current normalized by the current required to accelerate the plasma to the critical ionization velocity[46]. This finding corroborates Gallimore's findings. Diamant also found in the near anode region electron temperatures of 1-2 eV as well as density reductions, relative to a distance 5 mm from the anode wall (r_a=50 mm), of more than an order of magnitude. All of the above findings and observations in the study of anode phenomena in self-field MPDTs lead to the following conclusions:

- Anode sheath voltage fall increases with increasing current.
- Anode deposition power fraction reduces with increased current and power to the thruster.
- The physical processes leading to a variation of the anode sheath voltage fall with operational parameters are likely to be in the near anode region yet outside of the anode sheath.
- The electron temperature in a wide power range is fairly constant in the range of 1-2 eV.
- It is likely that there is a correlation between the self-induced magnetic field and anode sheath voltage fall. An increase in the former leads to an increase in the latter.

These conclusions can aid in the formulation of assumptions for future models for anode sheath voltage fall and anode power deposition. In addition, any qualitative conclusions drawn from experimental data of anode sheath voltage fall in AF-MPDTs should be compared to the conclusions above.

2.7 Summary of Relevant Research

In this chapter we have presented the results of past experimental and theoretical studies that aimed at finding expressions or scaling relations for thrust and efficiency. We have also presented past endeavors for characterizing the anode power dissipation mechanism in both AF-MPDTs and self-field MPDTs. Lastly, we have shown experimental evidence from past research for the values of some of the plasma properties and their dependence on various spatial and thruster parameters. All the experimental data taken on AF-MPDTs can be summarized as in Table 2.1.

Research Group	**Propellant**	**Power** P_{tot} [kW]	**Current** J [kA]	**Applied Field** B_c [T]	**Mass Flow Rate** $\dot{m}$ [mg/s]	**Electron Temperature** T_e [eV]	**Plasma Density** n_e $[m^{-3}]$
MAI	Li	30, 130, 200	0.4-3	0.112	8-120	1.5-2	
Alta	Ar	400	1-15	0.08	220-660	6	10^{20}
NASA Lewis	Ar	70	0.75-2	0.4	100-160	1.5-2.5	10^{18}-10^{19}
Stuttgart	Ar, He	100	0.6-1.2	0.25	60-220		
Tohoku	Ar, He	2000	3-9	0.1	100	1-2.5	10^{20}

Table 2.1: Comparison between operational parameters and measured data for different research groups for AF-MPDTs

From all of these past experimental and theoretical studies we can reach the following conclusions:

- Thrust, $\mathcal{T}$, increases linearly with current, J, and applied magnetic field, B.
- Efficiency, η, has a general increase with current and applied magnetic field.
- Anode power deposition is the largest contributor to MPDT power dissipation.
- Relative anode power deposition reduces with increasing thruster power.
- Anode sheath voltage fall, V_a, increases linearly with thruster current, J.
- V_a increases with applied magnetic field, B. More data is required to determine the scaling relation.
- V_a decreases with increasing mass flow rate, $\dot{m}$.
- V_a increases quadratically with anode radius, r_a.
- It is possible that there is a correlation between the magnetic field in the near anode region and the anode sheath voltage fall.
- Electron temperature, T_e, in the near anode region is in the range 1-2 eV, for a variety of propellants, regardless of the total thruster power.
- Plasma density, n_e, is reduced by a few orders of magnitude in the near anode region compared with the density at the center of the thruster. The density also has a radial Gaussian distribution with the maximum at the thruster centerline.
- It is likely that the radial force density is significantly larger than axial force density.

These conclusions aid our study in two ways: 1) Any experimental data, conclusions drawn or models formulated will be compared to past findings. 2) Several of

the conclusions aid in forming assumptions for an efficiency model presented in this thesis.

Although the above conclusions contribute to the general understanding of efficiency of AF-MPDTs, we must remember that the goal of this thesis is to understand efficiency determination in AF-MPDTs as well as the physics behind the various power dissipation mechanisms. To accomplish this goal the studies reviewed here require further investigation due to the following reasons:

- Tikhonov et al. studied AF-MPDT efficiency in a wide total current range yet not in a wide enough variety of applied magnetic field or mass flow rate values to achieve the goal of this thesis. For this reason no definitive conclusions were drawn on the scaling of voltage or efficiency as a function of the operational parameters. In addition, Tikhonov et al. did not fully explain the physics or demonstrated the scaling relations for all the power dissipation mechanisms in AF-MPDTs. To add to the research conducted at MAI more experimental research is required to complete the investigation in a wide operational parameter space.

- The electron temperature and number density measurements taken at Alta are not sufficient to draw global conclusions regarding the radial variation of T_e and n_e due to the limited number of measurements made. In addition, the research at Alta is experimental without any attempts to model or find conclusive scaling relations for the various power dissipation mechanisms or efficiency. In order to achieve the goal of this thesis there is a need to produce data in a wider parameter space.

- The study conducted by Myers et al. is experimental and additional theoretical study is needed to complete the picture of anode sheath voltage fall in AF-MPDT.

- The limited number of experiments and data points taken by Krülle et al. in Stuttgart prevent the drawing of any conclusive remarks on the mathematical scaling of efficiency with the operational parameters (Fig. 2.6) which is required to achieve the goal of this thesis. Also, the experimental data obtained by Krülle et al. point to the same scaling relations presented by MAI, Alta and 'NASA Lewis' research groups yet the exact mathematical dependence is not conclusive due to the lack of experimental data at a wide variety of current and mass flow rate values. Lastly, Krülle et al. did not attempt to investigate the various power dissipation mechanisms in AF-MPDTs. Thus, they did not make any conclusions on the scaling of efficiency at different current or applied field regimes.

In conclusion, to achieve the goal of this thesis the studies reviewed here lack the detailed explanations of the physical mechanisms in different operational parameter regimes. the experimental data from all of the above studies span too narrow of an operational parameter space to draw strong conclusions on scaling relations for efficiency. Therefore, there is a need for both additional experimental and theoretical investigations in order to properly characterize efficiency and elucidate the physical processes at work behind efficiency determination in AF-MPDTs.

Chapter 3

Experimental Apparatus

This chapter describes the facility and apparatus used to conduct the experiments and operate the lithium thruster (LiLFA). These include the facility's infrastructure, vacuum system, thruster, thruster subsystems, lithium feed system, lithium loading apparatus, power requirements and safety requirements.

3.1 General Experimental Layout

The general experimental layout is illustrated in Fig. 3.1. All the experiments were conducted at Princeton University at the **S**teady **S**tate **L**ow **P**ower **F**acility (SSLPF). The thruster is located at the front end of the vacuum chamber. The vacuum chamber allows the accommodation of intrusive diagnostics such as the emissive Langmuir probe, and non-intrusive optical diagnostics, such as a spectrometer and optical pyrometer, which have access to the thruster throughoptical access ports as shown in Fig. 3.1. All power to the thruster and its subsystems is provided by dedicated power supplies located in the facility's basement and on the main floor. The lithium loading prior to each experiment is performed in a glove box located near the vacuum chamber on the ground floor.

Each thruster operation requires at least three human operators: one at the control

and diagnostic computer, one at the thruster current control unit and one next to the glass window with a direct line of sight to the thruster during operation. Each one of the other diagnostics (emissive probe, optical pyrometer and spectrometer) require another human operator. In a typical experiment about six human operators are needed for the entire duration of the experiment.

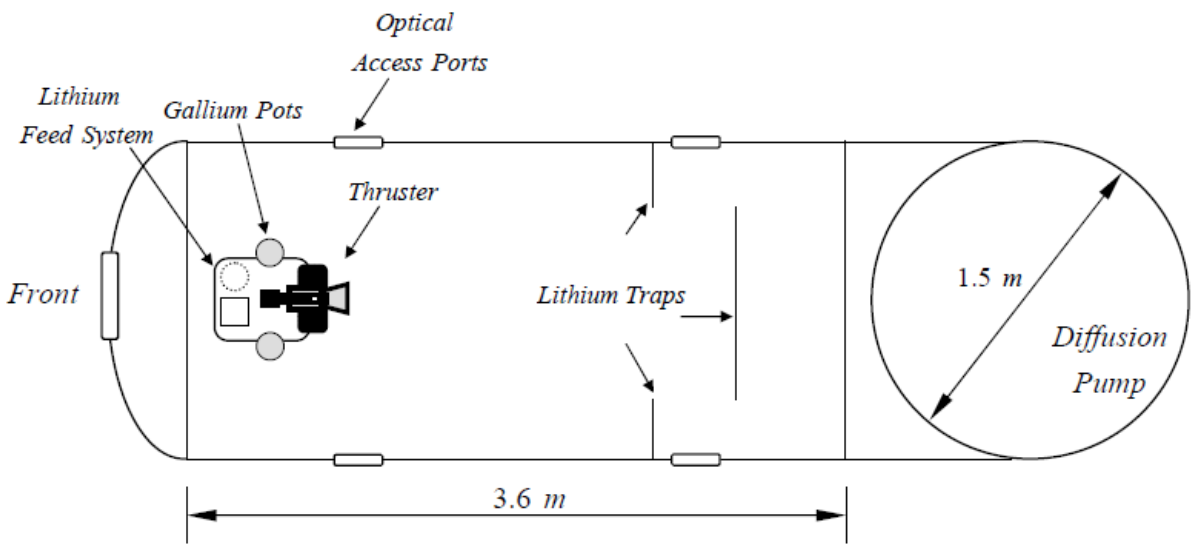

Figure 3.1: General layout of the experimental test facility.

3.2 Steady State Low Power Facility

The SSLPF consists of a vacuum chamber, pumping system and cooling liquid system. The cylindrical-shaped steel vacuum chamber, illustrated in Fig. 3.1, is 1.5 m in diameter and 3.6 m in length. It is designed to support steady state operation at up to 100 kW and is suitable for operation with high temperature lithium. The ultimate vacuum of this system is 1.7×10^{-5} Torr (2.266×10^{-3} pa) and is obtained using a 1.22 m CVC Type PMC-48C (95,000 l/s) diffusion pump, a Leybold Vacuum Products Inc. RUVAC WSU-2000 1342 CFM (630 l/s) Roots blower, and a 150 CFM (71 l/s) Stokes Microvac mechanical pump. All three pumps are connected to the vacuum chamber in series. Low pressure is easily maintained during thruster operation because lithium is

a solid at room temperature, and therefore condenses on the inner walls of the vacuum chamber. For this reason, pressure can be kept near ultimate vacuum during thruster firing. Pressure is measured using two pressure gauges. In the range of 760 Torr to one mTorr, pressure is measured using a Terranova model 906 convection gauge; below one mTorr, pressure is measured using an MKS 943 cold cathode gauge.

Tubes welded to the inside walls of the chamber conduct coolant at a rate of 0.6 l/s to maintain a moderate temperature on those walls. The cooled inner walls are covered with 0.002″ aluminum foil, held in place with flexible magnetic strips, on which lithium vapor condenses. After each experiment, during the cleanup procedure, the aluminum foil and magnets are removed from the walls and disposed of. Two fixed aluminum, water-cooled panels mounted at the back of the vacuum chamber and serve as lithium traps, thereby preventing lithium vapor from reaching the diffusion pump and contaminating it. Two smaller, removable aluminum panels mounted next to the back port covers (windows) also serve as lithium traps to prevent contamination of the lithium feed system and tank entrance area. A second closed-loop cooling system is used to keep the thrust stand and subsystems at reasonable temperatures so that wiring insulation and other components will not be damaged by high heat. It is also used for thermal control of the feed system by cooling the lithium cylinder walls and sealing the lithium freeze valve during thruster operation (See section 3.6). This closed-loop cooling system circulates a 50% Dowfrost, 50% water mixutre at a maximum flow rate of 50 g/s to each of 6 separate loops using a StaRite high-head pressure centrifugal pump. The heat absorbed by the closed-loop cooling system is transferred to Princeton's process chilled water system through two Swep North-America Inc., models 10046-030 and 10002-026, heat exchangers connected to Princeton University's process chilled water system, which delivers water at about $15°C$.

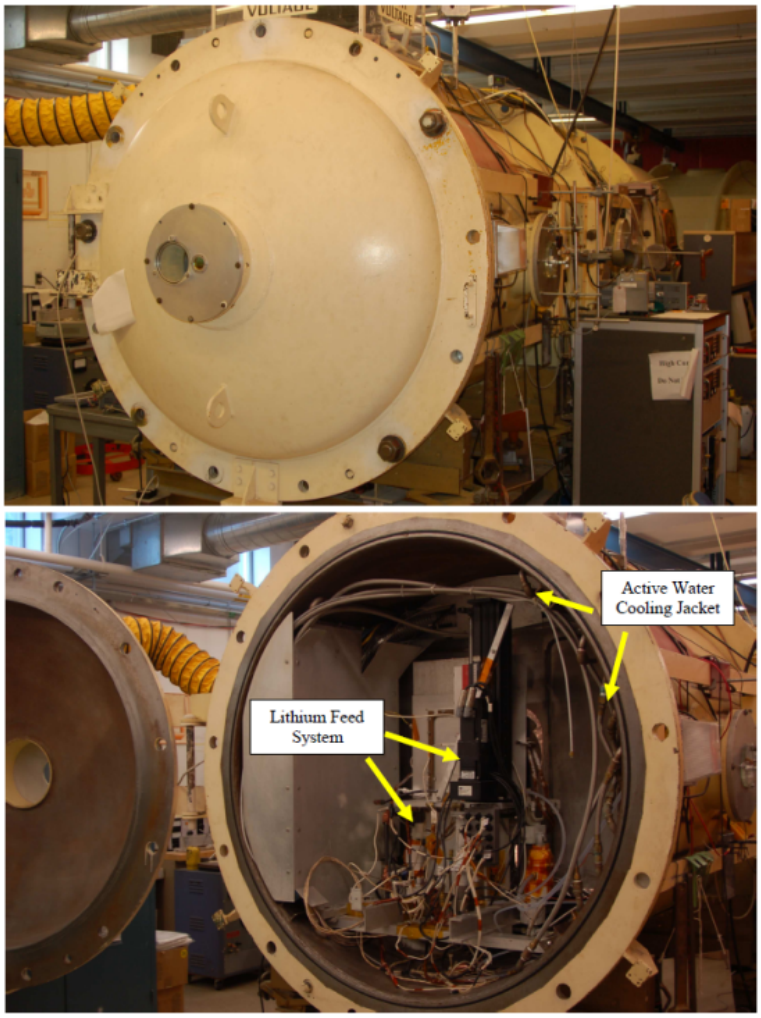

Figure 3.2: Front end of the Steady State Low Power Facility (SSLPF) with the main access door closed (top) and open (bottom).

3.3 The Lithium Lorentz Force Accelerator

The **Li**thium **L**orentz **F**orce **A**ccelerator (LiLFA) is a lithium-fed, steady-state thruster designed to operate at 30 kW. The LiLFA was built and initially tested at **M**oscow **A**viation **I**nstitute (MAI)[25, 28, 30, 32]. It was transferred to Princeton's EPPDyL in 1998. A schematic and a picture of the LiLFA are presented in Fig. 3.3.

The LiLFA consists of three main components that are electrically insulated from one another: the anode assembly, the cathode assembly and the solenoid (Fig. 3.4). The LiLFA consists of a conical anode made of tungsten with an upstream inner

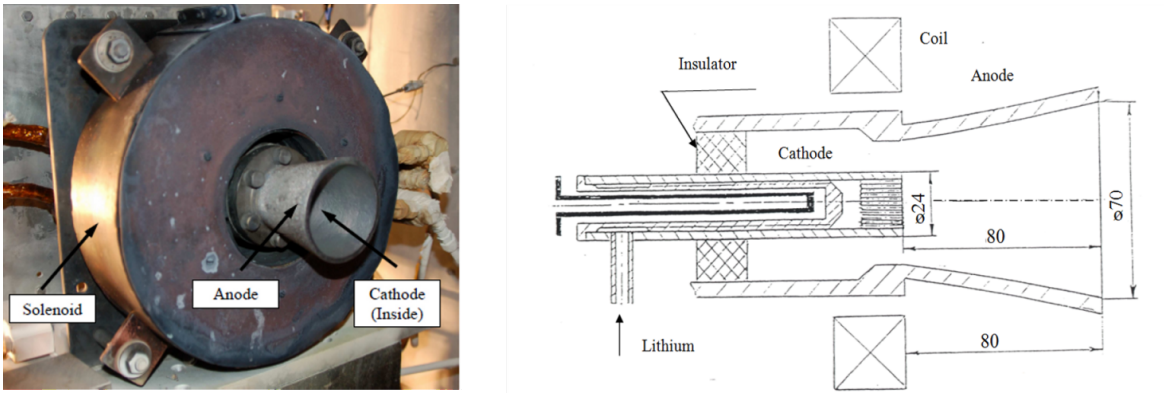

Figure 3.3: Left: Picture of the LiLFA Right: Cross-sectional view of the Lithium Lorentz Force Accelerator (all dimensions are in millimeters).

diameter of 45 mm and a downstream inner diameter of 70 mm. The cylindrical multi-channel hollow cathode (MCHC), also made of tungsten, has an inner diameter of 19.2 mm and a length of 215 mm (100 mm in the thruster cavity). The hollow tip contains 68 small tungsten rods, each 2 mm in diameter and 14 mm in length, recessed 6 mm from the tip.

The lithium is pumped in a liquid state by a dedicated feed system into the cathode through a 1/16″ inside diameter feed tube. Before thruster arc initiation, the cathode evaporates the incoming liquid lithium provided by the feed system, because of its high initial temperature (well over 1000°C), which is maintained by a graphite heater embedded inside. The cathode heater uses approximately 1.5 kW of power. The cathode and anode are each connected to a stainless steel plate. Four bolts attach the cathode plate, fixing the two assemblies relative to each other, the assemblies are separated from each other by a boron-nitride insulator for electrical insulation. The anode and cathode receive their power from a 30 kW Miller SRS 1000 high current welding power supply through a copper rod on each side of the thruster stand. These rods connect directly to the cathode and anode plates.

During operation the cathode reaches temperatures of well over 2000°C [47] while the anode reaches temperatures of up to 2000°C[30].

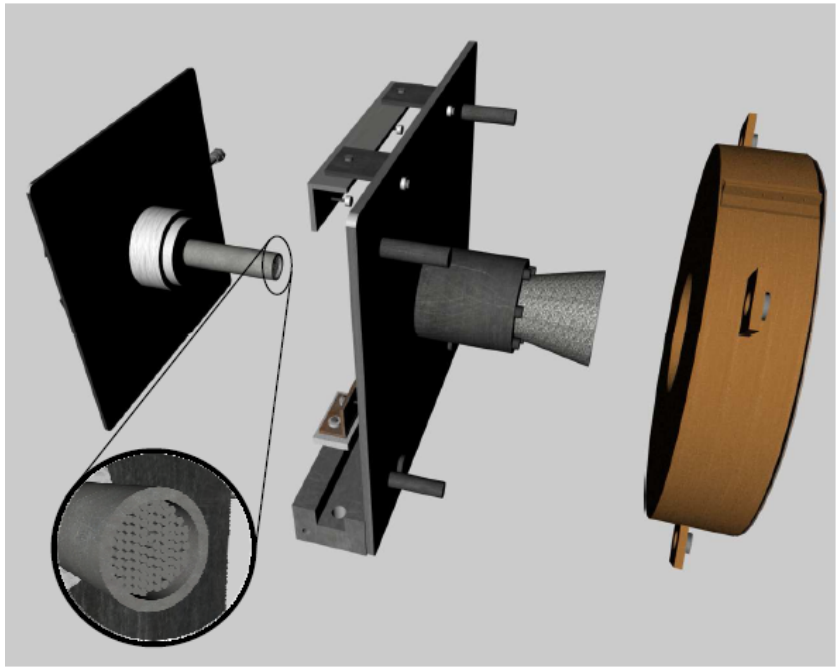

Figure 3.4: Exploded View of the LiLFA with a close-up on the cathode's multi-channel end.

3.4 The Solenoid

The applied magnetic field is generated by a water cooled solenoid (Figs. 3.3 and 3.4), which has a 280 mm outer diameter and 120 mm inner diameter. The solenoid is comprised of 56 turns of a copper tube 8 mm in diameter. A magnetic field of 0.08 T is generated at a current of 250 A. At this current the solenoid draws approximately 2.6 kW of power. The solenoid is powered by a Rapid Power Corporation high-current power supply capable of delivering a current of up to 650 ADC.

Prior to all experiments, the relation between current and applied magnetic field at the solenoid center was measured using a Hall magnetic probe. The graph shown in Fig. 3.5 is used to relate the current flowing in the solenoid to the applied magnetic field.

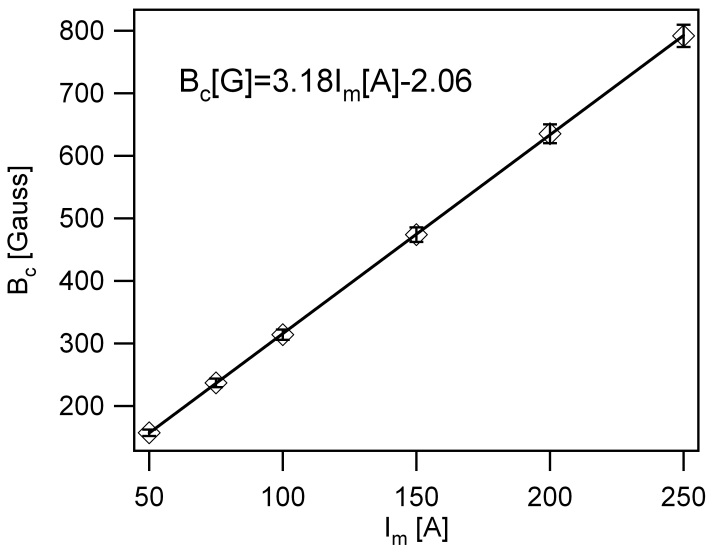

Figure 3.5: Applied magnetic field (in Gauss) measured at the solenoid center vs. solenoid current (in Amperes).

3.5 Lithium Evaporator (Cathode Heater)

The liquid lithium is evaporated inside the cathode by means of an internal heater, also called the *cathode heater*. The cathode heater is a 153 mm long circular graphite rod (8.1 mm in diameter) through which high current flows (Fig. 3.5). It has a longitudinal slit, along most of its length, that provides a path for current to flow up one side and down the other. Graphite is used for the heater because of its relatively high resistivity (7.84×10^{-6} Ω·m) compared to metals and its thermal properties under vacuum. The resulting resistance enables continuous conduction of over 100 A at a voltage of about 14 V. At this current the cathode heater reaches temperatures of well over 1000°C. It is attached to the cathode base by a set of six electrically insulated screws, thereby preventing any electrical connection between the cathode heater and the cathode. The heating is accomplished through radiation to the inner walls of a channel inside the cathode, since there is no electrical contact between the cathode heater and cathode.

The cathode heater at its normal operational point of 110 A and 14.2 V (1.56 kW)

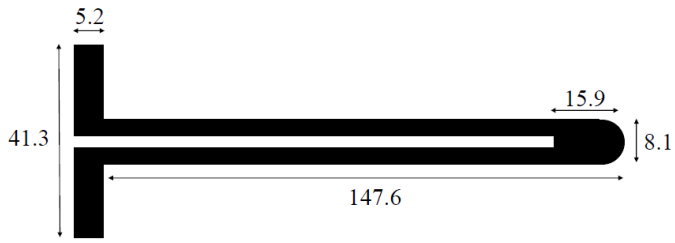

(a)

(b)

Figure 3.6: (a) Schematic and (b) picture of the cathode heater. All dimensions are in millimeters.

can heat the cathode to over 1000°C, thus supplying the required power for the heating and evaporation of liquid lithium.

3.6 Lithium Feed System

The feed system delivers liquid lithium into the thruster cathode at a controlled mass flow rate. It consists of a lithium reservoir, lithium container (cylinder), piston and piston drive motor, lithium freeze valve, cooling water loop, pipeline and argon injection line (Figs. 3.7 and 3.8).

The *reservoir* is a stainless steel container, 82 mm inside diameter and 165 mm in length. Around it two Watlow mineral-insulated band heaters, each capable of delivering up to 1.2 kW, are used to heat the reservoir above lithium's melting point of 183°C and melt the lithium contained in the reservoir. The reservoir's lid contains a gas inlet which is used to inject argon at a low flow rate in order to push the liquid lithium out of the reservoir through an outlet tube connected to its bottom. The

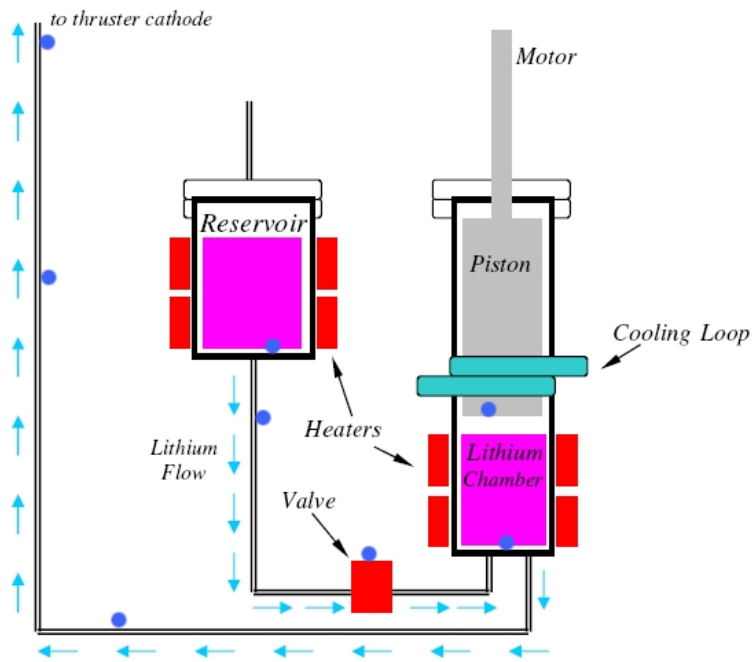

Figure 3.7: Schematic of the lithium feed system. The blue dots mark thermocouple positions

liquid lithium then flows through the heated pipeline, called the *reservoir line*, into a large cylindrical container called the *lithium chamber* or *cylinder*. The cylinder is a cylindrical stainless steel container, 48 mm inside diameter and 375 mm in length, which maintains the lithium in a liquid form using two Watlow mineral-insulated band heaters capable of delivering up to 1.5 kW each. The bottom half of the cylinder is used to contain liquid lithium, whereas the top half contains a stainless steel piston used to push the lithium out of the cylinder at a constant mass flow rate. The outside of the middle section of the cylinder is wrapped with a 1/4″ tube carrying 45 g/s of cooling fluid from the secondary closed-loop cooling system. In addition to compression rings on the end of the piston, the cooling loop maintains a local low temperature so that any liquid lithium leaking up through the gap between the piston rings and the inner walls of the cylinder solidifies, thus preventing further leaks.

After lithium is transferred from the reservoir to the cylinder, a small amount is frozen in the reservoir line by means of water cooling (at 45 g/s) of a copper cube,

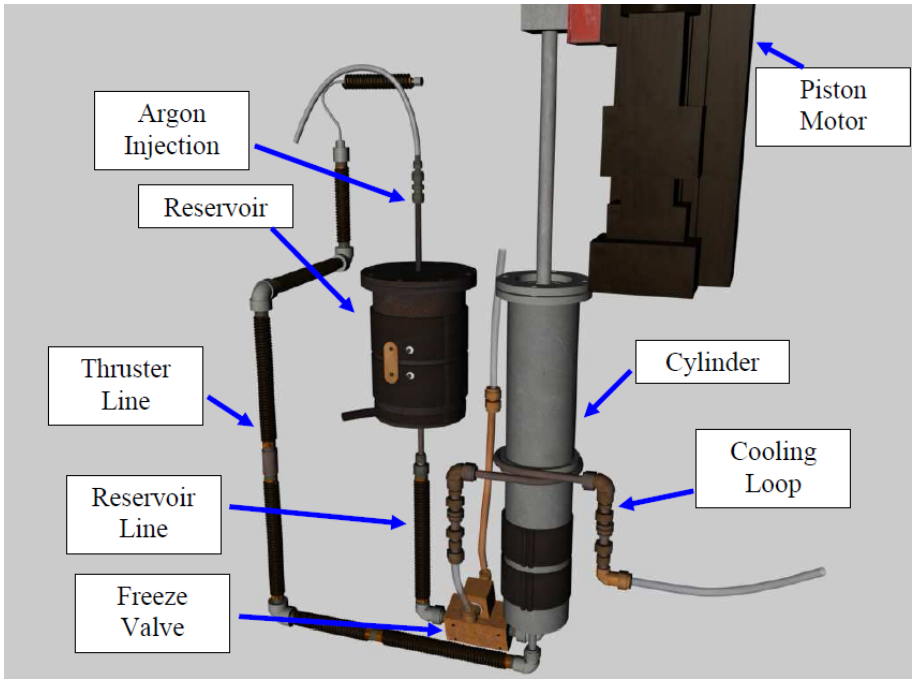

Figure 3.8: Illustration of the lithium feed system.

called the freeze valve, which is clamped around the reservoir line near the cylinder. This cube is actively heated during lithium transfer and actively cooled after transfer is complete. This cooling freezes the lithium in the reservoir line, preventing lithium flow back into the reservoir.

The piston is a cylinder, 46.3 mm in diameter and 205 mm in length, connected through a 3/8″ diameter 400 mm long shaft to a G & G Technical Company high force linear actuator. The actuator is capable of moving the piston at a rate of 0.0012-0.24 mm/s, which corresponds to lithium mass flow rates of 1-200 mg/s. The lithium is pushed out of the cylinder through a pipeline connected to the bottom of the cylinder, called the *thruster line*, and ultimately delivered to the cathode.
Both the reservoir line and the thruster line are constructed of 1/4″ stainless steel tubes, wrapped by a total of eight Watlow coiled heaters capable of delivering up to 500 W each, thereby maintaining the lithium in a liquid state.

The entire heating procedure takes about 6 hours to reach steady-state, during which the lithium is kept at a temperature of over 250°C except for in the freeze

valve. That valve stays below lithium's melting point both before and after liquid lithium has been transferred into the cylinder.

3.6.1 Lithium Control and Monitoring

All heaters in the feed system are powered by facility power of 120 VAC and controlled by a set of 4 Staco Model 3PN1010B auto-transformers (variacs) and are electrically insulated from facility power by two 1:1 isolation transformers. An additional rod-shaped heater delivers heating power directly to the freeze valve during the lithium transfer phase.

The piston actuator is controlled and monitored by a Pacific Scientific model PC800 servo drive module. The piston's position is also monitored by a linear voltage displacement transducer (LVDT) capable of measuring over 150 mm of piston displacement. Argon flow into the reservoir is controlled via a needle valve and monitored using a Setra model 280E pressure transducer. The input and output cooling water flow rates to the feed system are controlled via gate valves and monitored using two Malema flow sensors rotary flow meters.

The feed system temperature is monitored using eight ungrounded K-type thermocouples positioned at various locations along the feed system, as seen in Fig. 3.7. Tracking the thermocouple readings provides information regarding the lithium location in the feed system components and the temperature distribution, and helps guide the timing of actions leading to propellant injection into the cathode[48]. The thermocouple sheaths are in contact with the feed system, and are therefore at cathode potential thus posing a hazard when connected to the data acquisition system located outside of the tank. For this reason the thermocouples are galvanically insulated by a set of eight Omega thermocouple signal conditioners located on top of the vacuum chamber. In addition three T-type thermocouples measure the inlet and feed system cooling water outlet temperatures and outlet solenoid cooling water temperature.

All signals from the above sensors and diagnostics are received by a National Instruments data acquisition module, model 6034E, and recorded using LabView.

3.6.2 Power Requirements

The main components of the feed system and their power requirements are listed in table 3.1.

Component	*Power* [W]	*Voltage* [V]	*Current* [A]	*Melting & Transfer*	*Injection*
Reservoir Heaters	350	84	4.2	✓	*X*
Reservoir Line Heater	19.2	24	0.8	✓	*X*
Valve Heater	48	48	1	✓	*X*
Cylinder Heaters	720	120	4.8	✓	✓
Thruster Line Heaters	288	60	4.8	*X*	✓
Piston Motor	8.4	120	0.07	*X*	✓

Table 3.1: Power requirements of the components of the feed system

Each component, except for the cylinder heaters, is on or off during one of two phases. These phases are: (1) lithium melting and transfer and (2) lithium injection to cathode. The numbers presented in the table represent the input power to the feed system and are therefore subject to power losses through radiation and conduction, since not all input power is actually delivered to the lithium. It can be seen from the table that during thruster operation, when lithium is injected into the thruster, the total power to the feed system is about 1060 W, and is therefore significant to total system efficiency calculations.

3.6.3 Lithium Injection Procedure and Timeline

As mentioned earlier, it takes six hours from the beginning of the heating process until thruster ignition. This process can be divided into the following:

1. Lithium melting (3 hours)

2. Lithium transfer to cylinder (5 minutes)

3. Lithium injection through thruster line (2 hours)

4. Lithium injection into the thruster (1 hour)

At each of the stages mentioned above, the limiting factor is the heating time of the various components of the feed system, due to their high thermal inertia. In addition, not all heaters are on at the same time in order to minimize the operation time of each heater, which increases their lifetime. The feed system's operational chronology is shown in Fig. 3.9.

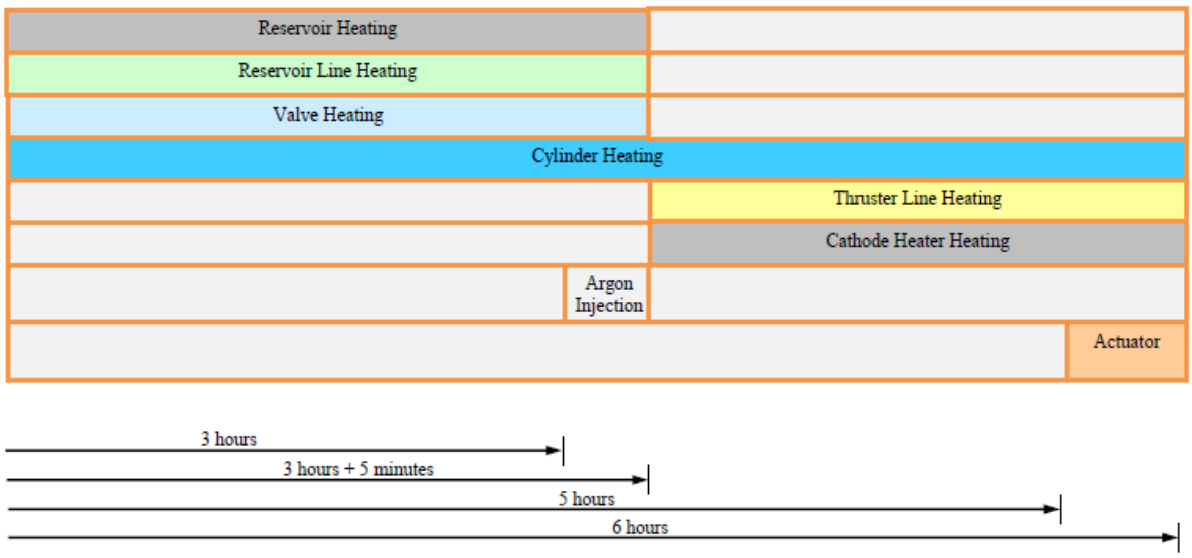

Figure 3.9: Feed system operation timeline from the beginning of the heating process to thruster ignition

3.7 Lithium Loading Apparatus

Prior to the feed system heating process the lithium is loaded into the reservoir at room temperature as a solid. Since lithium is highly reactive it cannot be exposed to ambient air and must be transferred from its packaging to the reservoir under an inert gas environment. This procedure is performed in a glove box (Fig. 3.10) in an

argon atmosphere at positive atmospheric pressure, while the transfer to the vacuum chamber is done with the reservoir, which is hermetically sealed.

The lithium loading procedure is done as follows. The packed lithium ingot and the

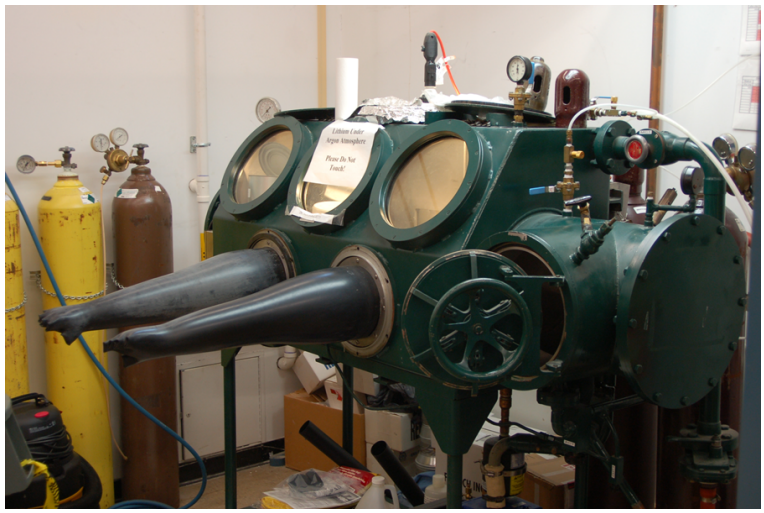

Figure 3.10: The glove box where lithium is loaded into the reservoir

reservoir are placed in the glove box, which is then evacuated and back-filled with argon. The lithium ingot is placed in the reservoir, the cover is placed on, and the reservoir's inlet and outlet tubes capped. The reservoir is then quickly taken out of the glove box to the vacuum chamber, and placed in its position in the feed system. The top cap is removed and the argon injection line is connected while fresh argon is flowing to keep the reservoir from being contaminated with air. The bottom reservoir cap is then removed and the reservoir is connected to the reservoir line. The vacuum chamber is then closed and evacuated while a continuous flow of argon is injected through the argon injection line until a significant low pressure of under 100 mTorr is reached.

3.8 Optical Access

Since lithium condenses on surfaces at temperatures below its boiling point (1342°C), it can obscure any optical path into the vacuum chamber by covering the windows.

In order to confront this problem we used the *continuous film* method[47] in which a rolling mylar film condensed lithium vapor and prevented it from reaching the window. Mylar was found to maintain structural integrity when exposed to small quantities of lithium while evenly transmitting light in the visible wavelengths. The continuous film method was implemented using a port-cover-mounted mechanism consisting of a 15 cm wide supply spool of mylar film and a take-up spool as shown in Fig. 3.11, taken from Ref. [47]. The take-up spool is connected to and driven by a DC motor controlled by a variable-voltage power supply. The film roll rate is adjusted according to visual inspection of lithium deposition on the mylar film and was in the range 0.5-5 mm/s. All optical measurements were taken only after a visual verification of a clear optical path to the thruster and plasma plume was performed.

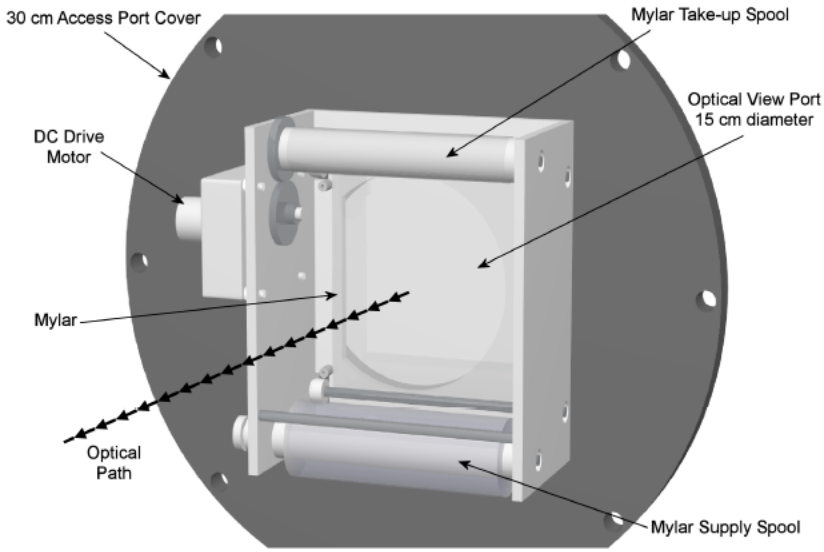

Figure 3.11: The continuous film mechanism for a clear optical path into the vacuum chamber

3.9 Lithium Handling and Safety

Lithium, due to its high reactivity with air and water, poses possible hazards when handled prior to, during and after LiLFA operation. Lithium reaction with air pro-

duces lithium oxide and lithium nitride as shown in Eqs. 3.1-3.3

$$4Li + O_2 \rightarrow 2Li_2O \tag{3.1}$$

$$2Li + O_2 \rightarrow Li_2O_2 \tag{3.2}$$

$$6Li + N_2 \rightarrow 2Li_3N_2. \tag{3.3}$$

Lithium reaction with water produces lithium hydroxide and releases hydrogen and heat as shown in Eq. 3.4.

$$2Li + 2H_2O \rightarrow 2LiOH + H_2 + 1016\ kJ/mol \tag{3.4}$$

During the loading process, lithium might react with air creating the lithium-nitride compound, which is flammable and reacts violently with water. During thruster operation, lithium condenses on the inner surfaces of the vacuum chamber and needs to be neutralized and removed after the experiment. Lithium must be removed from the individual components of the feed system prior to future LiLFA operations. All of these cases pose possible short-and long-term hazards to both the human operators and facility, and need to be carefully addressed. In order to mitigate these hazards, suitable detectors, safety gear and handling and cleaning procedures are used:

1. When coming in direct contact with lithium or lithium compounds, the human operator must wear nitrile or nomex gloves.

2. When surrounded by lithium compounds, such as during vacuum chamber entry after LiLFA operation, the human operator must wear tyvex suits and be equipped with fully self-contained breathing apparatus (SCBA) to prevent lithium compound inhalation.

3. After LiLFA operation is complete, the vacuum chamber is kept under ultimate

vacuum approximately (2×10^{-5} Torr) until all temperatures are below 50°C. Then it is neutralized by injecting small quantities of water into the vacuum chamber. The hydrogen released from the chemical reaction is evacuated by the vacuum system, which is purged with pure nitrogen.

4. During LiLFA operation, the vacuum chamber inner walls are covered with 0.002″ thick aluminum foil so that lithium condenses and solidifies on it. The aluminum foil is manually removed after the vacuum chamber is opened and disposed of by the university's hazardous-waste disposal personnel.

5. After the vacuum chamber is opened, the various components of the lithium feed system are removed and placed in cold water for neutralization. The removal of the feed system and vacuum chamber cleanup is done by the human operators that are wearing full tyvex suits and using air respirators with a full SCBA apparatus as shown in Fig. 3.12. The neutralizing water temperature is monitored, while a vent duct conducts the released hydrogen to the outside. After all neutralization is complete, the contaminated water is pumped into a 55-gallon drum and disposed of by the University's hazardous waste disposal personnel.

6. Hydrogen detectors located at various locations in the facility are set to alarm when the hydrogen concentration is above 30% of its lower explosive limit, which is a 4% hydrogen concentration.

All human operators working in the SSLPF are trained in all of the above procedures on a yearly basis and are required to rigorously follow them. This ensures the safety of the human operators and the facility, and prevents injuries and the infliction of damage.

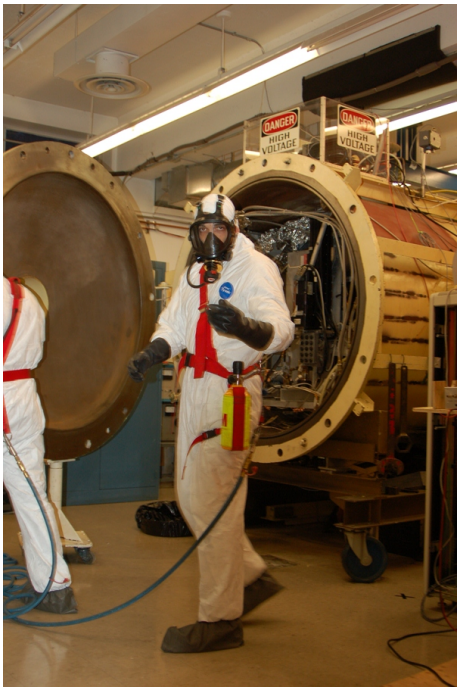

Figure 3.12: Human operators wearing full tyvex suits and using respirators while removing the feed system

3.10 Power Requirements of Supporting Systems

Several of the subsystems presented in this chapter function during LiLFA operation and require power in addition to the power to the thruster. These power requirements are summarized in Table 3.2

Supporting Subsystem	*Power Requirement During Thruster Operation [kW]*
Cathode Heater	1.5
Solenoid	up to 2.6
Propellant Feed System	1.1
Total	**up to 5.2**

Table 3.2: Power requirements of supporting subsystems during thruster operation

It can be seen from the table that the overall power required for the supporting subsystems at the Princeton facility can exceed 5 kW, which is a considerable fraction of the thruster power (30 kW). However, since no effort was made to optimize the

power consumption of the solenoid and lithium feed system, and since that consumption would depend on design considerations that are largely extraneous to the plasma dynamics of the discharge inside the thruster, the required power to operate these supporting subsystems was not included in the calculation of the thrust efficiency reported in this thesis. Of course, in this type of system these additional power consumption requirements will have an effect on the overall system efficiency and must be taken into account in any final design.

Chapter 4

Diagnostics

This chapter describes in detail the diagnostics used to measure the LiLFA plasma and thruster properties during operation. These include the data acquisition system, voltage-current measurements, emissive Langmuir probe, emission spectroscopy and optical pyrometry.

4.1 General Layout

The general diagnostics layout is illustrated in Fig. 4.1. The diagnostics are located both inside and outside the vacuum chamber. The data acquisition system is located next to the vacuum chamber. The Langmuir emissive probe is located inside the chamber and extends into the thruster. The spectrometer and optical pyrometer are located outside of the vacuum chamber next to the glass window, with a line of sight to the plasma plume and thruster anode respectively. Each diagnostic was operated and data collected by one operator.

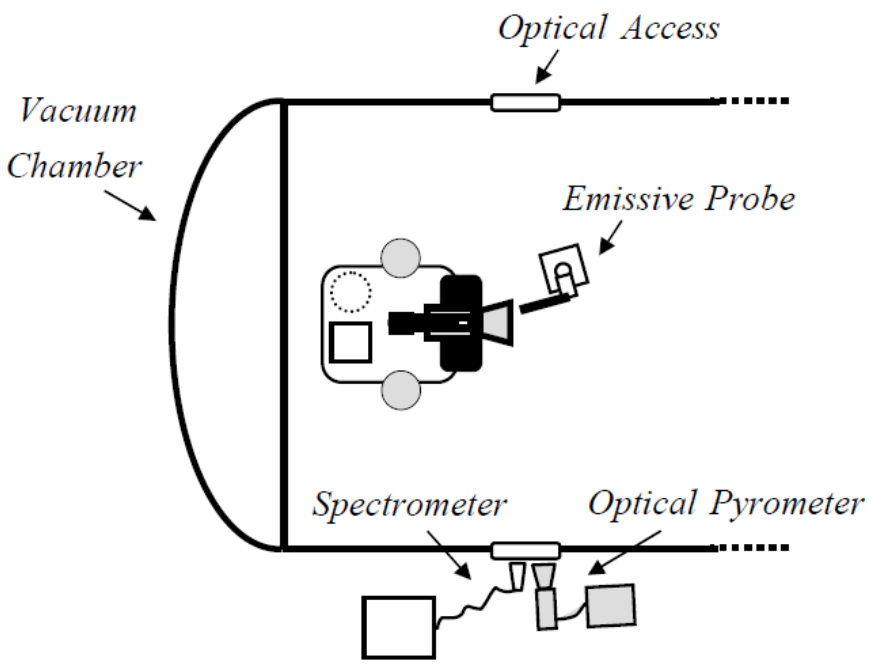

Figure 4.1: General layout of the diagnostics.

4.2 Data Acquisition System

All output signals from the feed system's control and monitoring devices, as well as facility diagnostics, cathode-heater current sensor, solenoid voltage and current sensors, thruster current sensor and thruster voltage sensor, are directly obtained by a National Instruments analog to digital data acquisition (DAQ) module model 6034E. All information from the DAQ was recorded by LabView software on the *control and diagnostic computer* (G4-PowerMac). A full control and diagnostic "VI" was constructed in LabViewiew to record and process all the incoming data at a rate of once per second. All information was presented to the computer operator in real time and saved to an Excel file. Using LabView the computer operator also controlled the piston motor, thereby controlling the propellant mass flow rate to the thruster. Data obtained from the emissive probe, optical pyrometer and spectrometer were recorded separately, either manually or using additional computers.

4.3 Voltage Current Measurements

Total current to the thruster was measured by an FWBell closed-loop Hall effect sensor, model QB-1687, located on the anode current line outside and on top of the vacuum chamber. The sensor's output was obtained directly through the data acquisition system and processed by the control and diagnostic computer.

Total voltage was measured by means of 25:1 voltage divider between the cathode and anode lines outside and on top of the vacuum chamber. The 25:1 ratio was chosen for compatibility with the data acquisition system's input voltage limit (5 V). The measured voltage was obtained directly by the high impedance data acquisition system and processed by the control and diagnostic computer.

4.4 Emissive Langmuir Probe

A stationary, electrically isolated, floating, emissive Langmuir probe, 1 mm in diameter and 2 mm in exposed length, was used to measure anode sheath voltage fall by positioning the probe about 1 mm away from the anode wall at the anode face (Fig. 4.2).

All the design details of the emissive probe and required theoretical background can

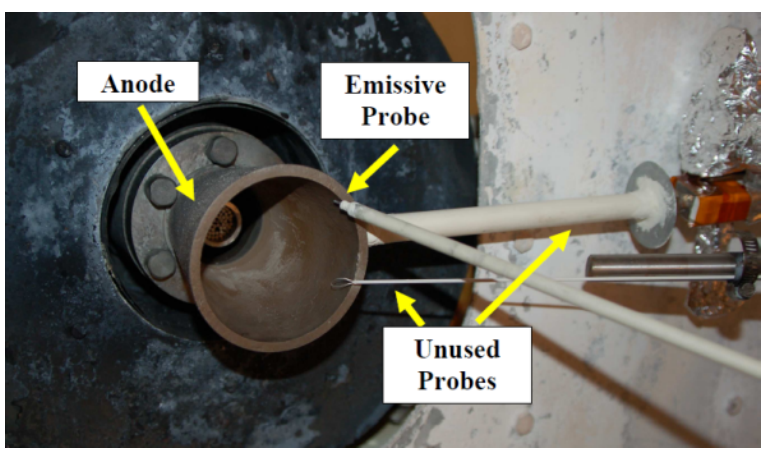

Figure 4.2: Picture of the Langmuir emissive probe. The two other probes seen in the picture were unused.

be found in appendix A.

The probe tip is made of tungsten wire (1 mm in diameter) encapsulated in a cylindrical ceramic sheath to prevent electron and ion collection outside of the intended collecting region. It is held in place by a steel stand about 10″ away from the anode so to prevent any interference to potential measurements made by the probe. The probe is not biased and is electrically floating at the potential in the near anode region. It is exposed to temperatures well over 1600 K, which is required for emitted charge saturation from the effects of plasma enthalpy amd direct radiation from the electrodes. This ensures a known potential difference of $\Delta_{CL} = 1.23\frac{k_B T_e}{e}$ Volts between the floating and plasma potentials and enables the estimation of the plasma potential relative to anode potential that is the anode sheath voltage fall (see appendix A). The electron temperature in the near anode region can be estimated to be 2 eV, according to Ref. [25].

Anode sheath voltage fall measurements were obtained by extending two high-temperature insulated wires from the probe and anode separately, and measuring the voltage between them. All floating potential probe measurements were taken relative to the anode. The measured voltage was then processed by a circuit designed specifically to safely handle and obtain the voltage readings. All data was recorded in real time by the operator and post-processed after the experiment to implement corrections.

During thruster operation the probe was able to withstand the high heat fluxes associated with the thruster as well as the highly corrosive hot lithium environment. After each experiment the emissive probe was visually and electrically examined for structural integrity.

4.5 Optical Pyrometry

A Leeds and Northrup disappearing-filament optical pyrometer, model 8622-C, was used to measure the anode temperature during LiLFA operation. The pyrometer contains a tungsten line filament which is current-heated until it matches, at a wavelength of 650 nm, the brightness of the object at which the pyrometer is pointed. The matching is done visually by the operator by raising or lowering the current to the filament thereby changing its emitted intensity. The pyrometer is pre-calibrated such that the heating current in the filament corresponds to a gray-body brightness, with a known emissivity, at 650 nm.

The pyrometer is positioned outside of the vacuum chamber and next to the side glass window with a direct line of sight to the anode, as shown in Fig. 4.3.

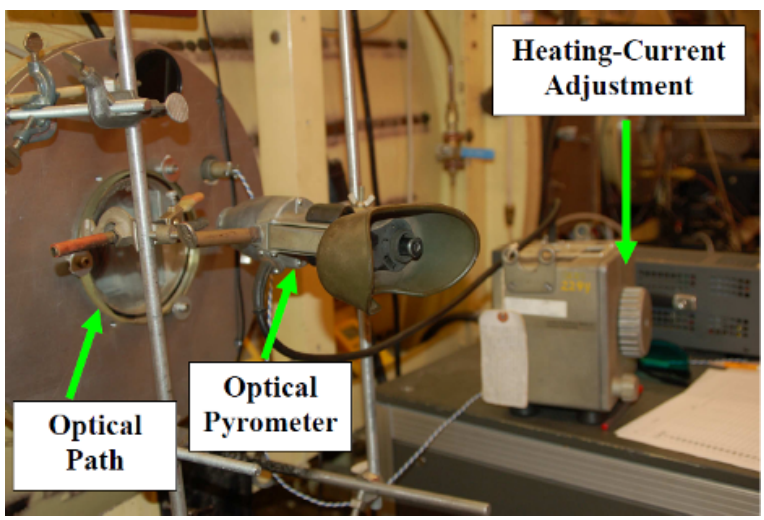

Figure 4.3: The optical pyrometer.

The temperature measured by the pyrometer corresponds to the brightness temperature and does not take into account the fact that the anode is an imperfect blackbody with a known emissivity. The gray body correction for the measured temperature is described in detail in appendix C. The emissivity for the anode was taken as the emissivity of tungsten at a temperature of 2000 K, which is $\epsilon = 0.442$ [49]. Another correction is required for the glass window transmissivity, which we

take to be $\tau = 0.8$ (see appendix D). Therefore the effective emissivity coefficient is $\epsilon_{eff} = 0.442 \times 0.8 = 0.354$ and this value is used in the calculation of the gray-body-corrected temperature.

4.6 Emission Spectroscopy

A Thor Labs spectrometer, model SP-1, with wavelength range of $257 - 816$ nm, was used to estimate the electron temperature (T_e) in the thruster plume about 2 mm from the anode face. The collimator connected to the spectrometer was positioned outside of the vacuum chamber and next to the glass window with a direct line of sight to the thruster plume, as shown in Fig. 4.4.

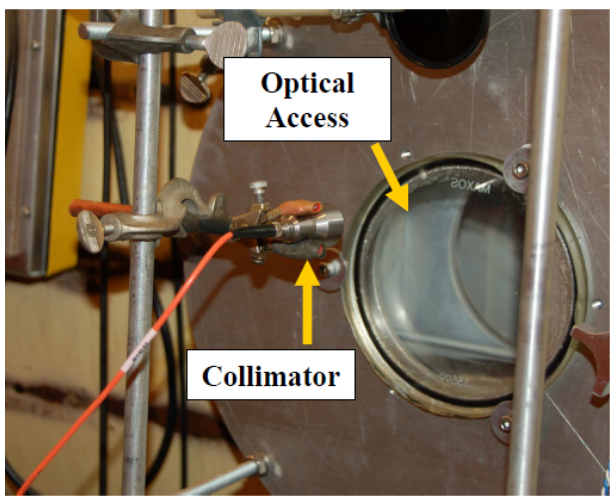

Figure 4.4: Spectrometer collimator position, with a direct line of sight to the thruster plume.

The data measured by the spectrometer was the centerline-averaged emitted intensity in the wavelength range. Therefore, the measured electron temperature is not a single-point measurement, but the electron temperature correlated to the average spectral intensity along a line that passes through the centerline of the thruster plume 2 mm from the anode face, as shown in Fig. 4.4. This gives an estimation of the average electron temperature in the thruster plume.

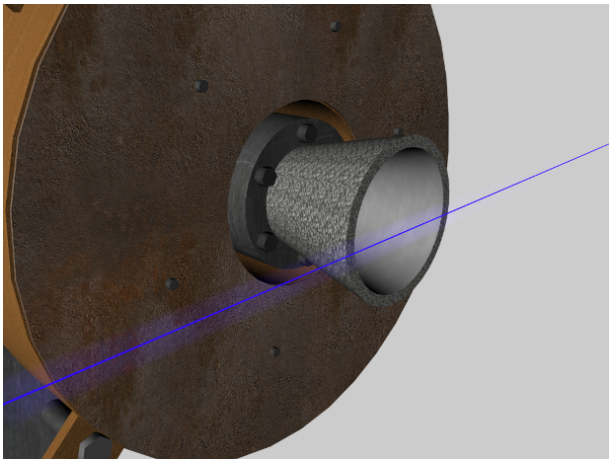

Figure 4.5: Spectrometer collimator line of sight through the thruster plume.

The electron temperature can be estimated with knowledge of the relative intensity at different wavelengths, as elaborated upon in appendix D. The maximum intensity-ratio resolution of the Thor Labs spectrometer is about 500:1. Since for some electron temperature measurements, the required intensity ratio resolution is over 5000:1 we used a 64× neutral density filter for our measurements. Each measurement was made with and without the neutral density filter, thereby giving a wider dynamic range of measured intensity. The emitted wavelengths considered in our analysis corresponded to lithium emission lines at 460, 610, 670 and 813 nm.

The measured intensity for the different wavelengths was obtained and recorded by a computer with Thor Labs software. All the data was post-processed after the experiment to implement known correction factors.

Chapter 5

Experimental Results

In this chapter we present the experimental data obtained during LiLFA operation for a wide range of the three operational parameters, J, B and $\dot{m}$. These paramount relationships were not completely characterized in past research and are imperative for the understanding of the different power mechanisms in AF-MPDTs. The main goal of these experimental measurements was to characterize the total thruster voltage, anode sheath voltage fall, electron temperature at the anode exit plane and anode temperature. These experimental data are required to determine the different scaling relations of total thruster power and its power dissipation components with the operational parameters and aid in the formulation of anode sheath voltage fall and total voltage models presented in chapters 6 and 7. In particular, anode sheath voltage fall measurements and anode temperature measurements are used to calculate the anode power dissipation component, electron temperature measurements at the anode exit plane are used to calculate the electron heating power component and total thruster voltage measurements are used to calculate the total power to the thruster. All measurements are eventually used along with the efficiency model presented in chapter 7.

5.1 Total Thruster Voltage Measurements

In chapter 1 it was explained that power distribution analysis in MPDTs can be conducted by examining the different voltage components of the thruster. It was also pointed out that the total voltage, V_{tot}, to the MPDT is representative of the total thruster power as V_{tot} is calculated by dividing the total power by the current, J. Therefore measuring the V_{tot}-J characteristics of the AF-MPDT is required for the estimation of total thruster power and the characterization of thrust efficiency.

Total thruster voltage was measured across the anode and cathode terminals at the connections to the vacuum chamber as described in section 4.3. In order to determine the dependence of total thruster voltage on thruster current, J, applied magnetic field, B, and mass flow rate, $\dot{m}$, measurements were obtained at current values between approximately 100 A and 1000 A, applied field values between 0 T and 0.1 T and mass flow rate values of 5 mg/s, 8 mg/s and 20 mg/s. A total of 120 different cases with and without applied magnetic field were studied. This variety of operational parameters enables a thorough characterization of the total thruster voltage. At each point data were obtained after voltage reached steady state, which usually took about 2 min. All magnetic field values were measured at the center of the solenoid.

Error estimations were made at each measurement for each individual voltage reading according to the estimated voltage fluctuations and were added to the standard deviation at each operational condition. The voltage-current characteristics are presented in Figs. 5.1-5.3.

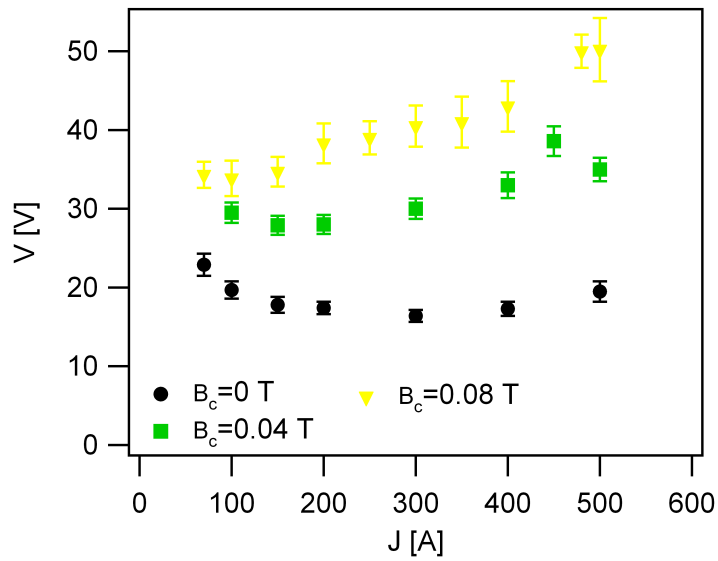

Figure 5.1: Total thruster voltage vs. current for different applied magnetic field values at $\dot{m}$=5 mg/s.

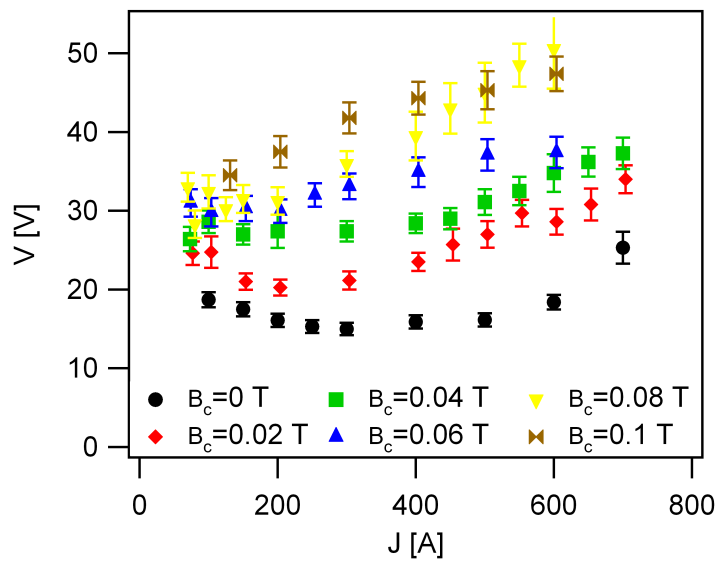

Figure 5.2: Total thruster voltage vs. current for different applied magnetic field values at $\dot{m}$=8 mg/s.

5.2 Observations and Discussion on Total Thruster Voltage Measurements

The voltage-current characteristics obtained for various applied magnetic field and mass flow rate values are presented in Figs. 5.1-5.3.

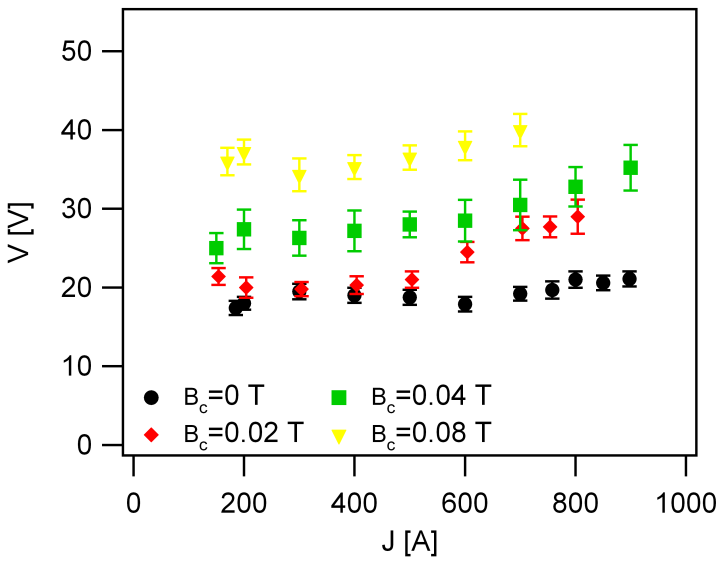

Figure 5.3: Total thruster voltage vs. current for different applied magnetic field values at $\dot{m}$=20 mg/s.

In Figs. 5.1-5.3 error is due to small fluctuations in the measured voltage. Although the arc was stable during thruster operation, small fluctuations on the order of 1 V were observed in most cases. In addition, we observed that the magnitude of voltage fluctuations was larger during operation at higher current values.

The observations from Figs. 5.1-5.3 are as following:

- **Dependence on applied magnetic field.** It can be observed from the figures that for all cases presented the voltage increases with increasing magnetic field. In some cases the voltage increases by a factor of almost 3 between two different applied-field values at a constant current and mass flow rate. This increase implies that the addition of an applied field to MPDT increases the total thruster power required. This power increase might come from increased thrust or other increased power dissipation components and will be thoroughly investigated in chapter 7.

- **V-J sensitivity with mass flow rate.** The increase of total voltage with applied field, at constant current, is higher for low mass flow rate values, i.e.

the lower the mass flow rate the greater the increase in total voltage with the applied field. To demonstrate, observe that the voltage-current curves at $\dot{m} =$ 20 mg/s are flatter than at $\dot{m} = 5$ mg/s. It can therefore be concluded that the total voltage is more sensitive to changes in current and applied magnetic field at low mass flow rate values. This sensitivity with mass flow rate implies a mathematical scaling relation of the form $V_{tot} \propto J^m/\dot{m}^n$ where m and n are positive numbers.

- **Low current regime trends.** It can also be observed that for most cases presented, the total voltage decreases with increasing current at current values below 400 A. This phenomenon resembles the voltage-current characteristics exhibited in *arcjet* thrusters where the current to mass flow rate ratio is lower than in MPDTs. Similarly to arcjets, in the low current regime propellant conductivity increases with increasing current, thus lowering the voltage between the electrodes[50]. We can likely assume that in both arcjets and MPDTs at low current values the voltage decreases with increasing current for this reason.

- **Dependence on thruster current.** At current values higher than 400 A the total voltage tends to increase with increasing current as also exhibited in self-field MPDTs[7, 33, 51, 52]. Therefore each curve has a minimum point associated with it. Moreover, the minimum point moves to lower current values with an increasing applied field while moving to higher current values with increasing mass flow rate. The reasons for these phenomena will be analyzed and discussed in chapter 7.

5.3 Experimental Repeatability Relative to MAI Facility

It is necessary to justify the usage of different experimental results obtained at MAI in our models by validating experimental repeatability between the Princeton facility and MAI's facility. After validation is verified several experimental results obtained at MAI will be used for the formulation of the anode sheath voltage fall and efficiency models presented in chapters 6 and 7. To verify similar operating conditions in both the MAI and Princeton facilities we present in Table 5.1 a comparison between voltage data obtained in both facilities at different current, applied-field and mass flow rate values.

$\dot{m}$ **[mg/s]**	B_c **[T]**	**J [A]**	**voltage [V] (MAI)**	**voltage [V] (Princeton)**	**Difference**
8	0.056	400	29.5	33±2	11.9%
8	0.056	500	33	34±2	3%
8	0.056	600	35	36±2.5	2.9%
8	0.056	700	39	39±2.5	0%
8	0.112	400	42	44±3	4.8%
8	0.112	500	46	47±3	2.2%
20	0.1	500	37.5	40±2	6.7%

Table 5.1: Comparison between voltage measurements taken at MAI and Princeton facilities

It can be seen from the table that MAI's voltage measurements are within 10% of the expected range of the data obtained in this study except for the first case presented. The 11.9% difference in the first case is due to a measurement taken early during a process of an experiment before a thermal steady state operation was established. The proximaty of the measured data in this study to the data obtained in MAI verifies operating repeatability between the two facilities. In addition, vacuum chamber ambient pressure was similar in both facilities and under 1 milliTorr.

5.4 Anode Sheath Voltage Fall Measurements

In chapters 1 and 2 it was explained that the main power dissipation mechanism in MPDTs is the anode sheath voltage fall, V_a. Therefore understanding the physics behind the anode sheath voltage fall and its scaling with the thruster's operational parameters is of great importance.

Measurements of V_a under varying operational conditions are needed to gain physical insight on the anode sheath voltage fall in AF-MPDTs. An emissive floating langmuir probe, described in section 4.4, was used to measure the floating potential relative to anode potential in the near anode region, the anode sheath voltage. The plasma potential was calculated from this measured voltage following the technique described in appendix A. This voltage was measured at current values between approximately 100 A and 800 A, applied field values between 0 T and 0.08 T and mass flow rate values of 5 mg/s, 8 mg/s and 20 mg/s, to determine the dependence of anode sheath voltage on thruster current, J. A total of 53 different cases with and without an applied magnetic field were studied. This variety of operational parameters enables a thorough characterization of the anode sheath voltage fall. At each experimental condition data were obtained after the langmuir probe voltage reached steady state, which usually took about 4 minutes. All magnetic field values were measured at the center of the solenoid.

Error estimations were made at each measurement for each individual anode voltage fall value according to the estimated voltage fluctuations observed at each reading.

The anode sheath voltage fall data are presented in Figs. 5.4-5.6.

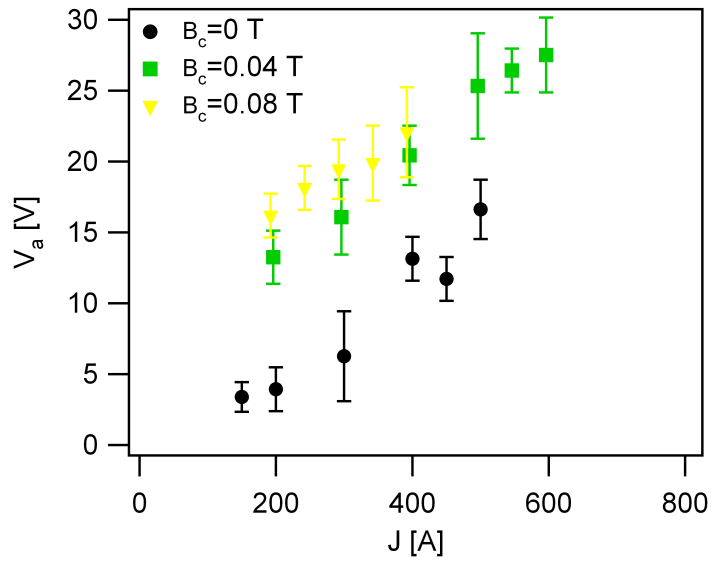

Figure 5.4: Anode sheath voltage fall vs. current for different applied magnetic field values at $\dot{m}$=5 mg/s.

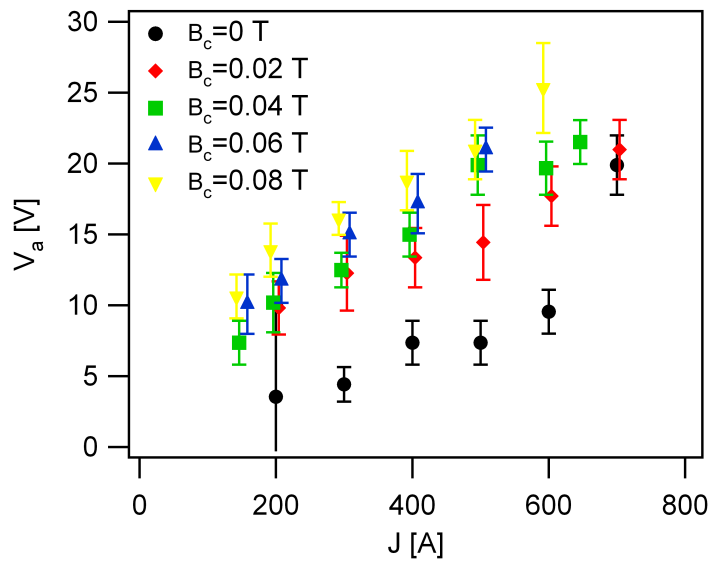

Figure 5.5: Anode sheath voltage fall vs. current for different applied magnetic field values at $\dot{m}$=8 mg/s.

5.5 Observations and Discussion on Anode Sheath Voltage Fall Measurements

The observations from Figs. 5.4-5.6 are summarized as follows:

- **Dependence on thruster current.** It can be observed from the figures that

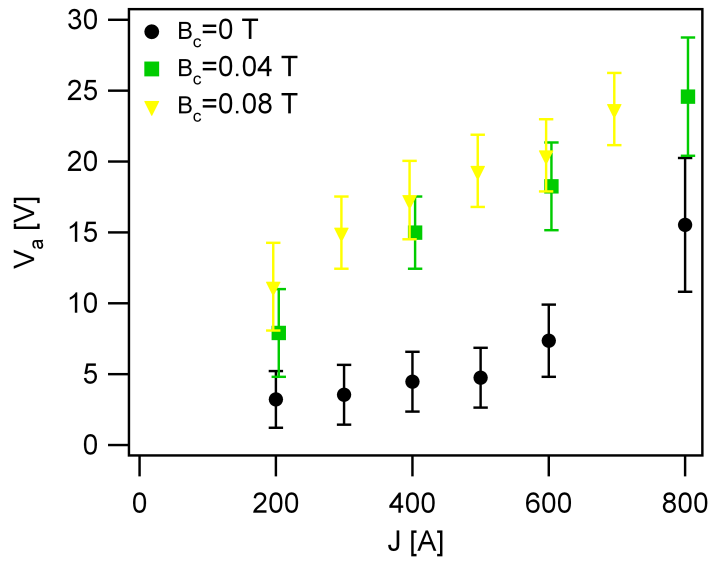

Figure 5.6: Anode sheath voltage fall vs. current for different applied magnetic field values at $\dot{m}$=20 mg/s.

for all mass flow rate and applied magnetic field values the anode fall increases approximately linearly with current. The rate of this increase seems to be approximately the same for all applied filed values at $\dot{m}$=5 mg/s while it increases with applied field at $\dot{m}$=8 mg/s and $\dot{m}$=20 mg/s. This dependence of anode fall on current was previously observed in MPDTs[22, 45] and even in AF-MPDTs by Myers[23]. The increase of anode fall with current seems to be somewhat non-linear and rapidly increasing for the non-applied field cases at all mass flow rate values. Moreover, this phenomenon occurs at lower current values at low mass flow rate operation. This trend resembles trends observed in MPDTs caused by the "onset phenomenon", which is caused by a lack of charge carriers in the near-anode region. This phenomenon is usually manifested at high current or low mass flow rate values and causes a fast anode erosion along with fluctuating thruster voltage[21, 53]. We assume that the same phenomenon occurs in our anode fall measurements, however, it is observed only during non-applied field operation. Since onset was not previously investigated in AF-MPDTs it remains unknown whether the addition of applied magnetic field ameliorates or

hastens onset in AF-MPDTs. From the results presented in Figs. 5.4-5.6 we might assume that applied field addition to MPDTs postpones onset to higher current values. It is not the scope of this thesis to investigate this phenomenon and we leave this question open to future researchers.

- **Dependence on applied magnetic field.** It is observed from Figs. 5.4-5.6 that anode sheath voltage fall increases with increasing applied magnetic field for all mass flow rate values. This phenomenon was also observed in previous studies on AF-MPDTs by Myers and Gallimore[23, 24] who observed a somewhat linear increase of anode fall with applied magnetic field. In our measurements a similar trend is observed at $\dot{m}$=8 mg/sec at applied field values higher than B=0.02 T. However, at $\dot{m}$=5 mg/sec and $\dot{m}$=20 mg/sec a large voltage fall increase is observed when increasing the applied field from 0 T to 0.04 T and an additional smaller increase from 0.04 T to 0.08 T.

- **Dependence on mass flow rate.** It is observed that the anode sheath voltage fall increases with decreasing mass flow rate. This phenomenon was also observed in AF-MPDTs by Myers yet the scaling relation between V_a and $\dot{m}$ was not determined due to lack of data at a variety of mass flow rate values.

5.6 Electron Temperature Measurements

The goal of electron temperature, T_e, measurements at the anode exit plane was to estimate the electron heat sink component in a thruster efficiency model. Emission intensity was measured using an SP1 Thor Labs spectrometer, described in section 4.6, and converted to electron temperature following the technique described in appendix D.

Emission intensity values were measured at current values between 150 A and 800 A, applied magnetic field values between 0 T and 0.1 T and mass flow rate

values between 8mg/s and 20mg/s. This variety of operational parameters enables a thorough characterization of the electron temperature at the anode exit plane as a function of operational parameters.

Emission intensity was insufficient at a mass flow rate of 5 mg/s to produce reliable data at 460 nm and 813 nm. Error estimations were made at each measurement for each individual emission line and were added to the error of the least mean square fit in Fig. D.1 in appendix D. These total error estimates were then used to evaluate the error in the slope of the line shown in Fig. D.1, which corresponds to the error in the electron temperature, T_e.

5.7 Observations and Discussion on Electron Temperature Measurements

The observations from Figs. 5.7-5.9 are as following:

- **Constant T_e value.** The electron temperature measurements presented in Figs. 5.7-5.9 indicate that the electron temperature is constant over a wide operational parameter space. This is a common phenomenon in MPDTs and was observed in past research efforts where T_e was measured to be constant for a variety of thruster current and applied magnetic field values[34, 37, 54]. In addition, Choueiri and Okuda[19] suggested that ionization in MPDTs at different operational conditions can originate from a superthermal tail in the velocity distribution while the bulk plasma stays at relatively lower electron temperatures on the order of 1 eV. This implies that the required ionization in MPDTs can occur at a constant bulk plasma temperature regardless of the operational conditions. Choueiri and Okuda then verified this ionization model by calculating the characteristic dimension of ionization front in MPDT and compared it to ionization length data taken by Randolph[55].

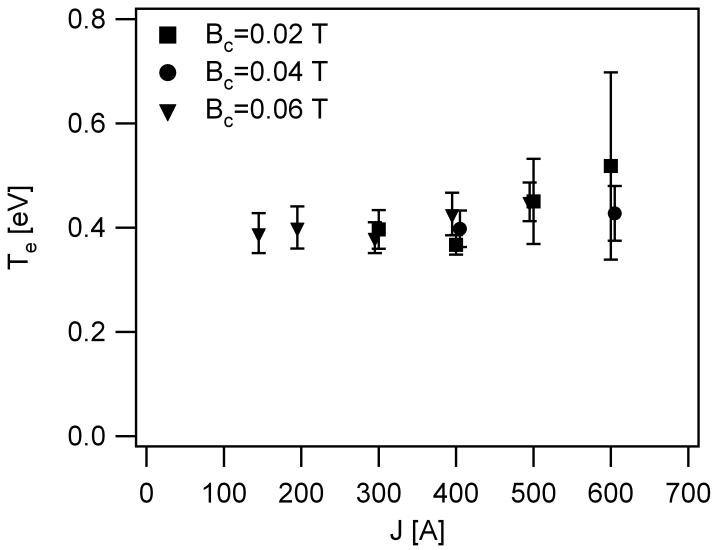

Figure 5.7: Electron Temperature, T_e, vs. thruster current, J, at the anode exit plane for different applied magnetic field values at $\dot{m}$=8 mg/s

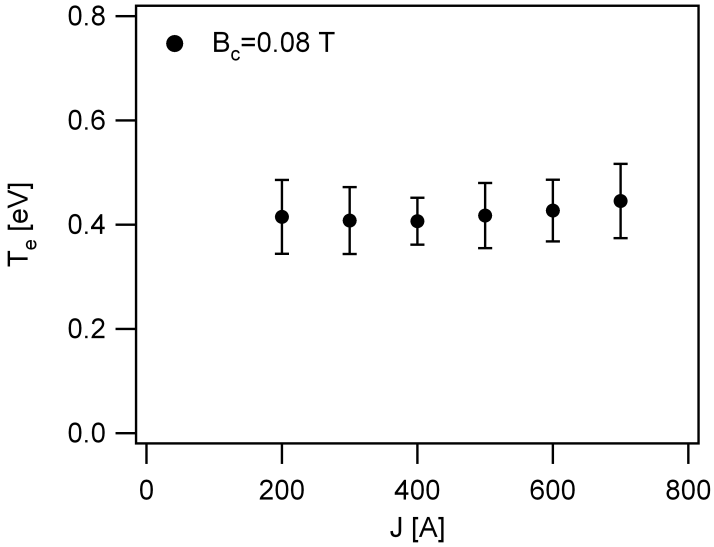

Figure 5.8: Electron Temperature, T_e, vs. thruster current, J, at the anode exit plane B_c=800 G and $\dot{m}$=20 mg/s

- **Axial decrease at thruster exit plane.** We observe from the electron temperature measurements that T_e measured at the anode exit plane is T_e=0.4 eV whereas the temperature at the cathode exit is T_e=1.5 eV[8]. This phenomenon was also observed by Randolph[54] where the measured electron temperature decreased from 1.1 eV at the back plate to roughly half as much at the anode

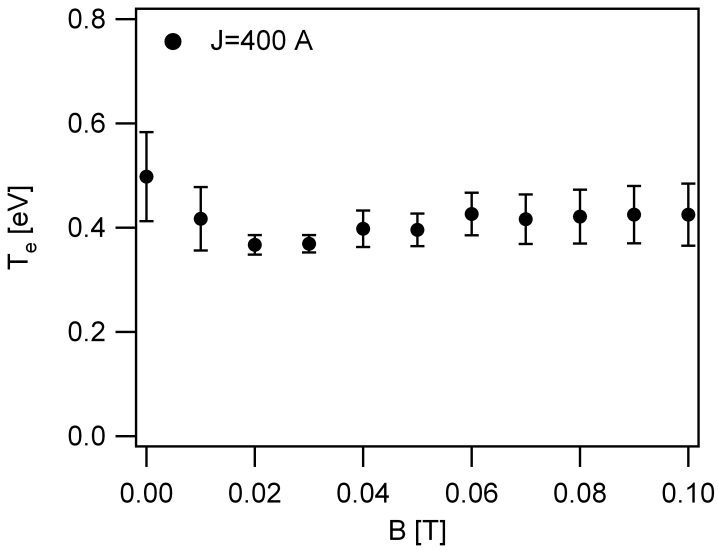

Figure 5.9: Electron Temperature, T_e, vs. applied magnetic field (B_c) at the anode exit plane J=400 A and $\dot{m}$=8 mg/s

exit plane. We can assume that this phenomenon is due to thermal expansion yet we leave this proof to future research since it is not within the scope of this thesis to model the axial electron temperature evolution in MPDTs.

5.8 Anode Temperature Measurements

In chapters 1 and 2 it was explained that the main power dissipation mechanism in MPDTs is the anode power losses which are associated with the anode sheath voltage fall, V_a. Since anode power dissipation can account for a power fraction as large as 80% in MPDTs[23, 45] which is usually on the order of kilowatts the anode absroves a large energy flux. This energy flux is responsible for heating the anode to temperatures, T_a, well above 1000 K. For this reason the anode experiences thermionic emission thus contributing to the current density balance at the anode wall. To take the thermionic emission into consideration one needs to know the anode temperature and its dependence on the thruster's operational parameters (J,B,$\dot{m}$).

The anode temperature was measured using a Leeds and Northrup disappearing

filament optical pyrometer described in section 4.5 and results corrected using the technique described in appendix C.

The anode temperature, T_a, was measured at current values between 150 A and 800 A, applied field values between 0 and 0.08 T and mass flow rate values of 5 mg/s, 8 mg/s and 20 mg/s to determine the dependence of the anode temperature on thruster current. This variety of operational parameters enables a thorough characterization of the anode temperature.

Error estimations were made at each measurement for each individual anode temperature reading according to the human operator's evaluation. The errors were then added to an estimated device sensitivity error of 25 K.

The anode temperature data are presented in Figs. 5.10-5.12.

5.9 Observations and Discussion of Anode Temperature Measurements

The observations from Figs. 5.10-5.12 are as follows:

- **Dependence on thruster current.** It can be observed from the figures that the anode temperature, T_a, increases with thruster current for all applied field and mass flow rate combinations studied. This behavior is expected since raising the current to the thruster increases the total power to the thruster and the electron current density into the anode. For this reason it does not come as a surprise that the strongest dependence of anode temperature on operational parameters is the dependence on current.

  It can also be observed from Figs. 5.10-5.12 that when no magnetic field is applied the anode temperature increases more sharply at high current values relative to those cases where B is not zero. This behavior is similar to the

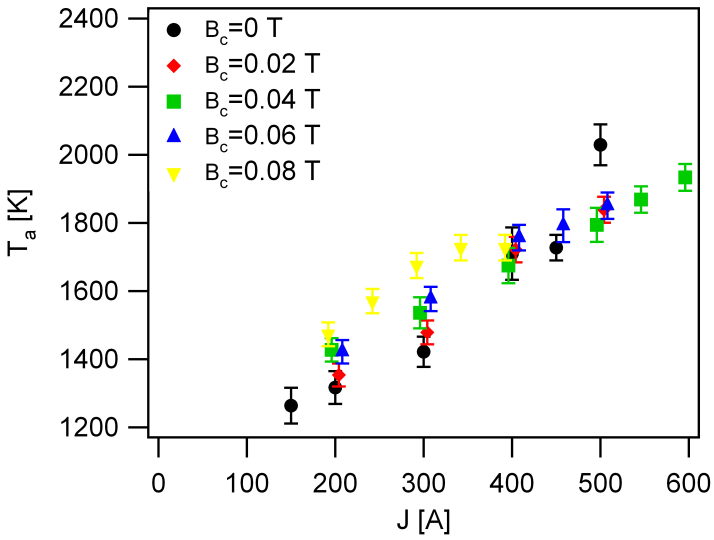

Figure 5.10: Anode Temperature, T_a, vs. thruster current, J, for different applied magnetic field values at $\dot{m}$=5 mg/s

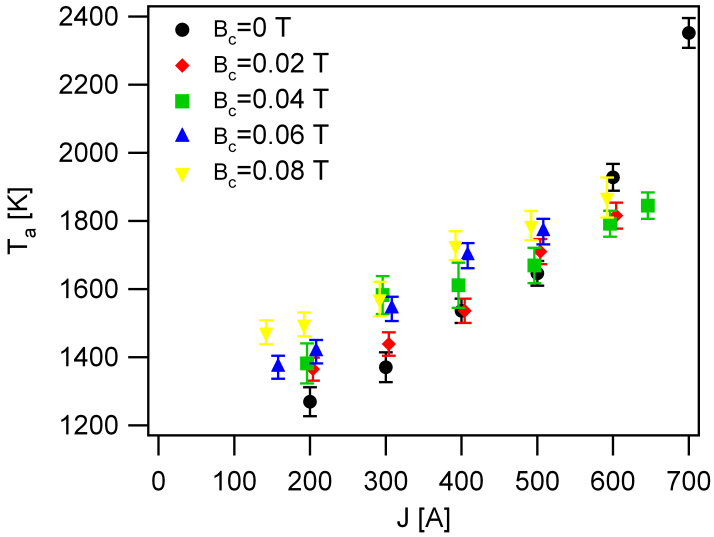

Figure 5.11: Anode Temperature, T_a, vs. thruster current, J, for different applied magnetic field values at $\dot{m}$=8 mg/s

one observed in the anode sheath voltage fall measurements and it occurs at roughly the same values of thruster current. As with anode fall measurements we can assume that a sharp increase in temperature implies the presence of the onset phenomenon. Similarly to anode fall measurements this behavior is not exhibited during operation with an applied magnetic field.

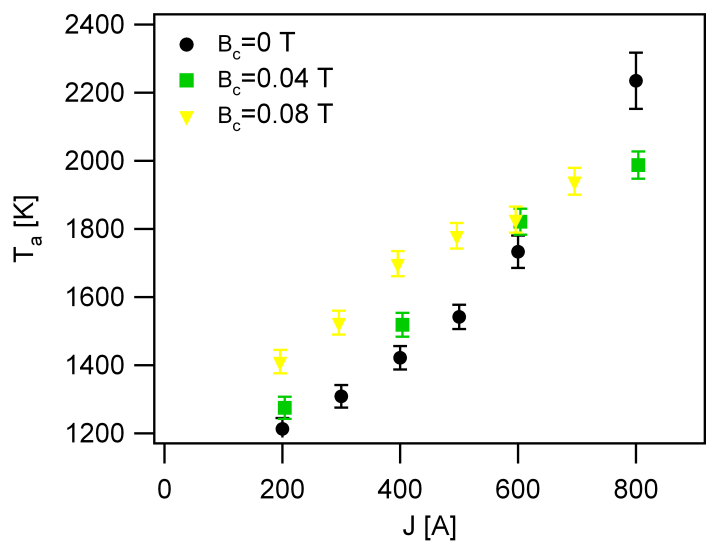

Figure 5.12: Anode Temperature, T_a, vs. thruster current, J, for different applied magnetic field values at $\dot{m}$=20 mg/s

- **Dependence on applied magnetic field.** It can be observed from the figures that the anode temperature increases with applied magnetic field for almost all cases studied. This increase is much weaker than the increase with current yet it can be explained in the same way. An increase in the applied magnetic field reduces the electron mobility into the anode thus reducing the conductivity. This reduction in conductivity requires a larger voltage fall to maintain the same thruster current. This process leads to an increase in the total thruster power with the applied magnetic field as also seen from the total voltage measurements, therefore increasing the applied field increases the power to the anode and the anode temperature.

- **Dependence on mass flow rate.** Much like the dependence on applied field the anode temperature exhibits a weak dependence on the propellant mass flow rate. The strongest influence appears in the slope of the T_a-J curves thus implying a mathematical scaling relation of the form $T_a \propto J^m/\dot{m}^n$ where m and n are positive numbers. This relation is similar to the dependence of the total thruster voltage, V_{tot}, on the mass flow rate. We expect that at low mass

flow rate values the electron number density, n_e, in the near anode region is low and any increase in thruster current increases the demand of electron current density into the anode. This demand is satisfied by an increase in anode sheath voltage fall which increases the power to the anode and the anode temperature. The electron density reduction mechanism is discussed in chapter 6.

5.10 Summary of Experimental Results

The observations made in this chapter are summarized in Tables 5.2-5.5

	Total Thruster Voltage Observations
1	Total voltage (V_{tot}) increases with applied magnetic field (B) for all values of current (J) and mass flow rate ($\dot{m}$).
2	Total voltage (V_{tot}) is more sensitive to changes in current (J) and applied magnetic field (B) at lower mass flow rate ($\dot{m}$) values.
3	Total voltage (V_{tot}) exhibits a decreasing-increasing behavior with increasing current (J) for all applied magnetic field (B) and mass flow rate ($\dot{m}$) values. Each V_{tot}-J curve has a minimum.

Table 5.2: Summary of observed trends in the V_{tot}-J curves

	Anode Sheath Voltage Fall Observations
1	Anode voltage fall (V_a) increases linearly with current (J) for all values of applied field (B) and mass flow rate ($\dot{m}$).
2	Anode voltage fall (V_a) increases sharply with current (J) at high current values for the $B = 0\ T$ cases. The value of current associated with the transition to sharply increasing V_a is lower at lower $\dot{m}$.
3	Anode voltage fall (V_a) increases with increasing applied magnetic field (B) for all values of current (J) and mass flow rate ($\dot{m}$).
4	Anode voltage fall (V_a) is higher at low mass flow rate values ($\dot{m}$) for all values of current (J) and applied magnetic field (B).

Table 5.3: Summary of observed trends in V_a-J curves

We will attempt to further explain the observations discussed in this chapter using the models presented in chapters 6 and 7.

	Electron Temperature at Anode Exit Plane Observations
1	Electron temperature at anode exit plane (T_e) is constant at about 0.4 eV for a wide range of operational parameters.
2	Electron temperature at anode exit plane (T_e) is lower than the electron temperature at the cathode exit reported by MAI.

Table 5.4: Summary of observed trends in T_e-J curves

	Anode Temperature Observations
1	Anode temperature (T_a) increases linearly with current (J) for all values of applied field (B) and mass flow rate ($\dot{m}$).
2	Anode temperature (T_a) increases sharply with current (J) at high current values for the $B = 0\ T$ cases. The value of current associated with the transition to sharply increasing T_a is lower at lower $\dot{m}$.
3	Anode temperature (T_a) increases with increasing applied magnetic field (B) for all values of current (J) and mass flow rate ($\dot{m}$).
4	Anode temperature (T_a) is higher at lower mass flow rate values ($\dot{m}$) for all values of current (J) and applied magnetic field (B).

Table 5.5: Summary of observed trends in T_a-J curves

Chapter 6

Anode Sheath Voltage Fall Semi-Empirical Model

6.1 Introduction

In chapter 1 and chapter 2 we discussed the significance of electrode energy dissipation to thrust efficiency[1]. In particular, anode power dissipation was shown to be a great contributor to MPDT and AF-MPDT energy loss via anode sheath voltage fall, V_a,[21, 23]. Furthermore, Myers et al.[23] found that in AF-MPDTs the anode sheath voltage fall scales linearly with current, linearly with applied magnetic field and inversely with propellant mass flow rate. Myers pointed out that the dependence of anode voltage fall on the applied magnetic field is challenged by the fact that the sheath size ($\lambda_{De} \sim 10^{-6}$ m) is smaller than the electron gyro-radius ($r_L \sim 10^{-4}$ m), thus electrons in the sheath are unmagnetized and ostensibly the applied magnetic field should have no effect on the anode sheath. However, previous work on self-field MPDTs[53, 21] implies that anode fall is associated with plasma pinching which might explain any dependence of the anode sheath voltage on thruster current and applied magnetic

[1]The model and experimental results presented in this chapter were presented at the 32nd International Electric Propulsion Conference at Wiesbaden, Germany[56]

field. Unfortunately, no theoretical attempt has been previously made to explain the physical mechanisms behind anode power dissipation in AF-MPDTs. It is therefore imperative that we formulate a model explaining the physics of anode sheath voltage fall phenomenon with the ability to predict its dependencies on the AF-MPDT's operational parameters, J, B_c and $\dot{m}$. Such a model will shed light on the processes that lead to anode sheath energy loss and might help in formulating future AF-MPDT design requirements.

In this chapter we formulate such a model based on a current density balance at the anode surface. We then find scaling relations for the electron density at the sheath edge ($n_e(r \simeq r_a)$) as a function of the thruster's operational parameters. We attempt to reconcile the linear dependence of anode voltage fall on the applied magnetic field through density reduction at the sheath edge due to increased plasma pinching at high applied magnetic field values. We also use empirical data presented in section 5.8 to find an expression for the anode temperature, T_a, as a function of the thruster's operational parameters. Both n_e and T_a are used in the expression for V_a. The model is compared to, and verified against, experimental data presented in section 5.4. Finally, conclusions are drawn on the physics of anode sheath voltage fall and its scaling with the thruster's operational parameters.

6.2 Assumptions

Before the model is presented we will list all the assumptions we make in the formulation of this theoretical description. We also discuss the extent of which these assumptions hold. The ultimate validity of these assumptions is in the context of the anode sheath voltage model and is supported by the ability of the model to predict the anode sheath fall experimental data presented in Chapter 5. In addition to these assumptions more minor assumptions will be introduced and discussed in the next

section.

- **The problem is one-dimensional.** We assume azimuthal symmetry in the coaxial device, thus $\partial/\partial\theta = 0$.

  We also make the assumption that the plasma properties along the z axis are constant inside the thruster between the cathode face and the anode exit plane. Since we are interested in the effects that the plasma has on the anode we ignore any evolution of properties in the plume outside of the thruster region. We also make the assumption that the anode material temperature, T_a, is axially constant. This latter assumption is supported by research performed on self-field MPDTs[57, 54], showing that the electron temperature and density exhibit little axial variation inside the thruster. The aforementioned studies support, to some extent, our assumption of axially constant plasma properties. On the other hand the assumption of constant anode temperature can be challenged since the current density pattern into the anode is not necessarily uniform and the anode is not evenly exposed to radiation from the hot cathode thus creating an uneven temperature profile. This was observed in the LiLFA by Tikhonov[28] where the anode material axial temperature profile varied within 10% of the average anode temperature. In reality the effect that this temperature variation has on the anode sheath voltage fall is due to variation in the thermionically emitted electron flux which in turn will increase the voltage fall required to sustain the total current to the thruster. Since the measured anode material temperature variation is no more than 10% we do not expect it to have any significant effect on the results of our model.

- **Electron and ion temperatures are not a function of radial position.** The electron temperature in MPDTs was shown to be almost constant radially[45, 57, 58]. A deviation from this assumption, such as a lower electron

temperature at the near anode region, will lead to a lower electron thermal velocity thus to a lower current density into the anode. A higher sheath fall is required to compensate for this deviation. However, as will be shown in the analysis, we are interested in showing that $k_B T_e \partial n_e / \partial r \gg k_B n_e \partial T_e / \partial r$ which was shown experimentally to occur in MPDTs[45] due to the strong electromagnetic pinching effect.

Similarly, the ion temperature in AF-MPDTs was shown to be constant radially in the interelectrode region[18].

- **Electron temperature does not change with mass flow rate, $\dot{m}$, applied magnetic field, B, or current, J.** It was previously shown that in MPDTs[45] the electron temperature in the near anode region is dependent on current and mass flow rate. However, the dependence of T_e is weak enough to make this assumption. It was also found in AF-MPDTs that the electron temperature is not dependent on the applied magnetic field[37].

  In addition, we found in section 5.6 that the electron temperature on the thruster's centerline at the anode axial exit plane is independent of mass flow rate, applied magnetic field, and current.

  We will hereby make the assumption that the electron temperature is T_e=2 eV which corresponds to the average of the electron temperatures previously reported by MAI[28, 29, 30] while our measurements of T_e were done at the anode exit plane and not the anode region and cannot be used in this model formulation.

- **Anode material temperature is radially uniform.** We assume that the inner and outer surfaces of the anode are at roughly the same temperature. Therefore, the anode temperature measurements presented in section 5.8 can be used for the anode inner surface temperature. The validity of this assump-

tion can be demonstrated by a heat transfer calculation for the temperature difference across the anode thickness. In steady state the energy flux passing through the anode is radiated out ($q_a = \sigma\epsilon T_a^4$). Where the temperature T_a is the temperature of the outer surface of the anode, σ is the Stephan-Boltzmann constant and ϵ is the emissivity of tungsten at temperatures above 1000 K and is $\epsilon = 0.42$[49]. The conduction equation is

$$q_a = \sigma\epsilon T_a^4 = -\kappa\frac{\partial T}{\partial r} = -\kappa\frac{\Delta T}{\Delta r} \tag{6.1}$$

where ΔT is the temperature difference between the inner and outer surfaces of the anode and Δr is the anode thickness (about 5 mm). Solving for ΔT for T_a=1500 K and κ=110 W/mK gives ΔT=5.48 K. This shows that a radially uniform anode temperature profile is a valid assumption.

- **Current attaches uniformly to the entire inner surface of the anode.** For simplicity we assume that current is uniformly attached to the entire inner surface of the anode, A_a. By making this simplification the net current density flowing into the anode, j_∞, can be written as J/A_a where J is the total current to the thruster.

  In reality, however, the current does not attach to the entire inner surface area of the anode and the effective attachment surface area, $A_{a,eff}$, is less than A_a. Oberth et al.[59], Clark[60] and Gallimore[22] showed that the magnitude of the current density into the inner anode wall can go down to no less than half of the maximum value at some sections of the anode wall. After the anode sheath fall model was formulated, to evaluate the assumption that $A_a \simeq A_{a,eff}$ we examined the change in the anode sheath voltage fall while varying $A_{a,eff}$ in the range $A_a/2 < A_{a,eff} < A_a$. The examination indicated that variation in the anode sheath voltage fall due to the smaller attachment region is negligible.

For this reason and for simplicity we assume that $A_{a,eff} = A_a$.

- **Anode's work function, ϕ_a, is constant at 3 eV.** The anode is made of tungsten and has a work function value of ϕ_a=4.54 eV. However, when the anode is perfectly coated with lithium the work function drops to about ϕ_a = 2.5 eV[13]. Since we know very little about the lithium coating state of the electrodes we make the assumption that the anode is mostly coated with lithium and that $\phi_a \simeq$3 eV. In the case in which the anode is barely coated with lithium the work function is expected to be higher thus reducing the thermionically emitted current density which leads to a reduction in the anode sheath voltage drop. Nevertheless, small deviations from our assumption at the investigated anode temperature range have little effect over the calculated anode sheath voltage drop.

6.3 Model Formulation

We start our theoretical formulation as depicted in Fig. 6.1. Although the thruster configuration in Fig. 6.1 is similar to the configuration of the LiLFA thruster, this model is generic to all types of AF-MPDTs as long as the assumptions listed in section 6.2 hold.

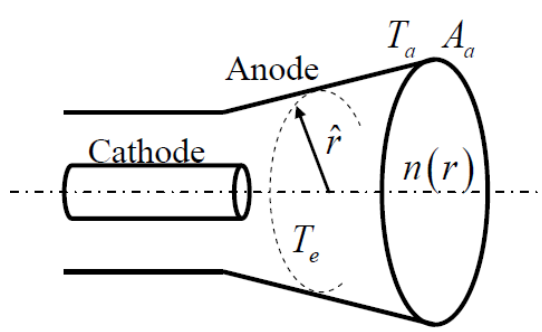

Figure 6.1: Anode voltage fall model thruster schematic.

Taking a look at a segment of the anode (Fig. 6.2), we can write a current density

balance equation[61].

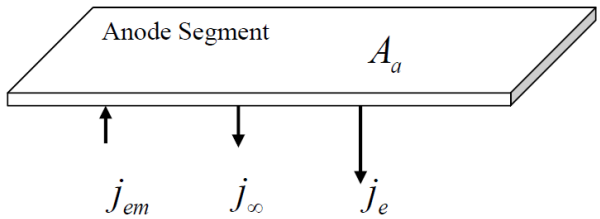

Figure 6.2: Anode voltage fall model - Current density balance at anode surface.

$$j_\infty = j_e - j_{em}, \tag{6.2}$$

where j_∞ is the net current density from the anode and can be written as

$$j_\infty = J/A_a. \tag{6.3}$$

The term j_e represents the electron current density into the anode and can be written[62] as

$$j_e = \frac{1}{4} e n_e \left(\frac{8 k_B T_e}{\pi m_e} \right)^{1/2} \exp\left(\frac{e V_a}{k_B T_e} \right) \tag{6.4}$$

where V_a is the anode sheath voltage drop and the electrons are assumed to be Maxwellian. V_a is taken to be the potential increase between the anode sheath and anode wall and is taken here to be positive for convenience.

The term j_{em} represents the thermionically emitted electron current density and can be written[63] as

$$j_{em} = A_R T_a^2 e^{(-e\phi_a / k_B T_a)} \tag{6.5}$$

where A_R is the Richardson-Dushman coefficient and is $1.2 \times 10^6\ A/m^2K^2$. Equation 6.2 indicates that the net current density from the anode is equal to the current density difference between the electron current density from the bulk plasma into the anode and the thermionically emitted electrons from the anode. Eq. 6.2 also implies

that at a given total current any increase in thermionically emitted current density will require an increase in the sheath potential drop so to increase the electron current density into the anode. Solving Eqs. 6.2-6.5 for V_a, we get

$$V_a = \frac{k_B T_e}{e} \ln \left(\frac{J/A_a + A_R T_a^2 e^{(-e\phi_a/k_B T_a)}}{\frac{1}{4} e n_e \left(\frac{8 k_B T_e}{\pi m_e} \right)^{1/2}} \right) \tag{6.6}$$

To formulate an expression for V_a as a function of the thruster's operational parameters, J, B and $\dot{m}$, we must find an expression for $n_e(J, B_c, \dot{m})$ and $T_a(J, B_c, \dot{m})$. We expect that an increase in J and B will increase the electromagnetic pinching force thus increasing the number density, n_e, at the thruster's centerline and decreasing it in the near anode region. We also expect that an increase in $\dot{m}$ will increase n_e both at the thruster's centerline and the anode sheath. Finally, we expect that an increase in J will increase the electron flux into the anode thus increasing its temperature, T_a.

6.3.1 Scaling Relations for the Radial Density Profile

We start with $n_e(J, B_c, \dot{m})$ by writing the MHD momentum equation in the radial direction

$$\rho \left[\frac{\partial u_r}{\partial t} + u_r \frac{\partial u_r}{\partial r} + \frac{u_\theta}{r} \frac{\partial u_r}{\partial \theta} + u_z \frac{\partial u_r}{\partial z} - \frac{u_\theta^2}{r} \right] = j_\theta B_z - j_z B_\theta - \frac{\partial P}{\partial r}, \tag{6.7}$$

based on our assumptions $\partial/\partial t = 0$ (steady state operation) and $\partial/\partial\theta = 0$ (azimuthal symmetry). Since in MPDTs $u_z \gg u_r$ and $u_\theta \gg u_r$ we also assume that $u_r \simeq 0$ and $\partial u_r/\partial z = 0$ based on the study conducted by Tobari on AF-MPDT[18] where the radial velocity, u_r, was found to be negligible compared with u_θ and u_z and constant axially.

We are now left with the equation

$$-\rho\frac{u_\theta^2}{r} = j_\theta B_z - j_z B_\theta - k_B(T_e + T_i)\frac{\partial n_e}{\partial r}, \tag{6.8}$$

where $\partial P/\partial r$ was written as $k_B(T_e + T_i)\partial n_e/\partial r$ under the assumption of constant radial electron and ion temperatures. Eq. 6.8 represents the balance between the centrifugal forces and density gradient forces pushing the plasma outwards while an electromagnetic pinching force constrains the plasma inwards towards the centerline.

We now use an order of magnitude analysis to determine the leading term in Eq. 6.8 that balances the density gradient term on the RHS. To do so, we use the data reported by Tobari[18] since it is the only source that includes measurements of both u_θ and j_θ that are required for this analysis. The typical values reported by Tobari are presented in Table 6.1

Property	*Typical Value*
u_θ [m/s]	10^4
r [m]	10^{-2}
ρ $[kg/m^3]$	10^{-7}
j_θ $[A/m^2]$	2×10^6
B_z [T]	2×10^{-2}
$\rho u_\theta^2/r$ $[N/m^3]$	10^3
$j_\theta B_z$ $[N/m^3]$	4×10^4

Table 6.1: Typical values of plasma properties in AF-MPDT for order-of-magnitude analysis for the pressure balance equation

We see from Table 6.1 that the centrifugal forces can be omitted since $\rho u_\theta^2/r \ll j_\theta B_z$ and the density gradient term balances the electromagnetic pinching term. Eq. 6.8 can now be written as

$$k_B(T_e + T_i)\frac{\partial n_e}{\partial r} = j_\theta B_z - j_z B_\theta = f_r\left(n_e, r, J, B, \dot{m}\right). \tag{6.9}$$

Here $f_r\left(n_e, r, J, B, \dot{m}\right)$ is the radial force density upon which we will elaborate thor-

oughly below.

To find $n_e(J, B, \dot{m})$ from Eq. 6.9, one has to develop relations for $j_\theta(r, n_e, J, B, \dot{m})$, $j_z(r, n_e, J, B, \dot{m})$ and $B_\theta(r, n_e, J, B, \dot{m})$, which is not a simple task. We avoid this by departing from a purely theoretical description of the plasma density distribution and using a few basic scaling relations derived from our current understanding of MPDT physics. These basic relations will be used to find more general relations for the plasma density with respect to the operational parameters, which in turn will be used in the anode sheath voltage fall model. Consequently, the anode sheath fall model becomes semi-empirical. However, since our ultimate goal is to find and understand trends in anode sheath voltage fall as it varies with the operational parameters, it will be sufficient for our purpose to use these scaling relations and compare them to the trends observed in the anode sheath voltage fall data. From the comparison to the experimental data conclusions and physical insights will be drawn.

We start by noting that $f_r = (\bar{j} \times \bar{B})_r = j_\theta B_z - j_z B_\theta$ represents the radial force density acting to pinch the plasma fluid. The symbol f_r represents the Lorentz force per unit volume that acts on the plasma fluid in the direction of the thruster's centerline, acting to concentrate the plasma while increasing the density towards the cathode. The radial force density, $f_r\,(n_e, r, J, B, \dot{m})$, was analitically shown by Jahn[10] in self-field MPDTs to scale in the same manner as thrust, $\mathcal{T}$, that is with J^2. The reasoning for the relation between f_r and thrust in self-field MPDTs stems from the fact that the axial current density, j_z, and the self-induced azimuthal magnetic field, B_θ, both scale linearly with current, J. We expect the same relation between the f_r and $\mathcal{T}$ to exist in AF-MPDTs where thrust was shown to be produced mainly by plasma pinching[18]. Later on we will show that the component of thrust generated by pinching scales with $(A_1 J B_c + A_2 J^2)$ where the A_1 and A_2 are proportionality constants. Therefore, we can make the assumption that f_r in AF-MPDTs is proportional to thrust ($f_r \propto (A_1 J B_c + A_2 J^2)$).

This scaling relation is not sufficient for the characterization of f_r and a solution of Eq. 6.9 since it lacks the spatial dependence of f_r on radial position; simply put, $f_r = f_r(r)$. This dependency originates from the spatial distribution of the current densities, j_z and j_θ. To find the spatial dependency of f_r we assume that the electric field is purely radial and that the applied axial magnetic field, B_z, is dominant thus $B_\theta \simeq B_r \simeq 0$. We also assume that the electric field due to radial electron pressure gradient, $\frac{1}{n_e e}\partial P_e/\partial r$, is negligible compared to the applied electric field, E_r. We base this assumption on experimental results obtained by Ando[43], who found the radial density profile to have a Gaussian shape. That is $n_e(r) = n_0 \exp\left(-(r/r_0)^2\right)$, where r_0 is the Gaussian distribution's standard deviation which is found to be in the order of $(r_a + r_c)/2$. In addition, Myers[37] found a radial density distribution that resembles a Gaussian shape yet he did not investigate this further. To validate this assumption we will verify that the radial density profile is indeed Gaussian after solving for $n_e(r)$. Using a radial density profile we can find an expression for the last term in the expression for E_r' which is $\frac{1}{n_e e}\partial P_e/\partial r = \frac{k_B T_e}{e} 2r/r_0^2$. Plugging in the typical values $\frac{k_B T_e}{e}$=2 eV, r=1 cm and r_0=1 cm leads to $\frac{1}{n_e e}\partial P_e/\partial r \simeq 4\ V/cm$. However, the typical value for the electric field drop in an MPDT is $E_r \simeq V_{tot}/(r_a - r_c) \simeq 20\ V/cm$. Although the contribution of the electron pressure gradient is about 20% of the electric field we neglect the term $\frac{1}{n_e e}\partial P_e/\partial r$ in the expression for E_r' for simplicity.

Under the above assumptions, and following Mitchner and Kruger[64], we will find this spatial dependence of f_r by using the steady-state generalized Ohm's law in θ and r which produces the following relations:

$$j_r = \sigma_0 \frac{1}{1+\Omega_e^2} E_r, \tag{6.10}$$

$$j_\theta = \sigma_0 \frac{\Omega_e}{1+\Omega_e^2} E_r. \tag{6.11}$$

Where $\sigma_0 = n_e e^2/(m_e \nu_e)$ is the scalar conductivity, Ω_e is the electron Hall parameter and E_r is the radial electric field. These two expressions present the relations between the radial electric field and the two current density components perpendicular to the applied magnetic field. The derivation of the above equations was presented by Krülle[39] for AF-MPDTs.

Now that we have an expression for j_θ we can go back to the sought $f_r(r)$ while assuming that the dominant radial force component responsible for the radial density distribution is due to the applied field ($f_r \simeq j_\theta B_z$). By using this assumption the radial force density can be written as

$$f_r = j_\theta B_z = \sigma_0 \frac{\Omega_e}{1+\Omega_e^2} B_z E_r \simeq \sigma_0 \frac{1}{\Omega_e} B_z E_r = n_e e E_r \tag{6.12}$$

where we used the fact that in AF-MPDTs $\Omega_e \gg 1$[44, 41, 22]. Eq. 6.12 gives the relation between f_r and E_r and should be sufficient for solving Eq. 6.9. We approach this by using the scaling of E_r with r as measured by Tobari[18] and Ando[43] who found it to be linear with radial position ($E_r = E_{r,0} r$) outside the sheath region which is much shorter than the typical interelectrode distance. Therefore, the spatial dependence of $f_r(r)$ is $f_r(r) \propto n_e(r) r$.

This scaling relation is in agreement with measurements taken by Tobari in AF-MPDTs[18], which showed that the radial force density to be largest at the thruster's centerline and decreases radially.

We can therefore assume that $f_r = (C_1 J B_c + C_2 J^2)\, n_e(r) r$ where the constants C_1 and C_2 are to be determined from fitting the final expression for V_a to experimental data presented in section 5.4 .

Although this expression for f_r was derived in a phenomenological manner, it still captures the fundamental dependence of the radial force density, f_r, on the operational parameters and plasma density. We must remember that our objective is

to characterize the basic scaling relations of n_e in the near anode region in order to find a scaling relation for V_a. These will be used to pursue similarities between the modeled V_a and those observed in the experiments presented in chapter 5.

We can now write Eq. 6.9 in the form of an ordinary differential equation in r

$$\frac{dn_e}{dr} = -(C_1 J B_c + C_2 J^2) n_e r \tag{6.13}$$

with the boundary condition $n_{e,r=0} = n_{e,0}$. In Eq. 6.13 the term $k_B(T_e + T_i)$ were absorbed into the constants C_1 and C_2 since it is assumed to be constant.

Since $\dot{m} = \rho A u = n_e m_i A u$ we will write $n_{e,0} = C_3 \dot{m}$ which means that as the mass flow rate to the thruster is increased so is the density at the thruster's centerline. Eq. 6.13 has the solution

$$n_e(r) = C_3 \dot{m} e^{-(C_1 J B_c + C_2 J^2) r^2}. \tag{6.14}$$

It can be seen from the radial density profile, $n_e(r)$, that the density decreases with radial position which implies a density reduction closer to the anode. This Gaussian density profile was observed in AF-MPDTs by Ando[43] and validates the assumption made earlier that $E_r > \frac{1}{n_e e} \partial P_e / \partial r$. Similarly, in MPDTs a density reduction of a few orders of magnitude was observed in the near anode region by Gallimore, Saber and Tilley[22, 45, 65]. In addition, it can be seen from the radial density profile, $n_e(r)$, that an increase in J and B_c leads to a stronger decrease in n_e with r, and to greater plasma pinching. In simple words, an increase in J and B_c results in more pinching towards the thruster's centerline as postulated earlier. We also see that an increase in $\dot{m}$ will lead to an increase in density at all radial positions. This was also expected since any addition of propellant is expected to increase the number of particles, at all locations in the thruster, thus increasing n_e.

The expression for $n_e(r)$ can now be used in the formulation for the anode voltage

drop, V_a, given in Eq. 6.6.

6.3.2 Empirical Formulation of Anode Temperature

To find an expression for $T_a(J, B, \dot{m})$ we use an empirical formulation based on anode temperature data presented in section 5.8. The best mathematical form that could be fit to the anode temperature data was

$$T_a(J, B, \dot{m}) = 1080 + 2375B_c - 5 \times 10^6\dot{m} + (1.366 - 1.33 \times 10^4\dot{m})J. \tag{6.15}$$

Figs. 6.3-6.5 show the anode temperature change with respect to current at different applied magnetic fields and mass flow rate values with the empirical fit according to Eq. 6.15. It can be seen that the empirical fit agrees with most data to within the errorbars. Some deviation exists at high current values when no magnetic field is applied. This is probably due to the *onset phenomena*, when at high current anode starvation from increased pinching leads to charge carriers supply crisis resulting in local melting of anode material that increase the electron current density to the anode surface, increasing the heat load on the anode[21, 53, 66].

The expression for $T_a(J, B_c, \dot{m})$ can now be used in the expression for the anode voltage drop, V_a, given in Eq. 6.6.

6.4 Solution and Comparison to Experimental Data

We now have a complete expression for the anode sheath voltage fall, V_a, as a function of the operational parameters, J, B_c and $\dot{m}$. This expression gives the basic scaling laws for anode sheath voltage fall and assists in understanding the fundamental scaling of the power dissipation mechanism. To verify these scaling laws one needs to show that Eq. 6.6 can predict the experimental data presented in section 5.4 and that V_a

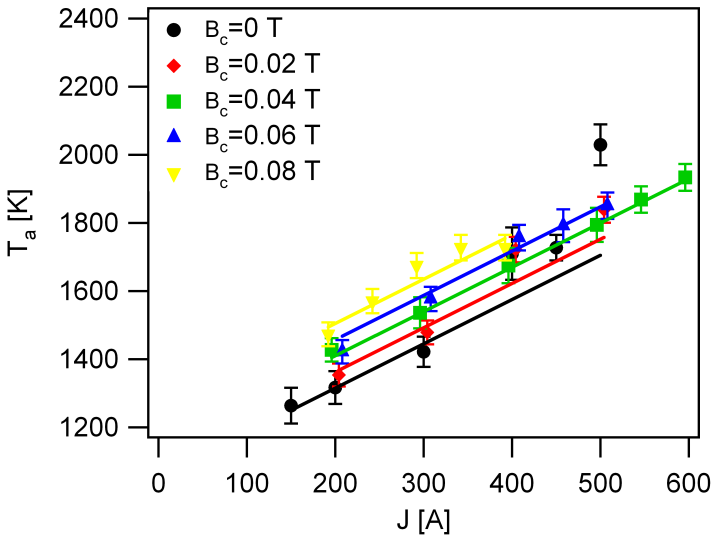

Figure 6.3: Anode Temperature vs. Current for different applied magnetic field values at $\dot{m}$=5 mg/s. The solid lines represent the empirical fit according to Eq. 6.15

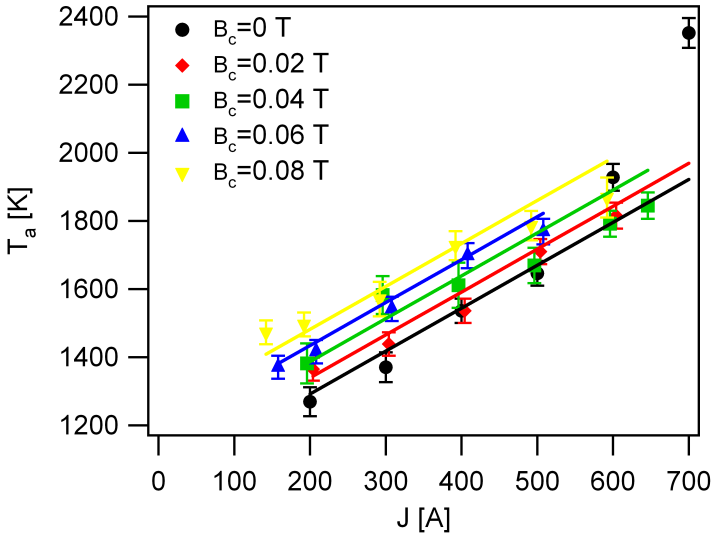

Figure 6.4: Anode Temperature vs. Current for different applied magnetic field values at $\dot{m}$=8 mg/s. The solid lines represent the empirical fit according to Eq. 6.15

exhibits the same mathematical trends with changing current, applied field and mass flow rate.

Figs. 6.6-6.8 show the anode sheath voltage fall data previously presented in section 5.4 along with curves fit according to the semi-empirical model presented in Eq. 6.6. The constants used in this model were $C_1 = 0.19$, $C_2 = 2 \times 10^{-6}$ and $C_3 = 2 \times 10^{21}$ and were found from fitting the curves to the data at B_c=0.04 T and

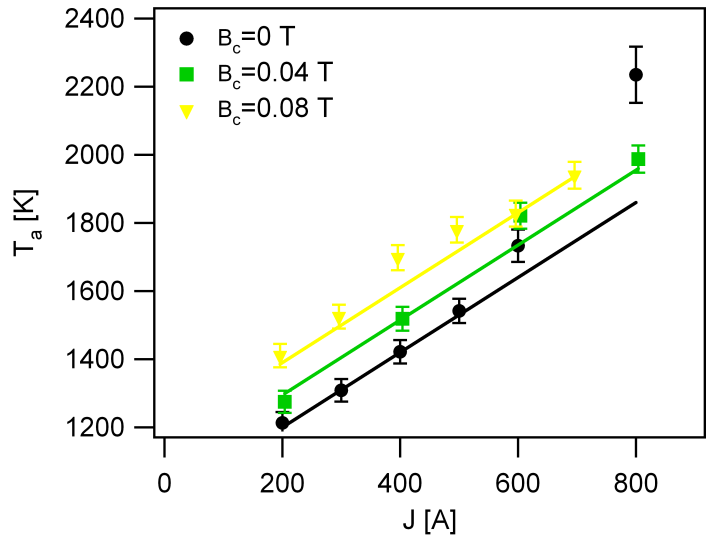

Figure 6.5: Anode Temperature vs. Current for different applied magnetic field values at $\dot{m}$=20 mg/s. The solid lines represent the empirical fit according to Eq. 6.15

$\dot{m}$=8 mg/s.

It can be seen from the figures that the semi-empirical anode voltage fall model predicts the trends in the measured data fairly well. At $\dot{m}$=5 mg/s the semi-empirical model matches the measured values at B_c=0.08 T and is close to the values of the case B_c=0 T. At the same time the model under-predicts the data for the case of B_c=0.04 T. The deviation from the measured data might be attributed to the onset phenomenon at higher current values where the anode overheats, as shown in the T_a data. This anode overheating results in an enhanced thermionic electron emission from the anode surface which leads to a higher sheath voltage than expected. This current density is countered by a larger incoming electron current density due to an increasing voltage fall. This phenomenon occurs at low mass flow rates as in our case. At $\dot{m}$=8 mg/s the semi-empirical model matches the data points very well. At $\dot{m}$=20 mg/s the model predicts the measured data quite well except for at high current values at B_c=0.08 T. We can attribute this behavior to an underestimation of the plasma density at high current, applied magnetic field and mass flow rate. One possibility is that at high mass flow rate centrifugal forces push the plasma from

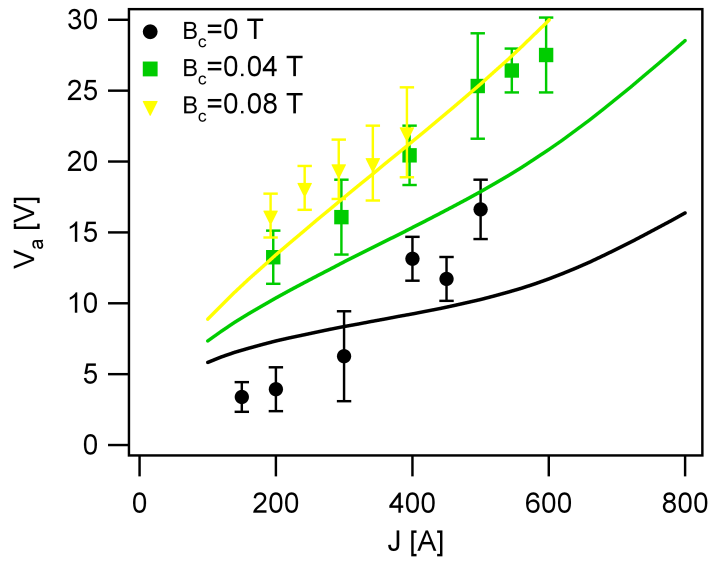

Figure 6.6: Anode sheath voltage fall vs. current for different applied magnetic field values at $\dot{m}$=5 mg/s. The solid lines represent the semi-empirical fit according to Eq. 6.6.

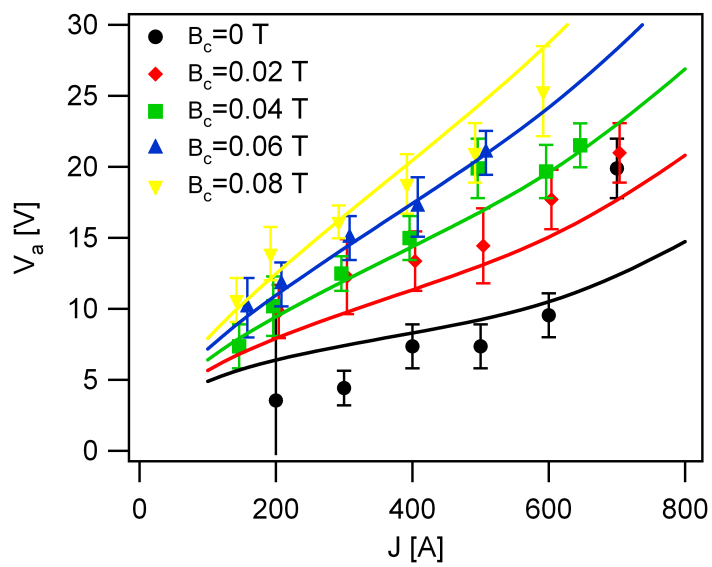

Figure 6.7: Anode sheath voltage fall vs. current for different applied magnetic field values at $\dot{m}$=8 mg/s. The solid lines represent the semi-empirical fit according to Eq. 6.6.

the thruster's center outwards while increasing the density in the near anode region. Since centrifugal force density was omitted from our derivation of n_e this effect is not taken into account. Nevertheless, the trends in predicting V_a at $\dot{m}$=20 mg/s and B_c=0.08 T are still captured.

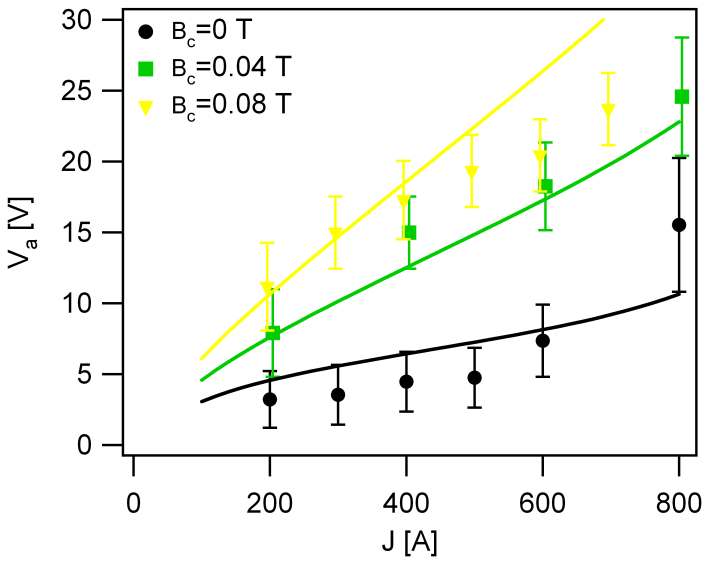

Figure 6.8: Anode sheath voltage fall vs. current for different applied magnetic field values at $\dot{m}$=20 mg/s. The solid lines represent the semi-empirical fit according to Eq. 6.6.

In general, the semi-empirical anode voltage fall model captures the trends observed from the measured data. The model predicts an increase in anode voltage fall with increasing current and applied magnetic field while predicting a mild decrease in anode voltage fall with increasing mass flow rate. The linear increase of anode voltage with current was observed in previous studies in MPDTs[22, 16]. The model also estimates a sharper increase of V_a with current at higher applied field values although this trend is not observed in all measured data.

Fig. 6.9 presents the balance between the three current density components at the anode surface according to Eq. 6.2. It can be seen from the figure that at low current values the thermionic emission is insignificant and the random electron current density into the anode balances the net current density dictated by the total current to the thruster. As the current to the thruster is increased so does the anode temperature until thermionic emission becomes significant and a larger random electron flux into the anode is required to compensate for the increasing thermionic emission. We can conclude that thermionic emission and anode temperature play important roles in the

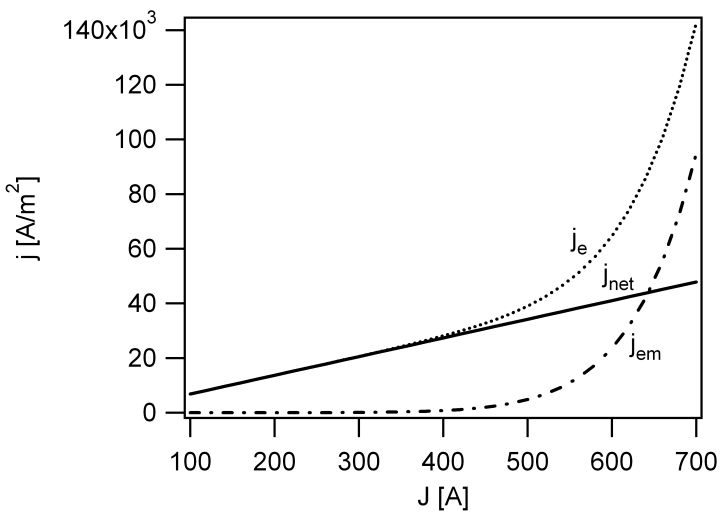

Figure 6.9: The three current density components (j_e, j_∞, j_{em}) presented in Eq. 6.2 as a function of total current, J, at B_c=0.04 T and $\dot{m}$=5 mg/s.

current density balance in AF-MPDTs and strongly affect anode sheath voltage fall.

Thermionic emission from the anode surface has implications on research conducted on quasi-steady MPDTs since the pulse length of these thrusters is too short to allow the anode temperature to reach steady-state. To support the above statement we conduct a first order estimation of the anode heating time scale and show that it is larger than the average pulse length of high power quasi-steady MPDTs.

The relation between the anode thermal properties and the thruster power is

$$P_a = \frac{C_p m \Delta T}{\Delta t}. \tag{6.16}$$

Where P_a is the power to the anode, C_p is the anode material heat capacity, m is the anode mass, ΔT is the temperature difference between room temperature and effective anode surface emission temperature and Δt is the heating time. We use the typical values for a high power quasi-steady MPDTs: $P_a \simeq 10^6$ W, $C_p \simeq 200$ J/kg K, $m \simeq 3$ kg and $\Delta T \simeq 1500$ K. The solution of Eq. 6.16 is $\Delta t = 0.9$ sec which is the time scale for anode heating to 2000 K in a quasi-steady MPDT. Quasi-steady MPDT pulse length is usually in the range $\Delta t_{pulse} \simeq 1$ millisec which is about three

orders of magnitude shorter. We can therefore conclude that the anode in a typical quasi-steady MPDT has no time to reach a temperature range that is sufficient for thermionic emission to have a significant effect on the anode sheath voltage fall, V_a. This means that operation with quasi-steady MPDTs underpredicts the performance of the thruster as V_a is expected to be lower than in steady-state operation.

6.5 Conclusions

A semi-empirical anode sheath voltage fall model was derived to find scaling relations with the thruster's operational parameters, J, B_c, $\dot{m}$, and reveal the physical mechanisms behind anode power dissipation in AF-MPDTs. The model was successfully verified against measured data and was found to predict the observed trends of the anode voltage fall with the operational parameters.

The semi-empirical model has allowed us to achieve the following physical insights.

- **The anode sheath voltage fall increases with increasing total current, J.** The random electron current density through the sheath must increase when total current to the thruster increases. To achieve this increase the anode fall has to increase so to draw more electrons through the sheath. In addition, an increase in total current enhances plasma pinching thus reducing the density in the near anode region which in turn reduces the electron current density through the sheath. This density reduction necessitates a larger voltage fall to attract more electrons through the sheath.

  It is also important to note that this increase in anode voltage fall appears to be somewhat linear with current. This observation will be used in chapter 7 in the physical interpretation of the different trends in thrust efficiency ($V_a \propto J$).

- **The anode sheath voltage fall increases with increasing applied field, B_c.** An increase in the applied magnetic field leads to an increase of the pinching

force towards the thruster's centerline which in turn decreases the density in the near anode region. This decrease in density leads to a decrease in density as previously mentioned. It should be noted that even though the electrons are not magnetized in the anode sheath the applied magnetic field affects the sheath potential fall indirectly by increasing the plasma pinching and reducing the plasma density at the sheath.

It is also important to note that much like the increase with current the anode voltage fall seems to be linear with applied magnetic field ($V_a \propto B_c$).

- **The anode sheath voltage fall decreases with increasing mass flow rate, $\dot{m}$.** Propellant mass flow rate affects the anode sheath voltage fall by altering the density in the near anode region. An increase in mass flow rate leads to an increase in density which in turn increases the electron random flux into the anode. When the electron current density into the anode is larger, a lower sheath voltage is required to maintain the same total current. It can be seen from Eq. 6.6 that the anode voltage fall has a weak dependence on the mass flow rate ($V_a \propto \ln(1/\dot{m})$) as observed both through the data presented in section 5.4 and in AF-MPDTs in Ref.[23].

- **Thermionic emission from the anode has an effect on the anode sheath voltage fall.** Using our model we have shown that thermionic emission from the anode surface is responsible for reducing the net current density into the anode and increasing the required anode sheath voltage fall necessary to maintain current density balance at the anode surface. This fact has important design implications on the choice of anode material since it is desirable to reduce anode thermionic emission by choosing materials with high work function values. In addition, this conclusion has implications on testing and experimentation of MPDTs since quasi-steady operation does not exhibit the anode thermal effects

due to the short operation time. Therefore steady-state operation of MPDTs should be preferable for power balance examination, as was the case of our study, to best capture the anode thermal effects that tend to increase the anode power requirements.

Finally, this phenomenon was observed in high power arcjets by Golz[67] who found the total thruster voltage to be lower at the same operating conditions when the anode was water-cooled. It is likely that the lower voltage is due to lower thermionic emission and so to lower required sheath voltage fall.

- **The anode sheath voltage fall scales quadratically with anode radius.** Using the expression for the anode sheath voltage fall from Eq. 6.6 ($V_a \propto \ln\left[1/(r_a^2 n_e(r = r_a))\right]$) and the expression for the radial density distribution presented in Eq. 6.14 ($n_e(r = r_a) \propto e^{-r_a^2}$), the relation between V_a and r_a is shown to be quadratic ($V_a \propto r_a^2$). This comes in accordance with previous research conducted by Myers[23] who also demonstrated the anode sheath voltage fall to be quadratically proportional to the anode radius. This serves as a confirmation for the semi-empirical anode sheath voltage fall model.

Chapter 7

Thrust Efficiency Model

7.1 Introduction

To date, there has not been a thorough study of thrust efficiency, η, in AF-MPDTs and little is known about the dominant physical mechanisms determining efficiency within different parameter regimes. Such a study will be the aim of this chapter, which will be achieved by examining data obtained from LiLFA operation and presented in previous chapters[1].

In chapter 1 we discussed the importance of voltage-current characteristics to efficiency estimations by explaining that thrust efficiency can be regarded as the ratio of the back electromotive voltage component, V_{emf}, to the total voltage, V_{tot}, as shown in Eq. 7.1.

$$\eta = \frac{V_{emf}}{V_{tot}} = \frac{V_{emf}}{V_{emf} + \frac{1}{J}P_{res} + V_E} \tag{7.1}$$

For this reason estimating the efficiency depends on an understanding of the physics behind different voltage components in AF-MPDTs and an ability to predict their scaling relations with the thruster's operational parameters (J,B,$\dot{m}$).

[1]Part of the model and experimental results presented in this chapter were accepted for publication in the Journal of propulsion and power[68] as well as presented at the 46th Joint Propulsion Conference at Nashville, TN[69]

In this chapter a general thrust efficiency model is formulated and trends analyzed for a better understanding of efficiency determination in AF-MPDTs. We start in section 7.2 by formulating a model for the different voltage components in the LiLFA and their scaling relations with the operational parameters. The model is verified by comparing the predicted total voltage to the measured total voltage presented in chapter 5. We then proceed to use the models to form an expression for the efficiency as a function of the operational parameters. We analyze the efficiency and its scalability with J, B_c and $\dot{m}$ at different parameter regimes and draw conclusions regarding the different physical processes underlying the scaling of the thrust efficiency. We conclude by analyzing the general AF-MPDT performance while identifying beneficial operating regimes.

7.2 Total Thruster Voltage Model

We start by listing the assumptions made in the formulation of this model. We continue with particularizing the voltage components found in an AF-MPDT while adopting a semi-empirical thrust model postulated by Tikhonov[8], to derive an expression for V_{emf}. All the voltage components are added to form an expression for the total voltage, V_{tot}, which is then compared to the experimental data presented in chapter 5. This voltage model will enable us to form an expression for the thrust efficiency in the LiLFA and obtain physical insights of efficiency determination in AF-MPDTs.

7.2.1 Assumptions

Before the model is presented we will list all the assumptions we make in the formulation of this theoretical description. We will also discuss the validity of each assumption and the effect that its violation may have on the final conclusions.

- **The plasma is singly and fully ionized.** In order to make a convenient estimation of power associated with internal modes we assume that, for the case of lithium, all plasma is ionized and none of the ions is in excited state. This assumption is strengthened by Randolph[54] who showed that the plasma in MPDTs is fully ionized at different operational conditions. Choueiri and Randolph[55] suggested and verified that even though ionization occurs through resistive effects the bulk electron temperature does not influence the ionization process which is due to super-thermal tail in the electron velocity distribution.

  This assumption is questionable in low current regimes where the power associated with ionization is a significant fraction of the total power. This happens at high mass flow rates and current value range of less than 200 A; where ionization requires more than one-third of the total power. Any conclusions drawn on the physical nature of voltage components at this regime should be regarded with caution.

- **Electron temperature values.** We assume that the electron temperature has the following values:

  1. At cathode exit T_e=1.5 eV[8]
  2. In the acceleration region T_e=0.4 eV[section 5.6]
  3. In the near anode region T_e=2 eV[28, 29, 30].

  While T_e=1.5 eV reported by MAI was measured far away from the acceleration region, which in AF-MPDTs is in the plume[41], we use the electron temperature measured at the anode exit plane.

- **Conversion of thermal to kinetic power is important only in the cathode region.** We assume that the conversion of thermal power to kinetic power is through expansion of hot gas into vacuum at the cathode exit. This con-

tribution of electrothermal power to thrust will be captured in the expression for thrust used in this study and presented in subsection 7.2.3. On the other hand, the conversion of thermal power to kinetic power in other regions of the thruster is negligible due to the low number densities associated with MPDT operation[20].

In addition, the LiLFA is not designed to efficiently convert the thermal power into kinetic power, like arcjets or resistojets, since it does not have a constrictor or a converging-diverging nozzle.

- **The ion temperature is constant at 1 eV.** It was shown by Fradkin[17] that the ion temperature in a lithium-fed AF-MPDTs is of the same order of magnitude as the electron temperature. Therefore we make the assumption that the ion temperature is on the order of a few electron-volts and equals 1 eV.

  Deviations from this assumption have little influence on the voltage model since as will be shown the power invested in plasma heating is less than 1 kW and has the largest effect on the total voltage at the low current regime. This current regime is of low interest due to the low exhaust velocities associated with it.

- **Electrode work function (ϕ_W) is constant at 3 eV.** The anode and cathode are made from tungsten and have a work function of ϕ_W=4.54 eV. However, when the electrodes are perfectly coated with lithium the work function drops to about $\phi_W = 2.5$ eV[13]. Since we know very little about the lithium coating state of the electrodes we make the assumption that they are mostly coated with lithium thus $\phi_W \simeq$3 eV. To validate making this assumption the sensitivity of the total thruster voltage to changes in ϕ_W between 3 eV and 4 eV was examined and total voltage showed to change no more than several percent. In addition, we assume the same work function for both electrodes.

- **Cathode sheath voltage fall is negligible.** The cathode sheath voltage

drop in MPDTs is much lower than the anode fall. In the LiLFA the cathode voltage fall was measured at MAI to be 1-3 V[31]. Since the values of the cathode sheath drop are very low compared with other voltage components and the physics behind cathode sheath was not investigated in this thesis we neglect this voltage contribution while keeping in mind that small deviations of the model from the measured data might originate from this voltage component and its dependence on the thruster's operational parameters.

7.2.2 Model Formulation

We start our model formulation by finding a mathematical expression for each of the voltage components corresponding to the power components presented in section 1.4.

1. **Back electromotive voltage.** The back electromotive voltage, V_{emf}, or kinetic voltage, $V_{kinetic}$, is the ratio of the kinetic power to the total thruster current. This voltage component consists of the contribution of both the directed and undirected kinetic voltages. The directed kinetic voltage is associated with thrust production, $V_{directed} = \mathcal{T}^2/2J\dot{m}$, while the undirected kinetic power does not contribute to thruster performance and reduces the thruster's efficiency. Therefore, it can be written

$$V_{emf} = V_{directed} + V_{undirected} = \frac{\mathcal{T}^2}{2\dot{m}J}(1+\alpha), \tag{7.2}$$

where α is the fraction of total kinetic power that goes into undirected kinetic power. This value of α was investigated by Villani[16] and found to be about 1/4 in an argon-fed self-field MPD thruster. However, in this study we assume that the addition of applied magnetic field contributes to beam centering thus $\alpha \simeq 0$. Under this assumption the back electromotive voltage, V_{emf}, can be

written as

$$V_{emf} = \frac{\mathcal{T}^2}{2\dot{m}J} \tag{7.3}$$

where the thrust, $\mathcal{T}$, is a function of the thruster's operational parameters. It is obvious now that thrust and voltage are intertwined and one cannot construct a proper voltage model or understand the physics behind it without the knowledge and understanding of the thrust. For this reason in our analysis we employed a thrust model composed by Tikhonov[8]. This model and its validity will be elaborated upon in subsections 7.2.3 and 7.2.4.

2. **Plasma Heating dissipation voltage.** The voltage representing the power to plasma heating can be written as

$$V_{heat} = \frac{\dot{m}}{m_i J}(k_B T_e + k_B T_i). \tag{7.4}$$

where the ratio $\dot{m}/m_i$ represents the number of injected propellant atoms per unit time. We will assume that T_e=0.4 eV as measured in section 5.6 and T_i=1 eV as explained in subsection 7.2.1.

3. **Internal Modes.** The voltage representing the power to internal modes can be written as

$$V_i = \frac{\dot{m}}{m_i J}\epsilon_i. \tag{7.5}$$

where ϵ_i is the ionization energy for lithium and is ϵ_i=5.39 eV. As mentioned in subsection 7.2.1 it was assumed here that the plasma is singly and fully ionized and the ions are not further excited.

4. **Electrodes work function.** The voltage invested into extracting electrons from the anode and cathode surfaces is simply ϕ_W for each electrode, thus $2\phi_W$ for both the anode and cathode together. We assume that $\phi_W \simeq 3$ eV thus the total voltage invested in electrons extraction from the electrodes is 6 eV.

5. **Electrodes sheaths.** We employ the semi-empirical expression for anode sheath voltage fall derived in chapter 6

$$V_a = \frac{k_B T_e}{e} \ln \left(\frac{J/A_a + A_R T_a^2 e^{(-\frac{e\phi_a}{k_B T_a})}}{\frac{1}{4} e n_e \left(\frac{8 k_B T_e}{\pi m_e} \right)^{1/2}} \right) \tag{7.6}$$

with

$$n_e = C_3 \dot{m} e^{-(C_1 J B_c + C_2 J^2)} \tag{7.7}$$

and

$$T_a(J, B, \dot{m}) = 1080 + 2375 B_c - 5 \times 10^6 \dot{m} + (1.366 - 1.33 \times 10^4 \dot{m}) J. \tag{7.8}$$

Although the mathematical form of this expression is quite complicated we observed in chapter 6 that the anode sheath voltage fall is somewhat linear with both current and applied magnetic field ($V_a \propto J$ and $V_a \propto B_c$). This scaling with current and applied magnetic field should be kept in mind while interpreting the different trends in efficiency with the operational parameters.

Since this expression for the anode sheath voltage fall is determined by using experimental results the final expression for the total thruster voltage will be semi-empirical as well. Nevertheless, this model is suitable for the LiLFA and will be tested for validation against the total voltage data taken on the LiLFA. Since this model still captures the fundamental physics of AF-MPDTs it will aid in finding the scaling relations with the operational parameters and elucidate the physics of AF-MPDTs in general.

All of the voltage components listed are part of the total voltage model. The model and comparison to experimental data will be presented in subsection 7.2.5.

7.2.3 Tikhonov's Semi-Empirical Thrust Formula

As discussed in subsection 7.2.2, to estimate and understand the physics behind the back electromotive voltage, V_{emf}, we employ a semi-empirical thrust model derived and verified experimentally by Tikhonov[8]. Tikhonov's thrust relation, shown below, was formulated based on experimental study conducted on the same 30 kW LiLFA we used in our study as well as on higher power (> 100 kW) versions of this thruster[28, 30, 32]:

$$\mathcal{T}(J) = K_{self}J^2 + K_H(2r_a)B_aJ + K_{gd}\dot{m}a_0. \tag{7.9}$$

In Eq. 7.9, the first term on the right hand side represents the self-field component of thrust, the second term represents the applied-field component (which scales as the product JB_a), and the third term represents the gas dynamic contribution. Here B_a is the applied magnetic field at the anode face ($B_a = B_c/2$ in the LiLFA) and a_0 is the sonic speed at the cathode exit. For the sonic speed we take $a_0 = \sqrt{k_B(\gamma_e T_e + \gamma_i T_i)/m_i}$ with electron and ion temperatures of 1.5 eV at the cathode exit as was measured for T_e by Tikhonov using probes. We assume that $T_e = T_i$ based on the fact that in AF-MPDTs both temperatures were shown to be at the same order of magnitude [17]. We also assume that the specific heat ratio is taken to be that of a monatomic gas ($\gamma = 5/3$). The sonic speed is therefore $a_0 = 8.3 \times 10^3$ m/s. K_{self}, K_H and K_{gd} are the self-field, Hall and gas dynamic thrust coefficients and have the values: $K_{self} = \left[\frac{3}{4} + \ln\left(\frac{r_a}{r_c}\right)\right] \times 10^{-7} = 1.76 \times 10^{-7}$, $K_H = 0.1$ and $K_{gd} = \left(1 + \frac{1}{\gamma_e}\right) = 1.6$ as given by Tikhonov[8].

We note that since the sonic speed (a_0) is a function of temperature (T_e and T_i) it is also a function of current since an increase in current might lead to an increase in T_e. It was shown in previous studies on self-field[58] and applied field[37] MPDTs that the electron temperature has a weak dependence on current and therefore so does the sonic speed which is proportional to the square root of the electron temperature.

Since this relationship between the sonic speed and current is weak we assume for simplicity that the sonic speed is constant with current.

We note that the AF-MPDT is designed to operate at current regimes in which the self-induced magnetic field generates thrust values that are low compared to the applied field and gas dynamic thrust components. The mathematical dependence of thrust on current and applied magnetic field was formulated by using data from the 30 kW, 150 kW and 200 kW lithium-fed AF-MPDTs[25, 28, 29, 30, 31] for a variety of current, applied-field and mass flow rate values. The constants K_{self}, K_H and K_{gd} in Eq. 7.9 were verified [25] by comparing Eq. 7.9 to experimental data taken at MAI on the 30 kW LiLFA as shown in Fig. 7.1. It can be seen that while a few of the

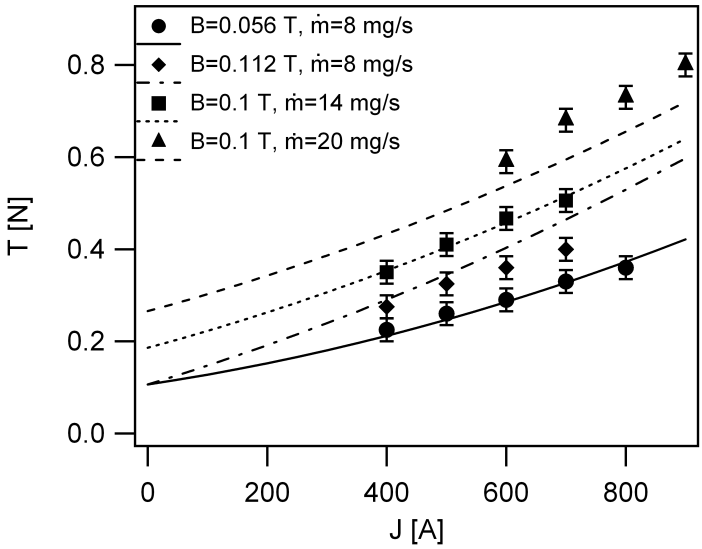

Figure 7.1: Thrust measurements taken at MAI on the 30 kW LiLFA along with Tikhonov's semi-empirical model.

experimental data points do not coincide very well with the model's curves the thrust model does depict the trends correctly and can be used to estimate, to within 9%, the thrust generated by the 30 kW LiLFA at different operating conditions.

7.2.4 Validity of Tikhonov's Thrust Formula

As seen from Fig. 7.1 the experimental data are limited to current values higher than 400 A, therefore any analysis conducted at lower current values using extrapolation from these data should be regarded with caution. One must remember that when no current is applied the thruster generates only cold thrust, which originates from thermal expansion through the heated cathode, and all $\mathcal{T}$-J curves must eventually pass near the origin in Fig. 7.1. The cold thrust in the LiLFA is in the order of 0.01 N which is an order of magnitude lower than the thrust estimated at an operating current of 400 A. For this reason we will constrict our analysis to measurements taken above 400 A and only comment on possible physical reasoning for measurements at lower current regime.

In general, the low current operational regime is characterized by low self-field and applied field contributions such that the majority of thrust originates from gas dynamic effects from current heating the cathode. As discussed in chapter 5 this operational regime is similar to the arcjet thruster operational regime where the current to mass flow rate ratio is lower than in MPDTs and the plasma is weakly to partially ionized. For this reason this low current regime is of little interest to the study of MPDTs in general and AF-MPDTs in particular.

It is important to note that even though Tikhonov's semi-empirical thrust model was derived for the Lithium MPD thruster class built in MAI, it correctly exhibits the same trends observed in AF-MPDTs in other facilities at a variety of thruster power values, thruster geometries and propellants[17, 36, 38, 70, 71, 72]. These trends show linear increase of thrust with an increase in the product JB. This repetitive trend for a vast number of different conditions implies a similar physical mechanism behind thrust scaling in AF-MPDTs. We can therefore assume that the effect that these linear trends in thrust have on trends in efficiency are similar in other types of thrusters operating in a variety of conditions. At the same time we emphasize

that the thrust generation mechanism behind AF-MPDT is not yet understood for all current regimes, especially at low current values and so this empirical formulation should not be regarded as universal for all types of AF-MPDTs at all current regimes.

7.2.5 Solution and Comparison to Experimental Data

Total thruster voltage, V_{tot}, is the addition of all the individual voltage components listed in subsection 7.2.2. The expression for the total voltage can be written as

$$V_{tot} = V_{emf} + V_{heat} + V_i + 2\phi_W + V_a. \tag{7.10}$$

In order to validate the total voltage model we compare it to the experimental data presented in section 5.1. The results are presented in Figs. 7.2-7.4.

It can be seen from the figures that the semi-empirical voltage model predicts well the values and trends of the total thruster voltage observed from experiments. In Fig. 7.2 ($\dot{m}$=5 mg/s) the model accurately predicts the voltage trends with current for all three applied field values, although it underestimates the actual voltage values at B_c=0.04 T and B_c=0.08 T, In Fig. 7.3 ($\dot{m}$=8 mg/s) the model predicts very well the trends and voltage values for all applied field cases with the exception of the B_c=0 T case in which it over-estimates the values by no more than 20%. In Fig. 7.4 ($\dot{m}$=20 mg/s) the model matches the trends presented; however, it over-predicts the measured values by up to 15%.

In general we can conclude that the total thruster voltage model predicts the measured voltage trends with the operational parameters very well. The increasing trends with increasing applied magnetic field are captured by the model as well as the decreasing V-J slope at high mass flow rate values. In addition, the decreasing-increasing trend with current is also captured by the model although the low current regime should be regarded with caution due to the extrapolation of Tikhonov's thrust

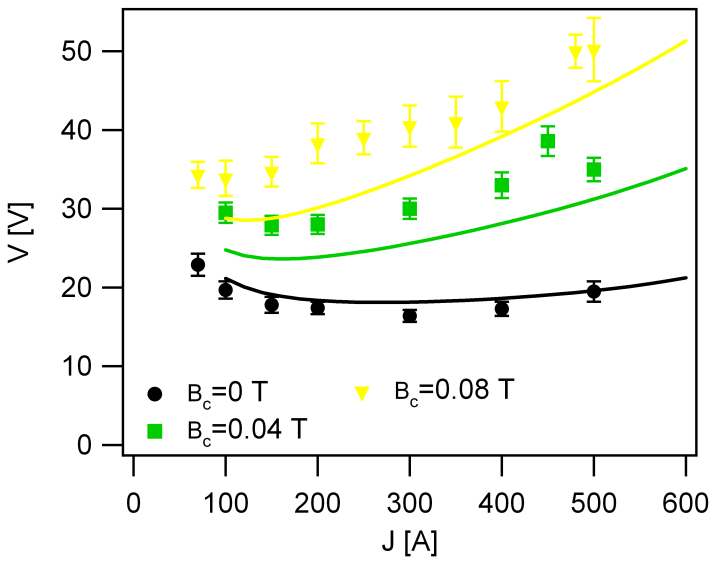

Figure 7.2: Total thruster voltage vs. current for different applied magnetic field values at $\dot{m}$=5 mg/s. The solid lines represent the semi-empirical fit according to Eq. 7.10

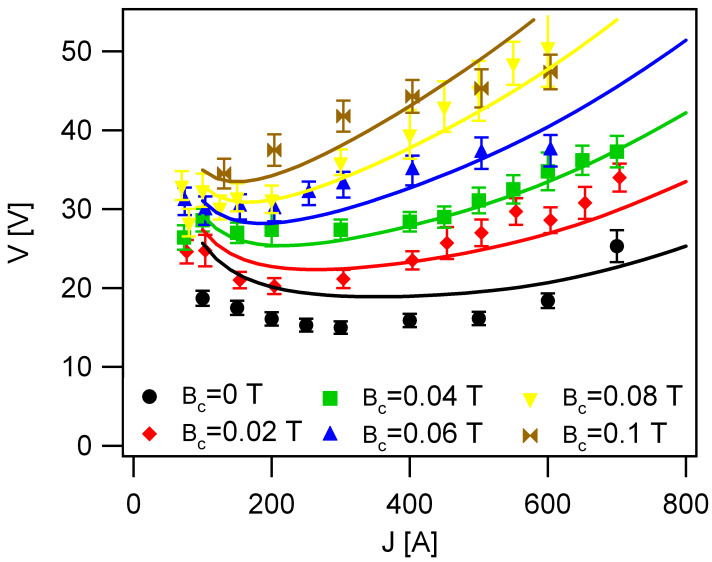

Figure 7.3: Total thruster voltage vs. current for different applied magnetic field values at $\dot{m}$=8 mg/s. The solid lines represent the semi-empirical fit according to Eq. 7.10

model in that regime.

Although the observed trends in voltage are predicted by the voltage model fairly well it seems like the voltage model somewhat underestimates the voltage values at low mass flow rates and over-predicts the voltage values at high mass flow rates. This

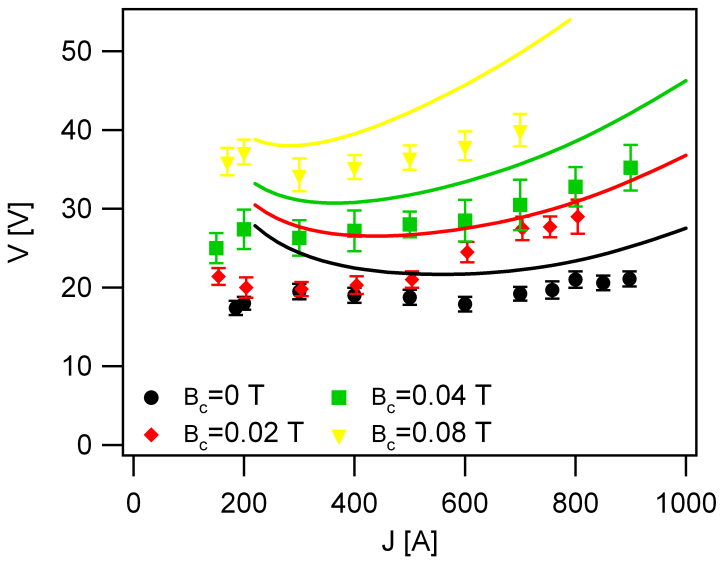

Figure 7.4: Total thruster voltage vs. current for different applied magnetic field values at $\dot{m}$=20 mg/s. The solid lines represent the semi-empirical fit according to Eq. 7.10

implies on a somewhat weaker dependence on mass flow rate in the model relative to that measured. We will speculate on this when examining the individual voltage components and their trends with the operational parameters.

Now that we have validated the total thruster voltage model we can investigate the thrust efficiency and contribution of each voltage component and its trends with the operational parameters.

7.3 Efficiency Trends

7.3.1 Observations

Using the voltage model, we calculate the efficiency according to Eq. 7.1. The efficiency trends for mass flow rate values of $\dot{m}$=5 mg/s, $\dot{m}$=10 mg/s and $\dot{m}$=20 mg/s are presented in Figs. 7.5-7.7.

It can be observed from the figures that for all cases presented the efficiency increases with increasing magnetic field. For the case of $\dot{m}$ = 5 mg/s the efficiency

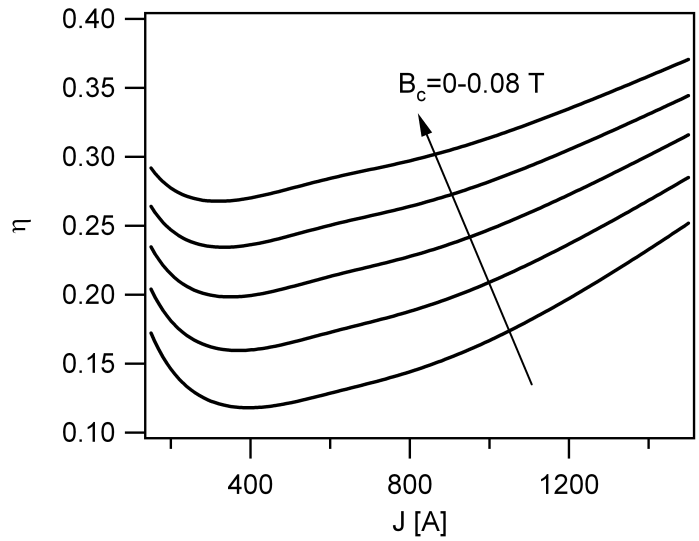

Figure 7.5: Efficiency vs. current curves at $\dot{m}$=5 mg/s based on Eq. 7.1

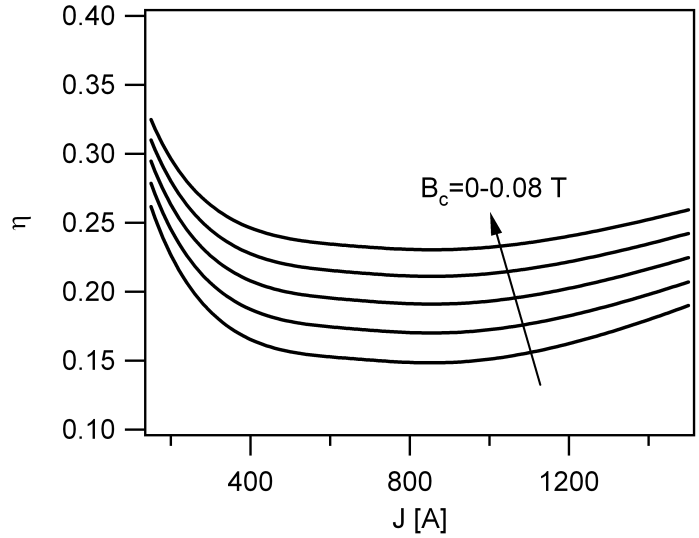

Figure 7.6: Efficiency vs. current curves at $\dot{m}$=10 mg/s based on Eq. 7.1

increases with B_c by as much as 120% from $\eta = 0.12$ to $\eta = 0.27$ at $J = 400$ A. This increase in efficiency is higher for low mass flow rate values, i.e. the lower the mass flow rate the greater the increase in efficiency with the applied field. This can be illustrated by plotting efficiency against applied magnetic field for different current and two mass flow rate values. The sensitivity of the increase with applied field at low mass flow rate values is evident from Figs. 7.9(a) and 7.9(b) where the increase at $\dot{m}$=20 mg/sec is clearly weaker than the increase at $\dot{m}$=5 mg/sec. This efficiency

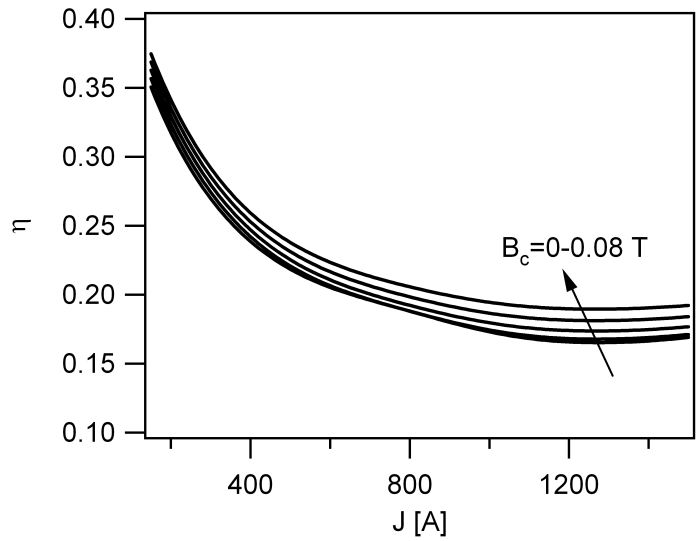

Figure 7.7: Efficiency vs. current curves at $\dot{m}$=20 mg/s based on Eq. 7.1

increase with applied field was also observed by Paganucci[12] and Myers[38] who found similar trends.

The mass flow rate also affects the slope of the η-J curves. The lower the mass flow rate the greater the slope. Much like the total voltage curves the η-J curves at $\dot{m}$ = 20 mg/s are flatter than at $\dot{m}$ = 5 mg/s. We conclude that the efficiency is more sensitive to changes in current and applied magnetic field at low mass flow rate values. This phenomenon was also observed in a 100 kW lithium AF-MPDT[27] at MAI.

It can also be observed that for all cases presented, the efficiency has a decreasing-increasing trend with increasing current similarly to total voltage. Therefore each curve has a minimum point associated with it. Moreover, the minimum point moves to lower current values with an increasing applied field while moving to higher current values with increasing mass flow rate. This phenomenon has not previously been reported in literature due to the lack of voltage data over a broad current regime.

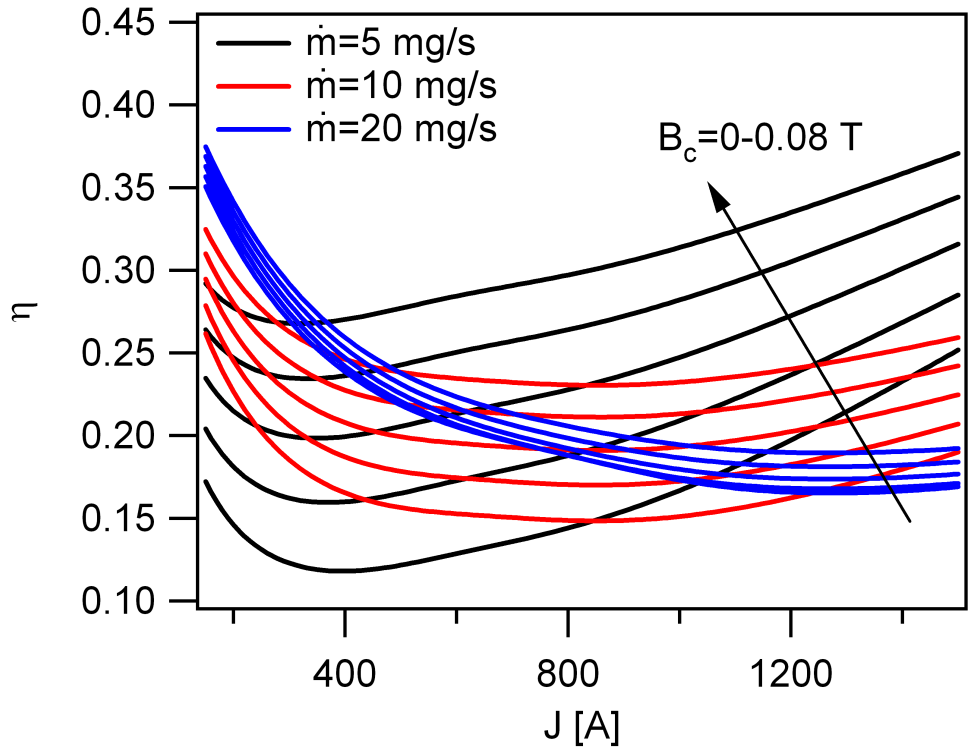

Figure 7.8: Efficiency vs. current curves for a variety of applied magnetic field values between 0 T and 0.08 T and mass flow rate values of 5 mg/s (black), 10 mg/s (red) and 20 mg/s (blue) based on Eq. 7.1

7.3.2 Physical Interpretation

Armed with the experimentally verified models we can now seek physical interpretation of the observed trends. This understanding can be used to interpret the observations presented in subsection 7.3.1.

We start by writing the full expression for the back electromotive voltage component, V_{emf}, by plugging Tikhonov's expression for thrust (Eq. 7.9) into the general expression for V_{emf} (Eq. 7.3). The full expression for V_{emf} is therefore

$$\begin{aligned} V_{emf} &= \frac{\mathcal{T}^2}{2\dot{m}J} \\ &= \frac{K_{gd}^2}{2}a_0^2\frac{\dot{m}}{J} + K_{gd}K_H a_0(2r_a)B_a + \frac{K_H^2(2r_a)^2}{2}\frac{B_a^2 J}{\dot{m}} + \\ &\quad K_{gd}K_{self}a_0 J + K_H K_{self}(2r_a)\frac{B_a J^2}{\dot{m}} + \frac{K_{self}^2}{2}.\frac{J^3}{\dot{m}} \end{aligned} \tag{7.11}$$

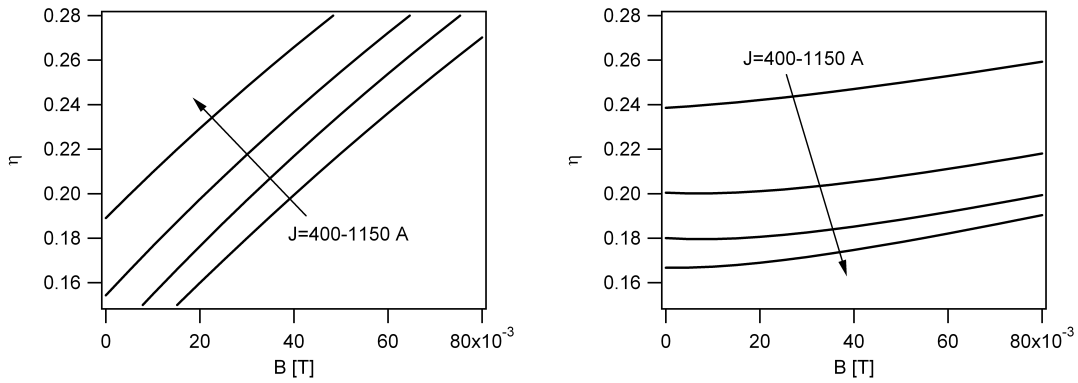

(a) $\dot{m}$=5 mg/sec (b) $\dot{m}$=20 mg/sec

Figure 7.9: Efficiency vs. applied magnetic field for different current values at $\dot{m}$=5 mg/sec and $\dot{m}$=20 mg/sec

The first three terms represent the contribution of the gas dynamic and applied filed component to thrust. The last three components represent the contribution of the self-field component of thrust and are negligible at current values less than about 800 A.

The primary observation made is that the efficiency increases with increasing applied magnetic field. The reason for this behavior is found from Eqs. 7.10 and 7.11, where the efficiency is seen to be greater when the useful voltage component (V_{emf}) increases faster than the non-useful voltage ($V_{tot} - V_{emf}$) with increasing applied magnetic field. Since V_{emf} scales with B^2 while the non-useful voltage scales roughly with B there is a general increase of the efficiency with B. From our observations of the last term in Eq. 7.10 we concluded that anode sheath power losses scale linearly with the applied field. Therefore the useful power increases faster than the non-useful power with increasing applied field. It is important to mention that this interpretation is valid not only for the LiLFA but for AF-MPDTs in general since in AF-MPDTs $\mathcal{T} \propto B$ thus $\mathcal{T}^2/(2J\dot{m}) \propto B^2$ and as was found in chapter 6 and by Myers[23] and Gallimore[24], $V_a \propto B$. For this reason the efficiency is expected to rise with applied field in a variety of AF-MPDTs.

We also observed that the increase in efficiency with increasing current and applied

field is more sensitive when the mass flow rate is lower. This can be corroborated with the fact that the back electromotive voltage scales with $(JB^2)/\dot{m}$ as seen in the third term in Eq. 7.11. Any changes in current or applied field will be greater for lower values of mass flow rate. This means that the enhancement of the efficiency by the applied magnetic field is greater when the mass flow rate is reduced. Physically speaking as the current increases so does thrust, exhaust velocity, and back electromotive voltage. At lower mass flow rates any increase in current and therefore thrust leads to a greater increase in exhaust velocity, which leads to a higher back electromotive voltage requirement.

The decreasing-increasing behavior of efficiency with increasing current can be explained by considering the contribution of each thrust component to the back electromotive voltage (Eq. 7.11). Each one of the three thrust components dominates thrust production in different current regimes according to Eq. 7.9. The thrust regime characterized by the lowest current values is the gas dynamic regime. This can be seen from Eq. 7.9 and Fig. 7.1 where at low current values the thrust is dominated by the current-independent constant $K_{gd}a_0\dot{m}$. The gas dynamic thrust component contributes the quantity $K_{gd}^2 a_0^2 \dot{m}/2J$ to the back electromotive voltage and therefore will decrease with increasing current. The reduction in this voltage component will contribute to the reduction in efficiency. When increasing the current even further the applied field component of thrust begins to dominate. This can be seen in Fig. 7.1 where at intermediate current values the thrust consists mostly of the value of the applied field component, $K_H(2r_a)B_aJ$. The applied field thrust component contributes the quantity $K_H^2(2r_a)^2B_a^2J/2\dot{m}$ to the back electromotive voltage thus scaling linearly with current much like the non-useful voltage. For this reason the efficiency curve flattens out and then begins to rise when the self-field component of thrust becomes larger.

7.4 Relative Magnitude of the Power Dissipation Components

The efficiency model derived in this chapter enables the examination of the relative magnitude of the power dissipation components, the power deposited into the electrodes and resistive power dissipation. The electrode and resistive losses power fractions, P_E/P_{tot} and P_{res}/P_{tot}, are plotted in Figs. 7.10 and 7.11 respectively.

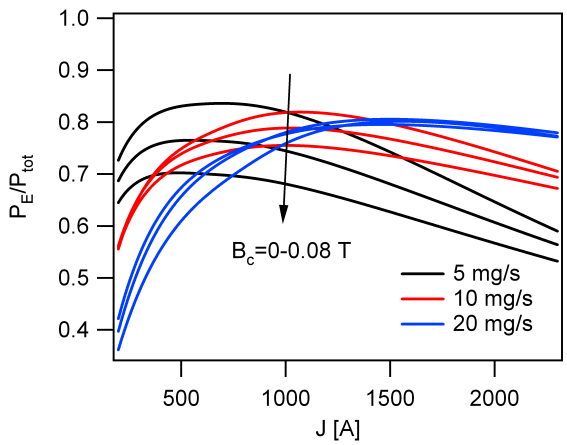

Figure 7.10: Electrode power fraction vs. current for B_c=0-0.08 T at mass flow rate values of 5 mg/s, 10 mg/s and 20 mg/s.

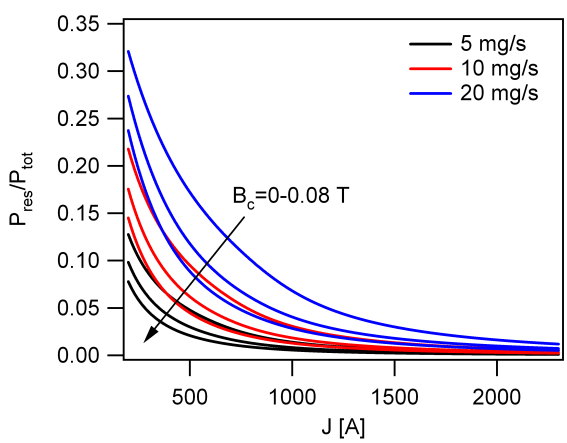

Figure 7.11: Resistive losses power fraction vs. current for B_c=0-0.08 T at mass flow rate values of 5 mg/s, 10 mg/s and 20 mg/s.

It can be observed from the figures that the dominant power dissipation mechanism is electrode power losses which take up to 85% of the total thruster power in the

case of no applied magnetic field. The high relative energetic cost of the electrodes, primarily the anode sheath power, is common in MPDTs and was observed to be in the same range of magnitude by Saber[45], Gallimore[22] and Diamant[21] in self-field MPDTs and by Myers[23] and Gallimore[24] in AF-MPDTs. It can also be observed from Fig. 7.10 that the electrode power fraction is lower at higher applied fields. This is due to efficiency increase with applied field as was explained in Subsection 7.3.2. In addition it can be seen that the electrode power fraction is low at the low current regime and increases with increasing current. This behavior is due to high resistive losses power fraction at low current, also observed in Fig. 7.11. As the power to plasma heating and ionization is constant the total thruster power increases with current, thus the resistive losses power fraction is decreasing with current. For this reason the higher the mass flow rate, the greater the resistive losses power fraction since more power is required for ionization and plasma heating. As the current is increased further the electrode power fraction decrease because of a faster increase of the acceleration power with current. Lastly, the resistive power losses, which are highest at low current values, can take up to a third of the total power and thus are significant at this current regime.

Overall, the results presented in Figs. 7.10 and 7.11 suggest that operation at high current and high applied magnetic field is preferred. However, this will be further investigated in the rest of this chapter.

7.5 Limitations to Efficiency Model

7.5.1 The Low Current Regime

In general, the efficiency varies between $\eta \simeq 0.1$ and $\eta \simeq 0.4$ in the current regime inspected. One must bear in mind that the low current regime under 400 A, where efficiency is highest, has large uncertainty due to the lack of thrust data in this regime.

However, the decreasing trend in efficiency in the low current region is expected since in this region a significant portion of the total power is invested in heating and ionizing the gaseous propellant while the acceleration is mainly electrothermal with constant power invested into acceleration as current varies. At the same time, the electrode power dissipation increases with current. For this reason as current increases, more power is dissipated into the electrodes and decreasing the efficiency. At high mass flow rates the electrothermal acceleration mechanism remains dominant with larger currents, which causes the decreasing trend to extend to higher current regimes. This can be illustrated by examining the different voltage components as they change with current for one particular case at B_c=0.04 T and $\dot{m}$=8 mg/s (Fig. 7.12). It is observed

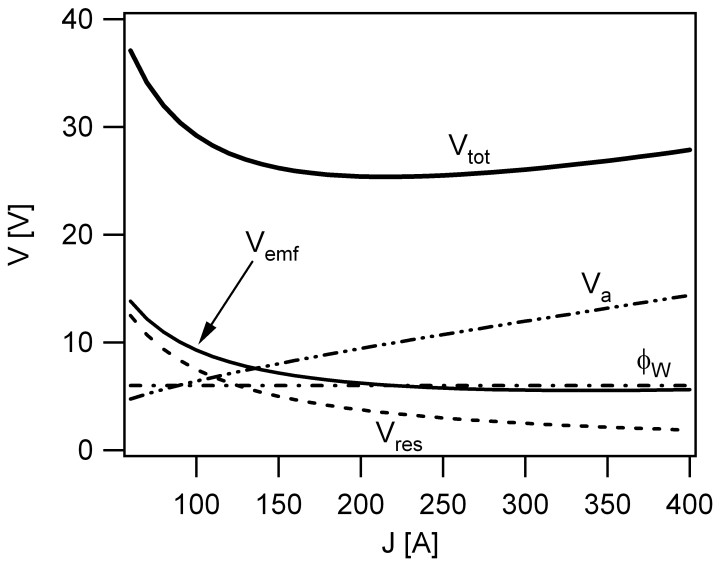

Figure 7.12: Breakdown of the different voltage components at low current regime for B_c=0.04 T and $\dot{m}$=8 mg/s

from Fig. 7.12 that while the back electromotive and resistive voltages decrease with current, the anode sheath voltage fall increases and the thrust efficiency decreases. This trend changes when the applied-field component of thrust becomes more dominant and the back electromotive force starts increasing with current. Nevertheless, since this low current regime is of high uncertainty the voltage trend with current should be regarded as qualitative.

7.5.2 Onset Phenomenon

A major restriction on thruster operation is caused by the onset phenomenon which limits operation at the high current regime. This phenomenon, also mentioned in chapter 6, is a major limiting one for MPDT operation and in self-field MPDTs depends on the factor $J^2/\dot{m}$[21, 53, 66]. Onset appears at lower current when operating at low mass flow rates, thus MPDT operation at high power should take place at higher mass flow rates. To estimate this limitation we calculate the conventional ionization current, J_{ci}, for the three mass flow rate values investigated here. The ionization current, which is the current that corresponds to exhaust velocities sufficient for ionization, was shown to be a good estimation parameter of the limiting current in MPDTs as the onset usually appears at $J_{onset} \simeq 2J_{ci}$[5]. In addition, since the physics of onset in AF-MPDTs are unknown, we calculate J_{ci} only for the non-applied field operation case in which the onset limitation prediction was experimentally verified.

The conventional expression for J_{ci} is[11]

$$J_{ci} = \left[\left(\frac{2\epsilon_i}{m_i} \right)^{1/2} \frac{\dot{m}}{\frac{\mu_0}{4\pi} \left(\ln(r_a/r_c) + 3/4 \right)} \right]^{1/2} . \tag{7.12}$$

The corresponding values of J_{onset} can be seen in Fig. 7.13 where the critical current is plotted against mass flow rate. It is observed from the figure that at $\dot{m}$=5 mg/sec the operation is limited to under 1176 A whereas at higher mass flow rate values the operation is limited to higher values of current. In Fig. 7.14 efficiency is plotted against current only in the valid current regime prior to the predicted manifestation of the onset phenomenon. For low mass flow rates, efficiency increases more strongly with current than at high mass flow rates. However, as we see in Fig. 7.14 these low mass flow rate regimes are prematurely cut-off due to the onset phenomenon. Therefore we can, in fact, achieve similar efficiencies at higher mass flow rates and higher currents before we reach onset.

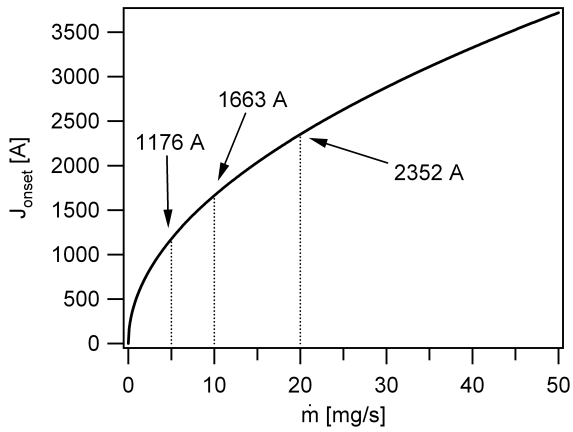

Figure 7.13: Onset current vs mass flow rate

Although the analysis conducted here led to some important conclusions, we must bear in mind that J_{onset} is not well defined and was found to be higher or lower in various experiments depending on the electrode materials and geometry[21]. This limitation is of great importance to AF-MPDT operation and should be properly investigated in future research to enable the understanding of the dependence of J_{onset} on the applied magnetic field.

While it may seem like operation at low mass flow rates and high applied magnetic field is the most beneficial operating regime for MPDTs, one must remember that other performance parameters are influenced by the operational regime chosen. These parameters are specific impulse, thrust and thrust to power ratio. Therefore, before we draw conclusions on optimal operational parameters we must examine the thruster's overall performance. This is done in section 7.6.

7.6 Performance Analysis

In this section we will look at AF-MPDT performance parameters other than efficiency and attempt to define some basic design criteria suitable to possible mission requirements.

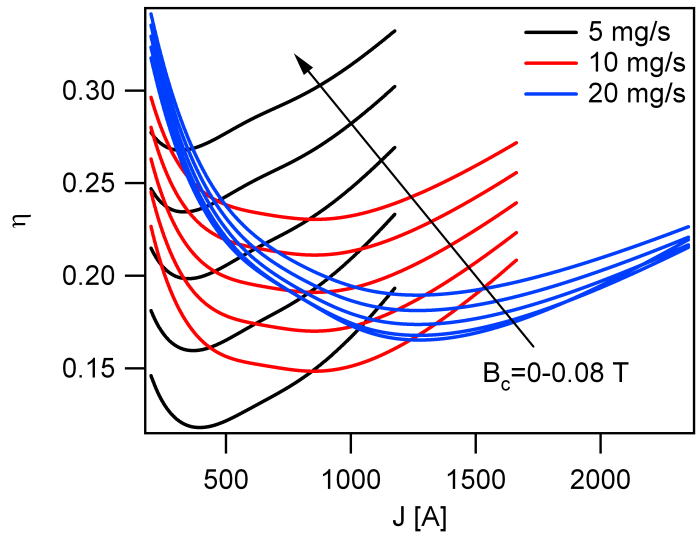

Figure 7.14: Efficiency vs current for the sub-critical current range at each mass flow rate

7.6.1 Specific Impulse

The specific impulse, Isp, is proportional to the exhaust velocity, Isp= u_e/g_0 where $g_0 = 9.81\ m/s^2$. According to the rocket equation, the higher the specific impulse the less propellant is required to carry out a specific mission. For this reason mission designers will be more inclined to chose an operational point that corresponds to the highest specific impulse. Since in AF-MPDTs $\mathcal{T} \propto JB$ the specific impulse will scale with $JB/\dot{m}$ which implies that operation at high current, high applied magnetic field and low mass flow rate is desired for a high specific impulse and low propellant mass fraction. This is illustrated in Fig. 7.15 where specific impulse is plotted for a range of applied fields and mass flow rate values. It is seen from the figure that the specific impulse monotonically increases with current and applied field and decreases with mass flow rate. To achieve highest specific impulse it is therefore beneficial to operate at high current and applied field and low mass flow rate regime.

It is important to note that operation at the above mentioned regime is limited by onset at high current which restricts operation at low mass flow rates. In addition, as shown in chapter 5 the above mentioned regime is characterized by high

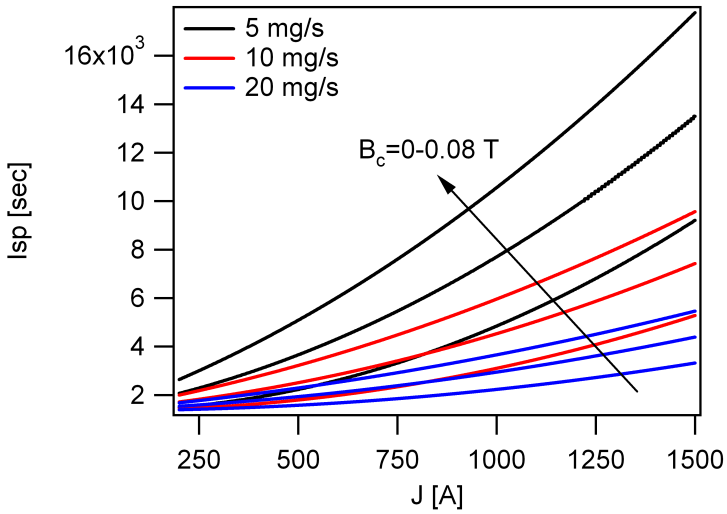

Figure 7.15: Specific Impulse vs current at B_c=0-0.08 T and $\dot{m}$=5 mg/s, $\dot{m}$=10 mg/s and $\dot{m}$=20 mg/s

electrode temperatures which pose an engineering limitation to thruster operation as the thruster might need additional cooling or experience rapid erosion which would shorten the lifetime.

7.6.2 Thrust

Thrust, $\mathcal{T}$, is an important performance parameter as it defines mission duration. High thrust is usually required for near-Earth missions where mission trip time has to compete with chemical based propulsion systems. In AF-MPDTs thrust is proportional to JB hence operation at high current and applied magnetic field is desirable. Also, since the current operational regime in AF-MPDTs is lower than that of self-field MPDTs the electrothermal contribution to thrust is significant[11] and high mass flow rate operation leads to higher thrust. This is illustrated in Fig. 7.16 where thrust and efficiency are plotted against current at B_c=0.08 T for three different mass flow rate values. It can be observed from the figure that for a given chosen current, thrust is higher at high mass flow rate values. For example, at a current of 750 A thrust goes from 0.35 N to about 0.54 N when increasing the mass flow rate from 5 mg/s to

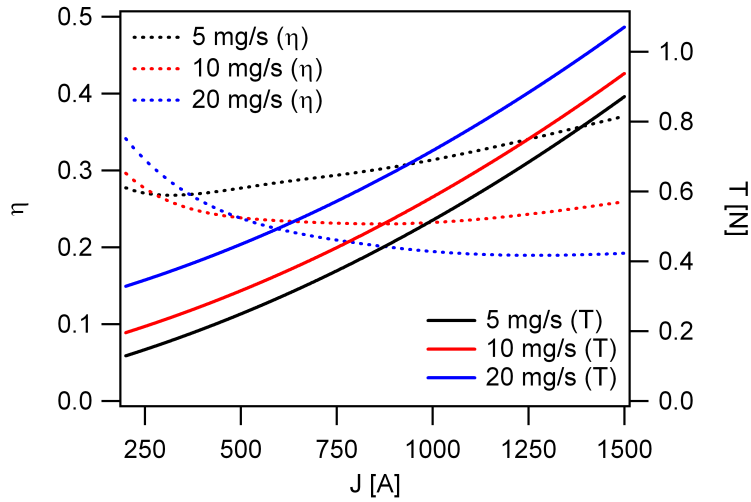

Figure 7.16: Efficiency and thrust vs current at B_c=0.08 T for $\dot{m}$=5 mg/s, $\dot{m}$=10 mg/s and $\dot{m}$=20 mg/s

20 mg/s. This increase of almost 55% in thrust might lead to significant reduction of mission duration. At the same time efficiency goes up by only about 38% when reducing the mass flow rate from 20 mg/s to 5 mg/s. These illustrate the trade-offs that would be important in planning a mission.

It is important to note that operation at high mass flow rate is typically associated with initial propellant mass thus might cause spacecraft contamination issues[73] since more propellant is ejected per unit time.

7.6.3 Thrust to Power Ratio

Both specific impulse and efficiency examinations indicate that operation at high current and high applied field is preferable, yet the choice of the optimal operational point should take into consideration the increase of one performance parameter over the increase of the other. An increase in efficiency leads to total power reduction while an increase in specific impulse requires higher power, for fixed mass flow rate. A good performance parameter that takes this relative magnitude into consideration is the

thrust-to-power ratio, since it is dependent on both specific impulse and efficiency:

$$\mathcal{T}/P = \frac{2\eta}{I_{sp}g_0}. \tag{7.13}$$

The thrust-to-power ratio is plotted against specific impulse in Fig. 7.17 at B_c=0.08 T for three different mass flow rate values. It is seen from the figure that the thrust-

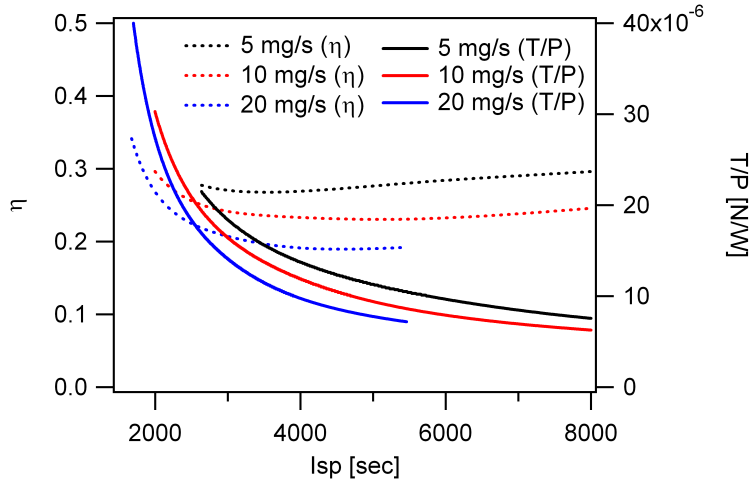

Figure 7.17: Efficiency and thrust to power ratio vs current at B_c=0.08 T for $\dot{m}$=5 mg/s, $\dot{m}$=10 mg/s and $\dot{m}$=20 mg/s

to-power ratio decreases quickly with specific impulse since at low specific impulse efficiency is highest thus less power is needed to reach the required exhaust velocity. At this range there are significant differences between high and low mass flow rate operation. On the other hand, in the high specific impulse range, the thrust-to-power ratio is converging to a constant value. We conclude from Fig. 7.17 that operation at high specific impulse leads to a low thrust-to-power ratio which is greater at lower mass flow rate.

The trend of the thrust-to-power ratio emphasizes what has been previously discussed. That is, a higher thrust corresponds to lower specific impulse and efficiency whereas high specific impulse comes at the cost of thrust and mission duration. Given the brief performance analysis conducted here, mission designers can decide on initial

thruster design criteria according to the mission objectives.

Chapter 8

Conclusions

The goal of this dissertation was to characterize and find scaling relations for the thrust efficiency with respect to the thruster's operational parameters (J,B,$\dot{m}$). This led to the characterization of the different power dissipation mechanisms in AF-MPDTs with an emphasis on anode sheath losses. It was shown through the review of past research that thus far only qualitative conclusions, to the most part, have been drawn on the scaling of efficiency and anode sheath losses. Although several experimental attempts were made to characterize efficiency, no study spanned a wide enough parameter space to make a conclusive assessment of the scaling of efficiency or the different power dissipation mechanisms.

Our approach in this dissertation was twofold: experimental and analytical. We experimentally carried out a detailed investigation of the total voltage, anode sheath voltage fall, anode temperature and electron temperature at the anode exit plane over a wide range of parameter space in an AF-MPDT. Using the experimental results along with a semi-empirical thrust model, we were able to characterize thrust efficiency and the different power dissipation mechanisms in AF-MPDTs. We analytically characterized and derived scaling relations for the anode sheath voltage fall while attempting to identify important physical processes in its determination. Both

the experimental and analytical investigations contributed to the formation of a semi-empirical efficiency model for AF-MPDTs. Using the efficiency model, various trends and scaling relations with the thruster's operational parameters were demonstrated. These scaling relations corroborate and augment the conclusions drawn from previous research.

Lastly, utilizing the thrust and efficiency models we carried out a brief overview of the performance parameters. These are: specific impulse, thrust and thrust-to-power ratio.

The physical insights from our study are summarized in the next section.

8.1 Physical Insights

Our experimental and analytical studies conducted on efficiency and power dissipation mechanisms in AF-MPDTs provide physical insights that broaden the understanding of efficiency determination in AF-MPDTs. The fundamental insights are given as follows:

- Efficiency increases linearly with applied magnetic field, B. This increase was attributed to the scaling of thrust and the back electromotive voltage with the applied magnetic field. the increase in back-electromotive voltage was found to be greater than the increase of the non-useful voltage, which is dominated by the anode sheath voltage fall.

- Curves of efficiency as a function of current have a decreasing-increasing behavior with a minimum point that is affected by both the applied magnetic field and the mass flow rate. This behavior is a result of an interchange between the different thrust components, each of which dominates in a different current regime, and thus affects the scalability of the back-electromotive voltage component.

- Curves of efficiency as a function of current show that η is more sensitive to changes in current and applied magnetic field at low mass flow rate values. This behavior is attributed to the higher back-electromotive voltage at low mass flow rates ($V_{emf} \propto 1/\dot{m}$); therefore, increases in V_{emf} due to an increase in J or B are more sensitive at low mass flow rate values.

- Power dissipation in AF-MPDTs is dominated by anode sheath power losses except in the low current regime where resistive losses dominate.

- Anode sheath voltage fall increases linearly with increasing applied field, B and increasing current, J. This phenomenon can be ascribed to the reduction of plasma density in the near anode region due to increased radial force density at higher values of applied field and current.

- Anode sheath voltage fall decreases with increasing mass flow rate ($\dot{m}$). This behavior is attributed to the increase of electron density in the near anode region at higher mass flow rate values. This increase in electron density necessitates a decrease in anode sheath voltage fall to maintain current density balance at the sheath edge.

- Thermionic emission from the anode influences the anode sheath voltage fall. Anode temperature, and thus thermionic emission from the anode surface, is affected by the thruster's operational parameters. The higher the thermionic emission, the greater the anode sheath voltage fall to maintain current density balance into the anode. Anode material with a high work function is preferred to lower thermionic emission.

In addition to the conclusions specified above, the detailed theoretical models for anode sheath voltage fall and total thruster voltage provide physical insights and a greater understanding of the processes that affect the different voltage components,

which determine the efficiency in AF-MPDTs. The anode sheath voltage fall model was able to predict the observed experimental trends and could explain the increase in voltage fall with increasing applied magnetic field that was not understood in past research. This model demonstrated consistent results with past experimental studies conducted on both self-field and applied-field MPDTs.

The total voltage model predicted the trends and scaling relations from the experimental results. This model enabled the creation of an efficiency map as a function of the thruster's operational parameters. The results and scaling relations of the total voltage model are consistent with previous research.

8.2 Future Work

While the semi-empirical models and experimental studies presented in this dissertation have led to the verification of the physical mechanisms behind the scaling relations of AF-MPDT thrust efficiency. However, a number of questions still remain unanswered and should be addressed in the future to better understand the physical mechanisms behind efficiency determination.

Most importantly, since efficiency trends in the low current regime could be characterized in this study only qualitatively, further detailed investigation of this regime is needed. This study should include both thrust and total voltage measurements as well as measurements of the ionization fraction. In this study it was assumed for simplicity that the electrothermal component of thrust does not scale with current. In reality this term does scale with current and is significant mainly in the low current regime where the applied and self field components of thrust are of low magnitude. Further investigation of the dependence of the cathode and plasma temperatures on current in the low current regime will aid in forming an adequate model for this regime. The knowledge of both thrust and total voltage in the low current regime

will shed light on the physical processes in this regime and will enable the formulation of new models to characterize this regime.

Secondly, the onset phenomena under the influence of an applied magnetic field is still vague and was never fully investigated in AF-MPDTs. In our study it was unclear whether or not the thruster crossed the onset limit. To investigate this phenomenon, the AF-MPDT has to be operated at increasing values of current while measurements of anode and cathode erosion are simultaneously performed. In addition, fast voltage fluctuations in the range of hundreds of kHz should accompany the high erosion rate associated with the onset phenomenon and can likely be measured.

Thirdly, although the model for the anode sheath voltage fall derived in this study enabled the prediction of various scaling relations with the operational parameters, it is a semi-empirical model and thus unable to predict the actual values of anode sheath voltage fall. To make the model purely theoretical one needs to fully characterize and calculate the radial force density, f_r. This can be done by modeling the magnetic field, $\bar{B}$, and current density, $\bar{j}$, as they vary spatially inside the thruster. Experimental data can aid in formulating and verifying the theoretical model for both vector fields and enabling the calculation of f_r.

Lastly, although we examined the change in efficiency over a wide range of applied magnetic field values, it will be interesting to examine trends in efficiency at even higher values of applied field. It is possible that with a further increase of applied field, plasma pinching would be limited due to plasma diffusion effects, thus limiting additional increases in thrust. This limitation in thrust could cause a reduction in efficiency with increasing thruster power. This is merely a qualitative assessment and we suggest that it be properly tested in future research.

Appendix A

Emissive Langmuir Probe Apparatus

A.1 Theoretical Background

The expression for measured current in a cold langmuir probe is

$$I_p = I_{is} - I_{es} \exp\left[-\frac{e(\Phi - V_p)}{k_B T_e}\right] \tag{A.1}$$

where I_p is the measured current, Φ is the plasma potential, V_p is the probe potential, k is Boltzmann constant and T_e is the electron temperature.

I_{is} is the ion saturation current and is equal to

$$I_{is} = A_i e n \sqrt{\frac{k_B(T_e + T_i)}{m_i}}, \tag{A.2}$$

where A_i is the effective probe surface area for ion collection.

I_{es} is the electron saturation current and is equal to

$$I_{es} = A_e \frac{1}{4} e n \sqrt{\frac{8 k_B T_e}{\pi m_e}} \tag{A.3}$$

where A_e is the effective probe surface area for electron collection.

When V_p equals the floating potential, V_f, no current is collected ($I_p = 0$). The expression for the relation between the floating and plasma potentials is

$$\Delta = \frac{e(\Phi - V_f)}{k_B T_e} = \ln\left(\frac{I_{es}}{I_{is}}\right) \tag{A.4}$$

where the difference between the plasma and floating potentials is normalized by the electron temperature in electron volts, and varies with the ratio of electron temperature to ion temperature and the atomic weight of the propellant species. In the case of lithium propellant for $T_e = 2$ eV and $T_i = 1$ eV (anode region temperatures after Ref. [25]) and $A_i = A_e$ the normalized difference is $\Delta = 3.66\frac{k_B T_e}{e}$.

When heating up the probe its surface will start emitting electrons thus reducing the current created by incoming electrons from the plasma. The emitted electron current density follows the relation

$$I_{em} = A_{em} A_R T_p^2 \exp\left(-\frac{e\phi_p}{k_B T_p}\right) \tag{A.5}$$

where A_{em} is the effective emitting probe surface area , A_R is the Richardson constant $A_R = 7.4 \times 10^5$ A m^{-2}K^{-2}, T_p is the probe surface temperature and ϕ_p is the probe material work function in electron volts. One can notice that as the probe becomes hotter the emitted electron current becomes greater.

The expression for the normalized difference between the floating and plasma potential in an emissive probe is

$$\Delta_{em} = \frac{e(\Phi - V_{f,em})}{k_B T_e} = \ln\left(\frac{I_{es}}{I_{is} + I_{em}}\right) \tag{A.6}$$

This implies that as the emitted electron current increases with probe surface temperature the floating potential approaches the plasma potential. In the case of a

Tungsten probe ($\phi_p = 4.55\ eV$), lithium propellant and $A_i = A_e = A_{em}$ Δ_{em} approaches zero at a probe surface temperature of $T_p = 2800\ K$.

Schrittwieser et al[74] showed that surface emission in emissive probes is in fact charge limited and saturates before the floating potential reaches the plasma potential. Using Child-Langmuir law he showed that the normalized difference between the floating and plasma potentials at probe saturation is found by solving the following equation

$$\frac{I_{is}}{I_{es}} + K\Delta_{CL}^{3/2} - \exp(-\Delta_{CL}) = 0 \tag{A.7}$$

with

$$K = \frac{A_{em}}{A_e}\frac{8\sqrt{\pi}}{9(d/\lambda_{De})^2} \tag{A.8}$$

where d is the sheath thickness.

In the above case of a Tungsten probe, lithium propellant and $A_i = A_e = A_{em}$ the solution is $\Delta_{CL} = 0.52\frac{k_B T_e}{e}$. This corresponds to a tungsten surface temperature of 2700 K. However, if the surface of the probe is coated with lithium the effective work function of tungsten drops to about 2.5 eV[13] and the surface temperature required to reach probe surface saturation is 1640 K. It is also important to note that the electron temperature has little effect over Δ_{CL} and the corresponding T_p. For example, if the electron temperature around the lithium-coated tungsten probe were 1 eV instead of 2 eV the normalized potential difference would drop to $\Delta_{CL} = 0.51\frac{k_B T_e}{e}$ and the corresponding probe surface temperature would be $T_p = 1590$ K. This implies that plasma potential calculations from probe voltage measurements are relatively insensitive to any error in the estimation of the electron temperature in the near anode region.

A.2 Magnetic Field Correction

In order to properly derive the plasma potential from the emissive probe voltage measurements one needs to account for the effects of the applied magnetic field on the probe. In the near-anode region the magnitude of the magnetic field is on the order of 0.01 T. Assuming T_e=3 eV and T_i=1 eV the corresponding electron and ion gyro-radii are of the order on 10^{-4} m and 10^{-2} m respectively. The electrons are therefore magnetized relative to the emissive langmuir probe whereas the ions are not. The effective surface area for electron current collection (A_e) is different than the surface area for ion current collection (A_i). The latter is simply the surface area of a cylinder with a diameter of 1 mm and length of 2 mm, that is $2\pi rL = 6.283$ mm^2. Since the probe is positioned parallel with respect to the anode surface, and thus parallel to the magnetic field flux lines (Fig. A.1), the effective electron collection surface area is the area projected to the magnetic flux lines.

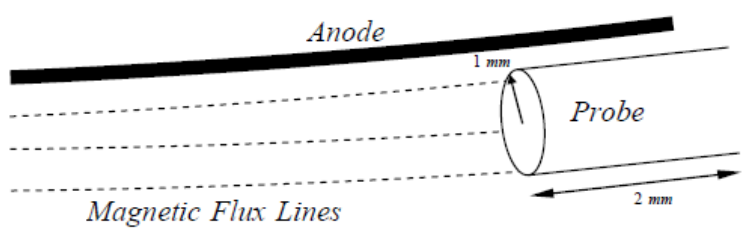

Figure A.1: Langmuir emissive probe positioning relative to the anode and magnetic flux lines.

The projected electron collection area is the area of the probe's cap that is $\pi r^2 = 0.125$ mm^2. The effective electron emitting surface area is also cylindrical. For this reason in our analysis $A_i/A_e = A_{em}/A_e = 1/8$. With the collection surface area correction the following can be calculated:

- Normalized potential difference without emission: $\Delta = 1.58\frac{k_B T_e}{e}$.
- Normalized potential difference for saturated emission: $\Delta_{CL} = 1.23\frac{k_B T_e}{e}$.

- Probe surface temperature for saturated emission: $T_p = 1580$ K.

One can notice that when accounting for the magnetic field effects the difference between the floating and plasma potentials is 1.58 T_e in the cold probe case and 1.23 T_e in the emissive probe case.

A.3 Probe Design

The design of an emissive probe posed a variety of challenges and constraints. The environment in the plasma plume is hostile to most materials due to the high heat flux from the plasma, radiation from the electrodes and gaseous and liquid lithium surface deposition. Due to the extremely high temperatures expected and material availability tungsten was chosen for the probe material (Fig. A.2). The probe insu-

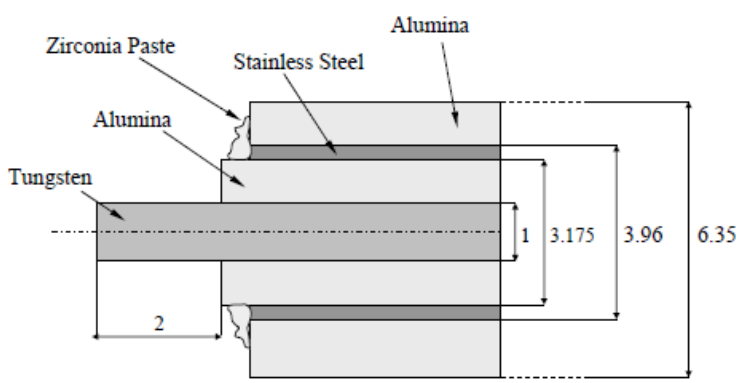

Figure A.2: Langmuir emissive probe schematic. All dimensions are in millimeters.

lating sheath material was chosen to be aluminum oxide (Al_2O_3) due to its resistance to both high temperatures and lithium corrosion. The probe sheath material was chosen to be stainless steel since it did not come in direct contact with the lithium propellant. The sheath is grounded and shields the probe from electrostatic noise. The probe was located 1 mm from the anode surface which is a distance a few orders of magnitude larger than the sheath length which is on the order of a few Debye lengths ($\lambda_{De} \simeq 10^{-6}$ m). This ensures a full capture of the anode sheath voltage fall

without measurement of the voltage drop between the electrodes.

The probe is not actively heated and reaches temperatures sufficiently high for saturated emission from heat flux from plasma enthalpy and radiated by the electrodes.

A.4 Circuit Design

The design of an electrical circuit to measure the probe's floating potential is subject to several constraints:

1. The floating potential is measured relative to the anode hence galvanic insulation is required to electrically protect the human operator.

2. The circuit impedance has to be greater than the probe-to-plasma interface impedance $R_{sheath} = \frac{k_B T_e}{e}/I_{is}$[75] so it does not interfere with current collection at the probe. In MPD thrusters I_{is} is typically on the order of milliamperes depending on the number density, n_e, thus the probe-to-plasma interface impedance is on the order of kilo-Ohms. The circuit impedance has to be a few orders of magnitude larger than that so as to prevent current leakage.

3. The probe measurements are taken within an electrical arc which might be changing at a high frequency. High frequency filtering is required to properly measure the sought-after steady state floating potential.

The final circuit design (Fig. A.3) consists of an isolation amplifier for galvanic insulation, a voltage divider to accommodate the input limits of the isolation amplifier, circuit input impedance of 100 MΩ and a low pass filter with a pole at 10 Hz. In addition, a potentiometer enables zeroing the measured signal by controlling current injection to the isolation amplifier. This procedure is done prior to thruster ignition. The circuit enables the measurement of voltages up to 108 V whereas the expected voltages are no more than 40 V.

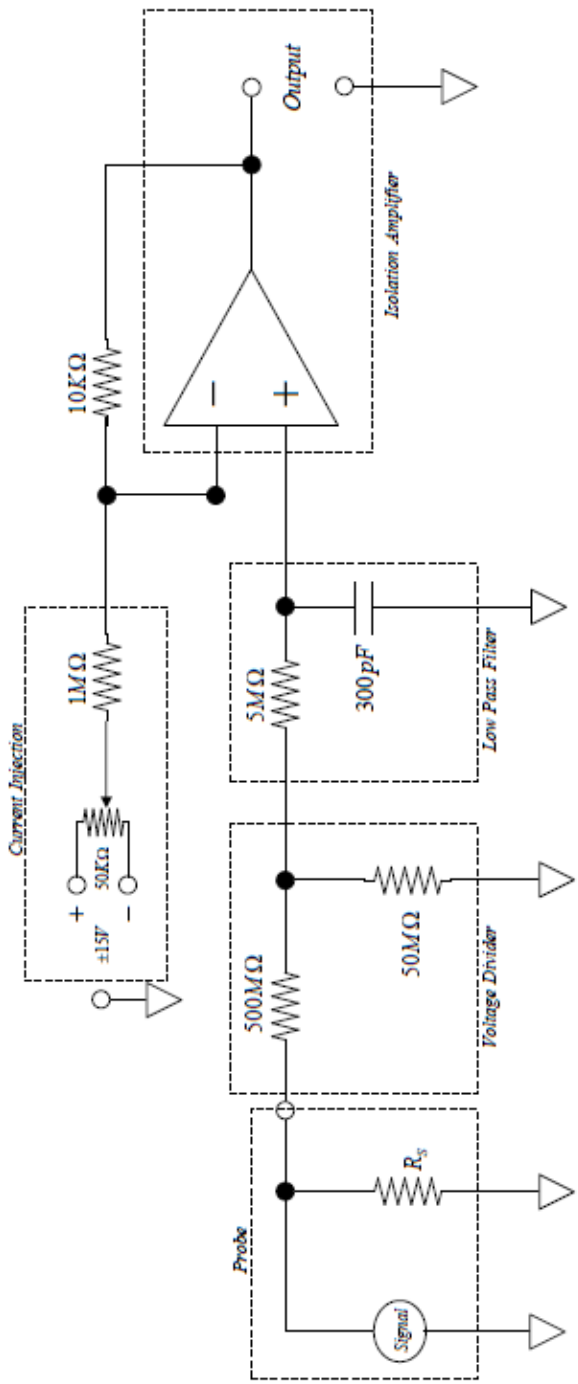

Figure A.3: Langmuir emissive probe circuit schematic.

Appendix B

Emissive Probe Temperature Estimation

The estimated probe temperature during thruster operation gives general design guidelines and an estimated surface emitted charge density according to the processes discussed in appendix A. A time dependent thermal numerical analysis was performed in order to estimate the probe temperature during thruster operation along with the time it takes the probe to reach that temperature.

The general equation describing the heating process is

$$C_m m \frac{dT}{dt} = P \tag{B.1}$$

where C_m is the probe heat capacity, m is the probe mass, dT is the temperature differential, dt is the time differential and P is the net input power to the probe. P is taken to be

$$P = P_{anode} + P_{cathode} + P_{plasma} - P_{probe} - P_{conduction} \tag{B.2}$$

where P_{anode} is the incoming power from anode radiation, $P_{cathode}$ is the incoming

power from cathode radiation, P_{plasma} is the power from plasma impinging on the probe, P_{probe} is the power radiated out from the probe and $P_{conduction}$ is the power conducted out from the probe to its base.

The estimation of the five power components should be done under a set of assumptions for the worst case scenario in which the probe is coldest. This will give the lowest temperature bound that should be greater than the required minimal temperature for surface emission charge saturation (1600 K found in appendix A). In order to estimate the five power components and solve Eq. B.1 we make the following assumptions:

1. The anode temperature is T_a=1300 K which is the lowest expected anode temperature from pyrometer measurements. The cathode temperature is T_c=3000 K[28].

2. The plasma number density is $n_e = 10^{18}\ m^{-3}$ which is the lowest expected number density in this type of thrusters[17, 37].

3. The ion and electron temperatures are $T_i = 2\ eV$ and $T_e = 2\ eV$ which are the expected temperatures in the near anode region.

4. The ion velocity in the plume is about $v_i = 3 \times 10^4$ m/s [28].

5. The power radiated from the probe does not affect the anode or cathode temperatures due to its small surface area.

6. The plasma impinging on the probe reaches a complete stop thus delivering all of its kinetic energy to the probe in form of heat.

7. The probe base temperature (10 inches from the probe tip) is at $T_b = 500$ K.

8. For convenience of future calculations we assume that the probe is located at anode face at the center of the thruster as seen in Fig. B.1. Under this assumption we expect the calculated temperature to be lower than in the case

in which the probe is right next to the anode wall since anode radiation to the probe is lower at the center of the thruster.

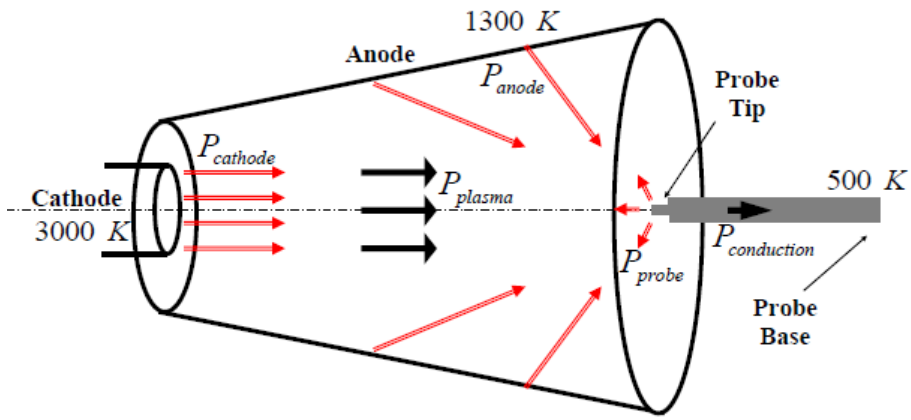

Figure B.1: General layout for the thermal analysis of the emissive probe.

B.1 Anode Radiation Power

The expression for the power radiated from the anode to the probe is

$$P_{anode} = \sigma \epsilon_W T_a^4 A_a F_{a \to p} \tag{B.3}$$

where ϵ_W is the emissivity of tungsten at 1300 K and is $\epsilon_W = 0.42$[49], A_a is the surface area of the anode and $F_{a \to p}$ is the radiation view factor from the anode to the probe which is a function of geometry alone. $F_{a \to p}$ is usually taken from view factor tables yet we could not find anywhere in literature a similar geometrical situation such as depicted in Fig. B.1. Therefore we calculate $F_{a \to p}$ by the basic definition of view factor

$$F_{x \to y} = \frac{1}{A_x} \int_{A_x} \int_{A_y} \frac{\cos\theta_x \cos\theta_y}{\pi R^2} dA_x dA_y \tag{B.4}$$

where A_x and A_y are the surface areas of the emitting and receiving bodies respectively, θ is the angle between the line of sight and the normal to the surface and R is

the distance between two points on the bodies. To simplify this calculation we make the assumptions:

1. The probe is a point recipient so that $\theta_y = 0°$ and $\cos\theta_y = 1$.

2. Due to the small size of the probe both θ_x and R are not a function of the position on the probe so that $\int_{A_y} \frac{\cos\theta_x}{\pi R^2} dA_y \simeq \frac{\cos\theta_x}{\pi R^2} A_y$

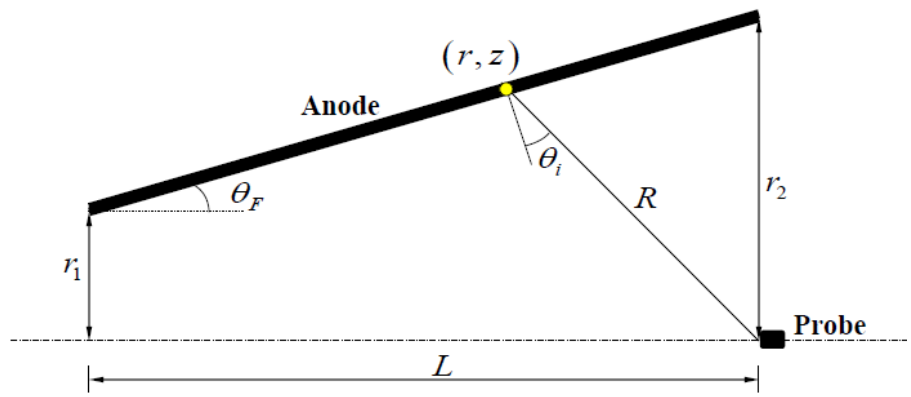

Figure B.2: General layout for view factor calculation between the anode and the probe.

Since the anode is an open frustum (Fig. B.2) all geometrical parameters can be written as a function of z and the calculation becomes

$$F_{a\to p} = \frac{A_p}{A_a} 2\pi \int_0^L \frac{\cos\theta_i(z)}{\pi R(z)^2} r(z) \sqrt{1 + \left(\frac{r_2 - r_1}{L}\right)^2} dz \tag{B.5}$$

where $r(z) = r_1 + \frac{(r_2 - r_1)}{L} z$, $R(z) = \sqrt{(L-z)^2 + r(z)^2}$ and $\theta_i(z) = arctg(\frac{L-z}{r(z)}) - \theta_F$.

We found the radiation view factor to be $F_{a\to p} = 0.0019$ and the radiation from the anode to the probe to be $P_{anode} = 1.92$ W.

B.2 Cathode Radiation Power

The expression for the power radiated from the anode to the probe is

$$P_{cathode} = \sigma \epsilon_W T_c^4 A_c F_{c \to p} \tag{B.6}$$

The radiation view factor ($F_{c \to p}$) was taken from Ref. [76] as the radiation view factors between two disks.

$$F_{c \to p} = 1/2 \left(S - \sqrt{S^2 - 4 \frac{r_p}{r_c}^2} \right) \tag{B.7}$$

where $S = 1 + \frac{1+(r_p/d)^2}{(r_c/d)^2}$, r_p and r_c are the probe and cathode radii respectively and d is the distance between the the probe and the cathode which are facing each other.

We found the radiation view factor to be $F_{c \to p} = 3.93 \times 10^{-5}$ and the radiation from the anode to the probe to be $P_{cathode} = 0.0384$ W.

B.3 Plasma Enthalpy Power

The expression for the power impinged by the plasma on the probe is

$$P_{plasma} = A_p n_e v_i \left(k_B T_e + k_B T_i + \frac{1}{2} m_i v_i^2 \right) \tag{B.8}$$

We found the plasma enthalpy power to be $P_{plasma} = 0.141$ W.

B.4 Probe Radiation Power

The expression for the power radiated by the probe itself is

$$P_{probe} = \sigma \epsilon_W A_p T_p^4 \tag{B.9}$$

The power radiated out by the probe is a function of the probe's temperature

which is the unknown variable in this analysis.

B.5 Conduction Power to Probe Base

The expression for the power conducted out through the probe is

$$P_{probe} = A_p \kappa_W \frac{(T_p - T_b)}{L_p} \tag{B.10}$$

where κ_W is the heat conduction coefficient of tungsten, T_b is the estimated probe base temperature and L_p is the probe length from the tip to its base. The power conducted out is a function of the probe's temperature which is the unknown variable in this analysis.

B.6 Results and Discussion

From the above power balance analysis we conclude that the majority of probe heating originates from anode radiation. This was expected due to the proximity of the probe to the anode, the long distance between the cathode and probe as well as the low plasma temperature.

Eq. B.1 was solved numerically and result shown in Fig. B.3. It can be seen from the results that the probe is heating up over time until it reaches steady state temperature after about 8 sec. The steady state temperature is about 1700 K which is greater than the required minimum of 1600 K for surface charge density saturation. Since this analysis was conducted for the worst case scenario we can conclude that in reality the probe temperature is higher than the one found in this analysis. Therefore the probe can be assumed to be at surface charge density saturation. The settling time indicates that at any thruster operation over 10 sec the probe can be considered in steady state and results valid for probe measurements.

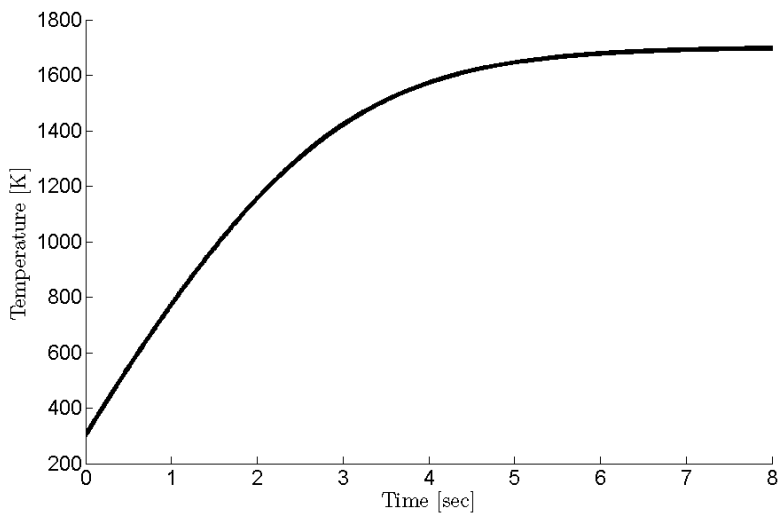

Figure B.3: Probe tip temperature (in K) Vs. Time (in sec).

Appendix C

Optical Pyrometer Gray Body Correction

Since no actual body in nature is a perfect blackbody any object can be assumed to be a gray body. A gray body emits radiation at a constant ratio of a blackbody radiation at all wavelengths. This ratio is named emissivity and is always less than 1. When measuring the temperature of an object by comparing its emitted intensity relative to the filament's intensity we are actually measuring the object's brightness temperature. The brightness temperature is the temperature under the assumption that the object is a blackbody. In order to find the real temperature of the object we need to correct for this assumption by relating the two temperatures. The expression for the emitted intensity of a blackbody is given by Planck's radiation law

$$I(T,\lambda) = \frac{2\pi hc^2}{\lambda^5}\frac{1}{\exp\left(\frac{hc}{\lambda k_B T_b}\right) - 1} \tag{C.1}$$

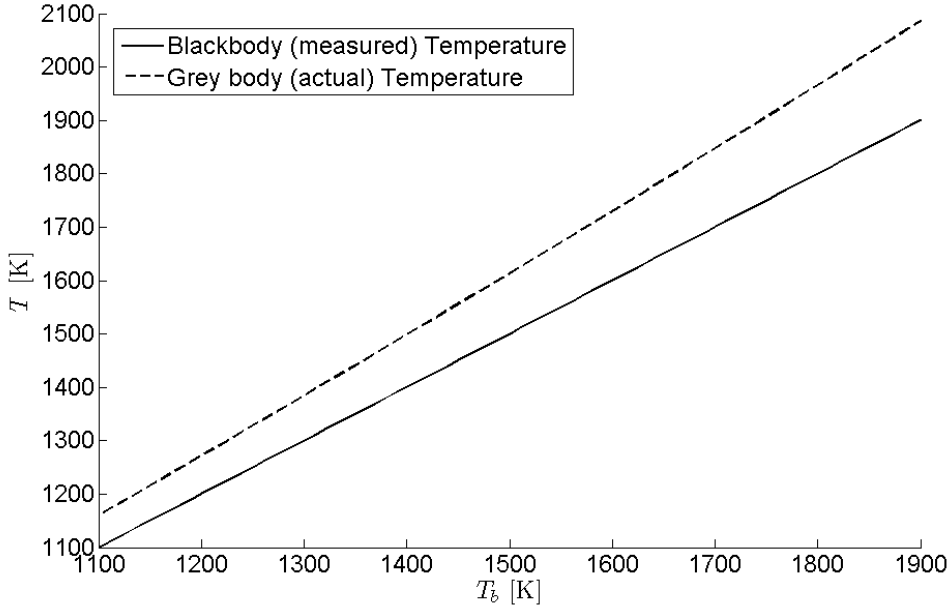

Figure C.1: Brightness temperature and gray body temperature for optical pyrometer measurements of anode temperature (ϵ_{eff}=0.354).

where T_b is the observed brightness temperature and λ is the wavelength (650 nm). The expression for the emitted intensity of a gray body with an emissivity ϵ is

$$I(T,\lambda) = \epsilon \frac{2\pi hc^2}{\lambda^5} \frac{1}{\exp\left(\frac{hc}{\lambda k_B T_g}\right) - 1}. \tag{C.2}$$

Equating the two expressions and solving for T_g gives[77]

$$T_g = \alpha \left[\ln\left[1 + \epsilon\left(e^{\alpha} - 1\right)\right]\right]. \tag{C.3}$$

where $\alpha = hc/\lambda k_B$. T_g can be regarded as the temperature at which a gray body with an emissivity ϵ has intensity equivalent to a blackbody with a temperature T_b. The measured brightness temperature and the equivalent gray body temperature for an effective emissivity of ϵ_{eff}=0.354 are plotted in Fig. C.1.

It can be seen from the figure that the actual anode temperature is up to 10% higher than the measured brightness temperature at the temperature range of 1100-1900 K,

i.e. without correcting for the gray body emissivity. This correction was made to all measurements conducted by the optical pyrometer.

Appendix D

Spectroscopic Measurements of Electron Temperature

D.1 Theoretical Background

Using spectroscopic measurements and the technique of relative line intensities one can calculate the electron temperature (T_e) of a given plasma [78].
In order to do so a few assumptions must be taken:

1. The plasma has to be assumed at LTE (Local Thermodynamic Equilibrium).
2. The plasma has to be assumed optically thin.

The reasons for making the above two assumptions are:

1. If LTE is assumed the bound electron distribution through the different energy levels can be assumed to have a Boltzmann distribution (Maxwellian).

$$\frac{n_m}{n} = \frac{g_m}{Z(T_e)} \exp\left(-\frac{E_m}{kT_e}\right) \tag{D.1}$$

where n_m is the population density of the mth energy level, n is the overall population density, g_m is the degeneracy of the mth energy level, $Z(T_e)$ is the partition function, E_m is the energy of the mth (upper) energy level and T_e is the electron temperature.

2. If the plasma is assumed to be optically thin, the spontaneous emission can be assumed to dominate stimulated absorption. For this case the expression for the intensity of one spectral line is:

$$I_{mn} = l_{op} \frac{hc}{4\pi} \frac{1}{\lambda_{mn}} A_{mn} n_m \tag{D.2}$$

where the mth energy level is the upper one and the nth is the lower. I_{mn} is the line intensity, l_{op} is the optical path length, h is Planck's constant, c is the speed of light, λ_{mn} the wavelength of the emitted line, A_{mn} is the spontaneous emission probability (Einstein coefficient) and n_m is the population density of the mth energy level.

From the above two mathematical relations we can derive the following expression for the intensity of one spectral line

$$I_{mn} = l_{op} C \frac{f_{nm}}{\lambda_{mn}^3} \frac{g_m}{Z(T_e)} n \exp\left(-\frac{E_m}{kT_e}\right) \tag{D.3}$$

where the mth energy level is the upper one and the nth is the lower. C is a proportion factor and f_{nm} is the oscillator strength.

Manipulating the above expression gives the relation

$$\ln\left[\frac{\lambda_{mn}^3 I_{mn}}{f_{nm} g_n}\right] = -\frac{1}{kT_e} E_m - \ln\left[\frac{Z(T_e)}{l_{op} C n}\right] \tag{D.4}$$

The above expression can be rewritten in the form $y = mx + y_0$ when defining $y = \ln\left[\frac{\lambda_{mn}^3 I_{mn}}{f_{nm} g_n}\right]$, $x = E_m$, $y_0 = -\ln\left[\frac{Z(T_e)}{l_{op} Cn}\right]$ and $m = -\frac{1}{kT_e}$.

Plotting a hypothetical graph of y vs. x for different emission lines should generate a straight line with $-\frac{1}{kT_e}$ as its slope.

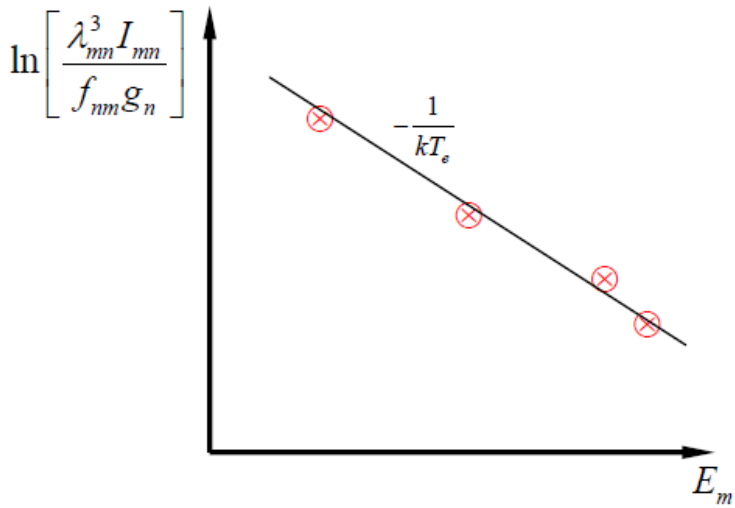

Figure D.1: Qualitative example of the spectroscopic technique of finding the electron temperature

It can be seen from the above figure that as higher energy levels have higher intensity the slope becomes less negative and the electron temperature is higher. This makes sense since higher electron temperature implies more energetic electron transitions.

It should also be noted that the only variable in the analysis is the intensity emission lines relative to other emission lines.

D.2 Spectrometer Calibration

The spectrometer used for the spectral measurements is an SP1 Thor Labs spectrometer with wavelength range of $257 - 816$ nm.

All spectrometers have a certain transmittance function. Different wavelengths exhibit different intensities for the same expected intensity. To calibrate the SP1 spectrometer there is a need for a black body source with a known intensity distribution. The source used for this calibration is a calibration lamp of the type LS-1 Tungsten Halogen Light Source made by Ocean optics. The calibration lamp emulates a black body radiation curve with a temperature of 3100 K .

The spectrometer pointed towards the calibration source produced the results presented in Fig. D.2. To find an expression for the oscillating line form we need to fit a curve to it. The curve was fit to the bottom part of the oscillating wave curve since the peaks correspond to tungsten lattice emission of the calibration lamp and represent deviations from the expected black body curve.

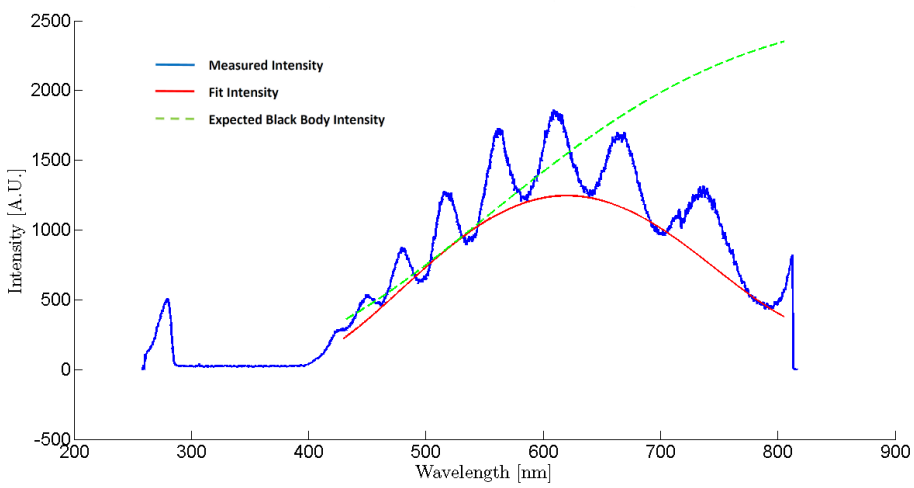

Figure D.2: Measured spectrometer intensity vs. wavelength for the calibration lamp (3100 K)

In addition, in Fig. D.2 the cyan line representing the black body radiation seems to have a different shape than the measured shape of the spectrometer. Since the black body curve must be higher in intensity than the measured curve for all wavelengths then the intensity must be changed.

The intensity of the black body curve will be changed so it will be higher or equal to the measured curve. That point where it is equal will be the point where the spectrometer transmittance is 1 ($\tau = 1$). All other points will have a lower transmittance. At this point and in order to obtain the transmittance function of the spectrometer the only thing left to do is to divide the measured intensity at each and every point by the expected black body curve. The result is presented in Fig. D.3.

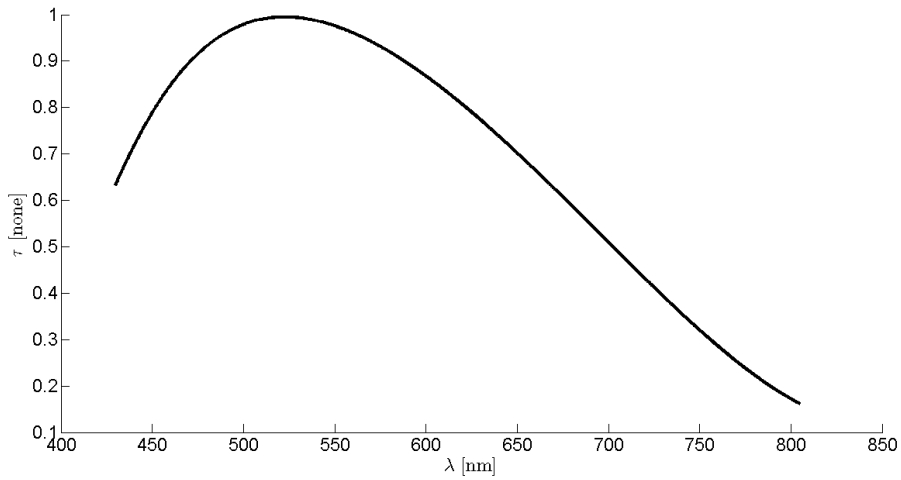

Figure D.3: Calculated transmittance function for the Thor Labs spectrometer

The transmittance function has a peak at around $\lambda = 520\ nm$ and drops sharply down to a few percent at around $\lambda = 800\ nm$. The cyan line represents the line fit to the calculated transmittance function.

Due to the poor transmittance at high wavelengths the spectrometer is highly unreliable for high wavelengths and fairly reliable at wavelengths of $\lambda = 450 - 650\ nm$.

D.3 Additional Corrections

An additional correction should be made for any measured signal by the Thor Labs spectrometer. This correction originates from the transmittance of the glass through

which the light passes.

The type of glass installed on the port covers is Pyrex Borosilicate glass. This type of common glass is known for its bad transmittance capability in the short wavelength range of below 400 nm and trasmittance of about 90% at a wavelength greater than 400 nm and into IR[79] as presented in Fig. D.4.

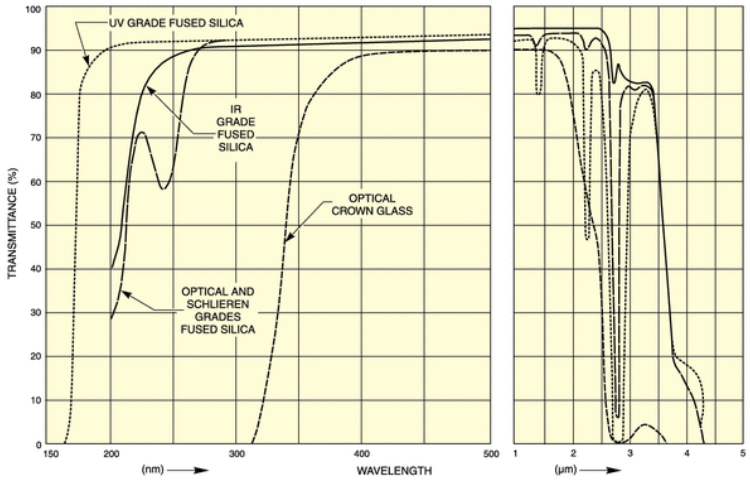

Figure D.4: Transmittance curve of Borosilicate Pyrex glass with thickness of 1 cm at different wavelengths

Since the thickness of the port cover glass is 3/4″ (1.9 cm) we can estimate the transmittance of the glass port cover to be about 80% at wavelengths greater than 400 nm and negligible at lower wavelengths. It is important to note that since we are examining the relative magnitude of emission lines at different wavelengths the intensity ratio between two wavelengths will not change by the port cover's glass as long as the transmittance is the same at the same two wavelengths.

It is important to note that since the calibration source had a much lower intensity than the plasma during thruster operation the spectrometer calibration was not performed through the glass window due to the large required distance between the source and spectrometer collimator.

Bibliography

[1] R. L. Burton, K. Brown, and A. Jacobi. Low cost launch of payloads to low earth orbit. *Journal of Spacecraft and Rockets*, 43(3):221–224, 1990.

[2] Dolores Beasley, Guy Webster, George Diller, and Joan Underwood. Mars reconnaissance orbiter launch - press kit. Technical report, NASA, 2005.

[3] Martin J. L. Turner. *Rocket and Spacecraft Propulsion*. Springer, New York, 2009.

[4] Archie E. Roy. *The Foundations of Astrodynamics*. The Macmillan, New York, 1965.

[5] Robert G. Jahn and Edgar Y. Choueiri. *Electric Propulsion Value in the Encyclopedia of Physical Science and Technology, Third Edition, Volume 5*. Academic Press, San Diego, 2002.

[6] A.D. Kodys and E.Y. Choueiri. A critical review of the state-of-the-art in the performance of applied-field magnetoplasmadynamic thrusters. In *The 41st Joint Propulsion Conference (JPC), July 10-14, 2005, Tucson, AZ. AIAA-2005-4247*, 2005.

[7] Michael R. LaPointe, Eugine Strzempkowski, and Eric Pencil. High power MPD thruster performance measurements. In *The 40st Joint Propulsion Conference (JPC), July 11-14, 2004, Fort Lauderdale, FL. AIAA-2004-3467*, 2004.

[8] V.B. Tikhonov, S.A. Semenikhin, J.R. Brophy, and J.E. Polk. Performance of 130kw MPD thruster with an external magnetic field and LI as a propellant. In *The 25th International Electric Propulsion Conference (IEPC), Oct, 1997, Cleveland, Ohio, IEPC-97-117*, 1997.

[9] H. Maecker. Plasma jets in arcs in a process of self-induced magnetic compression. *Z. Phys.*, 141:198–216, 1955.

[10] R.G. Jahn. *Physics of Electric Propulsion.* McGraw-Hill, New York, 1968.

[11] E. Y. Choueiri. The scaling of thrust in self-field magnetoplasmadynamic thrusters. *Journal of Propulsion and Power*, 14(5):744–753, 1998.

[12] F. Paganucci, P. Rossetti, M. Andrenucci, V. B. Tikhonov, and V. A. Obukhov. Performance of an applied field MPD thruster. In *The 27th International Electric Propulsion Conference (IEPC), October 15-19, 2001, Pasadena, California, USA, AIAA-01-132*, 2001.

[13] J.E.Polk and T.J. Pivirotto. Alkali metal propellants for MPD thrusters. In *AIAA/NASA/OAI Conference on Advanced SEI Technologies, September 4-6, 1991, Cleaveland, OH. AIAA-91-3572*, 1991.

[14] V.P. Ageyev and V.G. Ostrovsky. High current stationary plasma accelerator of high power. In *The 23th International Electric Propulsion Conference (IEPC), 1993, Seattle, WA, IEPC-93-117*, 1993.

[15] E. Choueiri. Plasma propulsion. Class notes, MAE524 Lecture, MAE Department, Princeton University, 2008.

[16] Daniel D. Villani. *Energy Loss Mechanisms in a Magnetoplasmadynamic Arcjet.* PhD thesis, Princeton Univ., 1982.

[17] Fradkin D.B. *Analysis of Acceleration Mechanisms and Performance of an Applied Field MPD Arcjet*. PhD thesis, Princeton Univ., 1973.

[18] H. Tobari, A. Ando, M. Inutake, and Kunihiko Hattori. Characteristics of electromagnetically accelerated plasma flow in an externally applied magnetic field. *Phys. Plasmas*, 14, 2007.

[19] Edgar Y. Choueiri and Hideo Okuda. Anomalous ionization in the MPD thruster. In *23th International Electric Propulsion Conference (IEPC), 1993, Seattle, WA, IEPC-97-067*, 1993.

[20] R. L. Burton, K. E. Clark, and R. G. Jahn. Measured performance of a multi-megawatt MPD thruster. *Journal of Spacecraft*, 20(3):299–304, 1983.

[21] Kevin D. Diamant. *The Anode Fall in a High Power Pulsed MPD Thruster*. PhD thesis, Princeton Univ., 1996.

[22] Alec Damian Gallimore. *Anode Power Deposition in Coaxial MPD Thrusters*. PhD thesis, Princeton Univ., 1992.

[23] Roger M. Myers and George C. Soulas. Anode power deposition in applied-field MPD thrusters. In *The 28th Joint Propulsion Conference (JPC), July 6-8, 1992, Nashville, TN. AIAA-92-3463*, 1992.

[24] Roger M. Myers, Alex D. Gallimore, and R.G.Jahn. Anode power deposition in an applied-field segmented anode MPD thruster. *Journal of propulsion and power*, 10(2):262–268, 1994.

[25] G. Popov, V. Kim, V.B. Tikhonov, and S. Semenikhin. The second quarterly report on the stage no 3 c,d of the contract on the research studies no nasw-4851 between RIAME MAI and NASA. Technical report, Moscow Aviation Institute (MAI), Moscow, Russia, April 1997.

[26] M. Andrenucci. *Magnetoplasmadynamic Thrusters*. Wiley, Online Library, 2010.

[27] G. Popov, V. Kim, V.B. Tikhonov, and S. Semenikhin. The third quarterly report on the stages no 5-6 of the contract on the research studies no nasw-4851 between RIAME MAI and NASA. Technical report, Moscow Aviation Institute (MAI), Moscow, Russia, June 1995.

[28] G. Popov, V. Kim, V.B. Tikhonov, and S. Semenikhin. The first quarterly report on the stage no 3 a of the contract on the research studies no nasw-4851 between RIAME MAI and NASA. Technical report, Moscow Aviation Institute (MAI), Moscow, Russia, April 1996.

[29] G. Popov, V. Kim, V.B. Tikhonov, and S. Semenikhin. The second quarterly report on the stage no 2 a of the contract on the research studies no nasw-4851 between RIAME MAI and NASA. Technical report, Moscow Aviation Institute (MAI), Moscow, Russia, July 1996.

[30] G. Popov, V. Kim, V.B. Tikhonov, and S. Semenikhin. The second quarterly report on the stage no 3 b of the contract on the research studies no nasw-4851 between RIAME MAI and NASA. Technical report, Moscow Aviation Institute (MAI), Moscow, Russia, December 1996.

[31] G.A. Popov, V. Kim, V.B. Tikhonov, S.A. Semenikhin, and M.K. Tibrina. The third quarterly report on the milestones (a)(3) and (a)(5)(c) of sow of contract no 960938 between RIAME MAI and JPL. Technical report, Moscow Aviation Institute (MAI), Moscow, Russia, June 1998.

[32] G.A. Popov, V. Kim, V.B. Tikhonov, S.A. Semenikhin, and M.K. Tibrina. The third quarterly report on the milestones (a)(4) and (a)(5)(d) of sow of contract no 960938 between RIAME MAI and JPL. Technical report, Moscow Aviation Institute (MAI), Moscow, Russia, December 1998.

[33] V.B. Tikhonov, S.A. Semenikhin, V. A. Alexandrov, G. A. Dynakonov, and G. A. Popov. Research of plasma acceleration processes in self-field and applied-field thrusters. In *The 23th International Electric Propulsion Conference (IEPC), Oct, 1993, Seattle, WA, IEPC-93-076*, 1993.

[34] G. Serianni, N. Vianello, F. Paganucci, P. Rossetti, V. Antoni, M. Bagatin, and M. Andrenucci. Plasma diagnostics in an applied field MPD thruster. In *The 27th International Electric Propulsion Conference (IEPC), October 15-19, 2001, Pasadena, California, USA, IEPC-01-135*, 2001.

[35] F. Paganucci, P. Rossetti, M. Andrenucci, V.B. Tikhonov, and V.A. Obukhov. Performance of an applied field MPD thruster with a pre-ionization chamber. In *The 28th International Electric Propulsion Conference (IEPC), March, 2003, Toulouse, France, IEPC-2003-0302*, 2003.

[36] Roger M. Myers. Scaling of 100kw class applied-field MPD thrusters. In *The 28th Joint Propulsion Conference (JPC), July 6-8, 1992, Nashville, TN. AIAA-92-3462*, 1992.

[37] Roger M. Myers. Plume characteristics of MPD thrusters: A preliminary examination. In *The 25th Joint Propulsion Conference (JPC), July 10-12, 1989, Monterey, CA . AIAA-89-2832*, 1989.

[38] R. M. Myers, M. Mantenieks, and J. Sovey. Geometric effects in applied-field MPD thrusters. In *The 21st International Electric Propulsion Conference (IEPC), July 18-20, 1990, Orlando, Florida, USA, AIAA-90-2669*, 1990.

[39] G. Krülle. Characteristics and local analysis of mpd thruster operation. In *AIAA Electric Propulsion Conference, September 11-13, 1967, Colorado Springs, CO, 67-672*, 1967.

[40] G. Krülle and E. Zeyfang. Preliminary conclusions of continuous applied field electromagnetic thruster research at dfvlr. In *The 11th AIAA Electric Propulsion Conference, March 19-21, 1975, New Orleans, LA, 75-417*, 1975.

[41] Gerd Krülle, Monika Auweter Kurtz, and Akihiro Sasoh. Technology and application aspects of applied field magnetoplasmadynamic propulsion. *Journal of Propulsion and Power*, 14(5):754–763, 1998.

[42] Hiroyuki Tobari, Masaaki Inutake, Akira Ando, and Kunihiko Hattori. Spatial distribution of lorentz forces in an applied-field magneto-plasma-dynamic arcjet plasma. *J. Plasma Fusion Res.*, 80(8):651–652, 2004.

[43] Ando Akira, Ashino Masashi, Sagi Yukiko, Inutake Masaaki, Hattori Kunihiko, Yoshinuma Mikirou, Imasaki Atsushi, Tobari Hiroyuki, and Yagai Tsuyoshi. Spectroscopic studies of a high mach-number rotating plasma flow. *J. Plamsa Fusion Res.*, 4:373–378, 2001.

[44] P.G. Mikellides and P.J. Turchi. A theoretical model for the thrust and voltage of applied-field MPD thrusters. In *The 34th Joint Propulsion Conference (JPC), July 13-15, 1998, Cleveland, OH. AIAA-94-3474*, The Ohio State University, Columbus, Ohio, USA, 1998.

[45] Aaron Jaan Saber. *Anode Power in the Quasi-Steady MPD Thruster*. PhD thesis, Princeton Univ., 1974.

[46] E.Y. Choueiri, A.J. Kelly, and R.G. Jahn. The manifestation of alfven's hypothesis of critical ionization velocity in the performance of mpd thrusters. In *The 18th International Electric Propulsion Conference (IEPC), September 30 - October 2, 1985, Alexandria, Virginia, AIAA-85-2037*, 1985.

[47] Cassady L.D. *Lithium-Fed Arc Multichannel and Single-Channel Hollow Cathode: Experiment and Theory*. PhD thesis, Princeton Univ., 2006.

[48] A.D. Kodys, G. Emsellem, L.D. Cassady, J.E. Polk, and E.Y. Choueiri. Lithium mass flow control for high power lorentz force accelerators. Technical report, Princeton Univ., Princeton, NJ, USA, Jet Propulsion Lab, Pasadena, CA, 2001.

[49] David R. Lide. *CRC Handbook of Chemistry and Physics, 77th Edition*. National Institute of Standards and Technology, 1997.

[50] T. Yoshikawa, K. Onoe, and M. Yasui. A low-power arcjet thruster for space propulsion. In *The 18th International Electric Propulsion Conference (IEPC), September 30- October 2, 1985, Alexandria, Virginia, IEPC-85-2032*, 1985.

[51] G. L. Cann, R. L. Harder, and S. T. Nelson. Experimental performance of the alphathrustor. In *AIAA Electric Propulsion and Plasmadynamics Conference, September 11-13, 1967, Colorado Springs, Colorado, AIAA-67-687*, 1967.

[52] N. J. Wood, J. J. Osborne, G. T. Roberts, and S. B. Gabriel. Characterization of a low-power steady-state magnetoplasmadynamic thruster for non-propulsive applications. *Plasma Sources Sci. Technol*, 6:484–491, 1997.

[53] Luke Uribarri. *Onset Voltage Hash and Anode Spots in Quasi-Steady Magnetoplasmadynamic Thrusters*. PhD thesis, Princeton Univ., 2008.

[54] T. M. Randolph, W. F. Von Jaskowsky, A. J. Kelly, and R. G. Jahn. Ionization processes in the interelectrode region of an MPD thruster. In *The 22nd International Electric Propulsion Conference (IEPC), October 14-17, 1991, Viareggio, Italy, AIAA-91-052*, 1991.

[55] Edgar Y. Choueiri and Thomas M. Randolph. Ionization front in a high-current gas discharge. *Physics of Plasmas*, 14, 2007.

[56] D. Lev and E.Y. Choueiri. Scaling of anode sheath voltage fall with the operational parameters in AF-MPD thrusters. In *The 32th International Electric*

Propulsion Conference (IEPC), September 11-15, 2011, Wiesbaden, Germany, IEPC-2011-222, 2011.

[57] A. J. Kelly, N. M. Nerheim, and J. A. Gardner. Electron density and temperature measurements in the exhaust of an MPD source. *AIAA Journal*, 4(2):291–295, 1966.

[58] Hirokazu Tahara, Yoichi Kagaya, and Takao Yoshikawa. Exhaust plume characteristics of quasi-steady MPD thrusters. In *The 27th International Electric Propulsion Conference (IEPC), October 15-19, 2001, Pasadena, California, USA, AIAA-01-133*, 2001.

[59] Ronald C. Oberth and Robert G. Jahn. Anode phenomenon in high-current accelerators. *AIAA Journal*, 10(1):86–91, 1972.

[60] Kenn E. Clark and Robert G. Jahn. Quasi-steady plasma acceleration. *AIAA Journal*, 8(2):216–220, 1970.

[61] V. V. Subramaniam and J. L. Lawless. Thermal instabilities of the anode in a magnetoplasmadynamic thruster. *J. Propulsion*, 6(2):221–224, 1990.

[62] F.F. Chen. *Introduction to Plasma Physics and Controlled Fusion*. Springer, New York, 1984.

[63] O.W. Richardson. *The Emission of Electricity form Hot Bodies*. Longman, Green and co., London, New York, 1921.

[64] M. Mitchner and Charles H. Kruger. *Partially Ionized Gases*. Wiley series, 1973.

[65] D. L. Tilley, S. Castillo, M. S. Jolly, E. Niewood, and M. Martinez-Sanchez. A comparison of theory and measurements in the anode region of a self-field cylindrical mpd thruster. In *The 30th Joint Propulsion Conference (JPC), June 27-29, 1994, Indianapolis, IN. AIAA-94-3249*, 1994.

[66] L. K. Rudolph. *The MPD Thruster Onset Current Performance Limitation.* PhD thesis, Princeton Univ., 1980.

[67] T.M. Golz, M. Auweter-Kurtz, H. Habiger, and H.L. Kurtz. High specific impulse performance of a 100 kw radiation cooled thermal arcjet thruster. In *The 30th Joint Propulsion Conference (JPC), June 27-29, 1994, Indianapolis, IN. AIAA-94-3249*, 1994.

[68] D. Lev and E.Y. Choueiri. Scaling of efficiency with applied magnetic field in magnetoplasmadynamic thrusters. Accepted for publication in the Journal of Propulsion and Power, 2011.

[69] D. Lev and E.Y. Choueiri. Scaling of efficiency with applied magnetic field in magnetoplasmadynamic thrusters. In *The 46th Joint Propulsion Conference (JPC), July 25-28, 2010, Nashville, TN. AIAA-2010-7024*, 2010.

[70] Maris A. Mantenieks, James S. Sovey, Roger M. Myers, Thomas W. Haag, Paul Raitano, and James E. Parkes. Performance of a 100 kw class applied field MPD thruster. In *The 25th Joint Propulsion Conference (JPC), July 10-12, 1992, Monterey, CA. AIAA-89-2710*, 1989.

[71] D.B.Fradkin and D.J.Roehling. Thrust stand performance of a lithium fueled applied field MPD arcjet. In *The 13th Symposium on the Engineering Aspects of Magnetohydrodynamics, March 26-28, 1973, Stanford University. Number VI.11.1*, 1973.

[72] H. Tahara, F. Takiguchi, Y. Kagaya, and T. Yoshikawa. Performance characteristics and discharge features of a quasi-steady applied-field MPD arcjet. In *The 21st International Electric Propulsion Conference (IEPC), July 18-20, 1990, Orlando, Florida, USA, AIAA-90-2669*, 1991.

[73] Iain D. Boyd, Kevin Scavezze, Chunpei Cai, James E. Polk, and Edgar Y. Choueiri. Analysis of plume backflow from a lithium magnetoplasmadynamic thruster. In *The 29th International Electric Propulsion Conference (IEPC), Oct, 2005, Princeton, NJ, IEPC-2005-014*, 2005.

[74] Roman Schrittwieser, Jiri Adamek, Petru Balan, Martin Hron, Cordina Ionita, Karel Jakubka, Ladislav Kryska, Emilio Martines, Jan Stockel, Milan Tichy, and Guido Van Oost. Measurements with an emissive probe in the castor tokamak. *Plasma Phys. Control. Fusion*, 44:567–578, 2002.

[75] L. Dorf, Y. Raites, and N. J. Fisch. Electrostatic probe apparatus for measurements in the near-anode region of hall thrusters. *Review of Scientific Instruments*, 75(5):1255–1260, 2004.

[76] Frank P. Incropera and David P. DeWitt. *Introduction to Heat Transfer, 3rd Edition*. John Wiley and Sons, 1996.

[77] Dan Maclsaac, Garry Kanner, and Graydon Anderson. *"Basic Physics of the Incandescent Lamp", The Physics Teacher, Vol. 37*. AAPT - Physics Education, December 1999.

[78] H.R. Griem. *Plasma Spectroscopy*. McGraw-Hill, New York, 1964.

[79] Newport Corporation. Tranmittance of optical materials, May 2011.